Handheld Force-Controlled Ultrasound Probe

by

Matthew Wright Gilbertson

B.S. Mechanical Engineering, Massachusetts Institute of Technology
(2008)

Submitted to the Department of Mechanical Engineering
in partial fulfillment of the requirements for the degree of

Master of Science in Mechanical Engineering

at the

MASSACHUSETTS INSTITUTE OF TECHNOLOGY

June 2010

Author ....
Department of Mechanical Engineering
May 7, 2010

Certified by ....
Brian W. Anthony
Research Scientist, Department of Mechanical Engineering
Thesis Supervisor

Accepted by ....
David E. Hardt
Graduate Officer, Department of Mechanical Engineering

Handheld Force-Controlled Ultrasound Probe

by

Matthew Wright Gilbertson

Submitted to the Department of Mechanical Engineering
on May 7, 2010, in partial fulfillment of the
requirements for the degree of
Master of Science in Mechanical Engineering

Abstract

An hand-held force controlled ultrasound probe has been developed. The controller maintains a prescribed contact force between the probe and a patient's body. The device will enhance the diagnostic capability of free-hand elastography, swept-force compound imaging, and make it easier for a technician to acquire repeatable (i.e. directly comparable) images over time. The mechanical system consists of an ultrasound probe, ballscrew-driven linear actuator, and a force/torque sensor. The feedback controller commands the motor to rotate the ballscrew to translate the ultrasound probe in order to maintain a desired contact force. In preliminary user studies it was found that the control system maintained a constant contact force with 1.7 times less variation than human subjects who watched a force gauge. Users without a visual force display maintained a constant force with 20 times worse variation. The system was also used to determine the viscoelastic properties of soft tissue. In three mock ultrasound examinations one hour apart in which the goal was two obtain two consistent images at the same force, an unassisted operator obtained the second image at a 20% lower force, while the operator assisted by the controller obtained the same force to within <2%. The device enables users to gather more force-consistent images over time.

Thesis Supervisor: Brian W. Anthony
Title: Research Scientist, Department of Mechanical Engineering

Acknowledgments

I would like thank my advisor Brian Anthony. Brian's diverse set of skills enabled him help me on a wide range of subjects from mechanical design to controls to general project strategizing. Brian always found a way to make time for me when I had questions or needed advice. I eagerly look forward to working with him in the future.

And I would like to thank Shih-Yu Sun, our computer science ninja. I believe Shih-Yu received a black belt in Matlab in Taiwan. Combining forces with Shih-Yu has enabled this project to soar.

I'd also like to thank Jared Trotter for his UROP help during the summer of 2009. His legacy lives on in the form of several high-quality parts he helped machine that we're still using today.

Contents

List of Figures

List of Tables

Chapter 1

Introduction

The diagnostic capabilities of freehand ultrasound imaging systems can be enhanced by measuring the contact force of the ultrasound probe with the body. Ultrasound is used to image soft tissues of the body. Because of its benign nature it is used extensively in medicine to image, for example, the abdomen, the thyroid, and muscles. To gather "freehand" images, an ultrasound technician grasps the probe in his/her hand and places the probe in contact with the patient's skin. Ultrasonic acoustic waves are emitted. By measuring the reflections of the waves the internal structure of the tissue can be determined. The harder the probe is pressed into the body the better the coupling between probe and tissue and the higher the signal-to-noise ratio (SNR) of the images. Typical ultrasound examinations of the carotid artery require contact forces of up to 6.4N [28], and examinations of the abdomen require up to 20N (determined qualitatively from a visit to Terason, Inc of Burlington, MA, an ultrasound technology company).

For soft areas of the body, especially those near the surface, the contact forces required to obtain a high-SNR image deform the tissue itself [29]. Fig. 1 shows three ultrasound images of the brachial artery taken at different forces using the device presented in this paper. The artery (at top) is circular in the 1N image but compressed and oval in the 5N image. The deep tissue, shown in the dotted box, is closer to the surface due to tissue compression.

Thus, the ultrasound system gathers images of deformed tissue. This presents

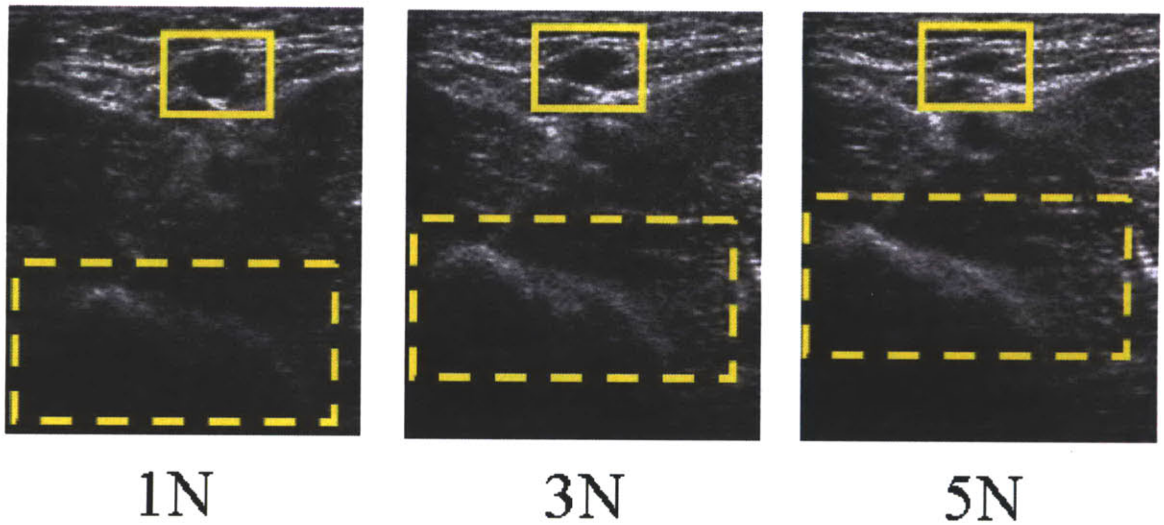

Figure 1-1: Ultrasound images of the brachial artery area taken at 1N, 3N, and 5N contact force using the device.

a diagnostic challenge because body feature dimensions should be based on images of the undeformed or consistently deformed tissue. For example, if two images are taken of the spleen, one month apart, and the two images are gathered with different contact forces it will be difficult for a technician to directly compare the images since they contain different levels of distortion. If instead the same force could be applied in acquiring each image, it would be easier for a technician to make an accurate diagnosis.

Measurement of ultrasound probe contact force is also important in the field of elastography, in which the tissue deformation over a change in force is measured in order to determine the mechanical properties of the tissue, such as the stiffness [17]. An electro-mechanical system that can both measure and control the contact force between the ultrasound probe and the body will thus be able to enhance the diagnostic capabilities of ultrasound imaging. This work focuses on the design of a hand-held single-degree of freedom force-controlled imaging system. We are also creating deformation correction algorithms that use finite element modeling to calculate the undistorted image of tissue based on the applied force [31].

1.1 Current Technology

There has been interest in the development of systems that can control ultrasound probe contact force or the relative position between the probe and the patient.

Numerous advances in teleoperated ultrasound imaging robots have been achieved: [28],[14],[33],[32],[13],[23],[26]. [28],[14], and [33] present teleoperated multi-degree of freedom (DOF) devices that consist of a long arm reaching over the patient with the ultrasound probe mounted at the endpoint. In these systems the patient is moved into the workspace of the robot. Salcudean et al [28] created a six-DOF teleoperated system that can be used to track the length of the carotid artery. The device is anchored to a table next to the patient and has a long arm with an ultrasound probe at the endpoint that reaches to the patient.

Degoulange et al [14] present a six-DOF robot arm that can similarly be used to position an ultrasound probe at a desired contact force with the patient. Vilchis-Gonzalez [33] developed a three-DOF dual remote-center robot that manipulates the probe to achieve two localized rotational and one linear DOF. The device is suspended over the patient by an external structure.

Numerous smaller imaging systems have been developed that are localized on the patient's body. This results in a smaller structural loop between the patient and the probe. Vilchis et al in [32] present a three-DOF device that is strapped to the patient by a series of belts, which are driven by motors secured to the examination bed. Courreges et al [13] present a three-DOF hand-held system that is held against the patient's body by an ultrasound technician. The system moves in three axes to perform an image sweep while the technician holds the device in place.

Several haptic devices enable the technician to control the movements of a remote ultrasound imaging robot. Marchal et al [23] designed a one-DOF haptic device that uses a linear actuator to feedback to the technician the force encountered by the slave robot. Najafi and Sepehri [26] created a four-DOF kinematically decoupled haptic probe and associated slave robot that is held above the patient similarly to [28],[14], and [33]. Burcher [12] presents a system that consists of a passive ultrasound probe equipped with force sensor and a stereoscopic positioning system. The force and position are recorded each time an ultrasound image is gathered.

There is currently no actuated ultrasound probe system that fits comfortably in a technician's hand that allows the technician to apply a constant, or otherwise programmable, force. We envision a compact system not much bigger than the ultrasound probe itself that the technician could use to gather more consistent and insightful images.

1.2 Thesis Scope

This thesis describes the design of an electro-mechanical system to improve the quality and diagnostic capabilities of ultrasound imaging. We first discuss the evolution of the focus of the project from initially controlling position, orientation, and force to simply controlling force. We discuss in detail the design of two prototypes to control position, orientation, and force. We next discuss the design of the third prototype to control force and create a model of the device. We compare its performance to the model predictions and describe the results of experiments using the system.

Chapter 2

Systems for Position Control

This chapter describes the design of two prototypes to control the position and orientation of the ultrasound probe with respect to the patient's body. The first Spherical Motion Frame uses two curved semicircular tracks with intersecting centers to vary the orientation of the ultrasound probe about the probe's tip. The Cylindrical Motion Frame uses two parallel degrees of freedom to change the yaw angle of the ultrasound probe in addition to its linear position.

2.1 Spherical Motion Frame (SMF)

The first prototype we developed is shown in Fig 2-1. It has two sliding bearings which provide for two rotational degrees of freedom of the white shaft in the center of the image, which represents an ultrasound probe.

2.1.1 Design of the Spherical Motion Frame

The focus of the project evolved during the course of this research. The initial goal was to create an ultrasound scanning device with multiple degrees of freedom. The device would be placed in contact with the patient (or the patient would be placed in the workspace of the device) and the device would manipulate the ultrasound probe through a range of positions and orientationas at a programmable force, acquiring

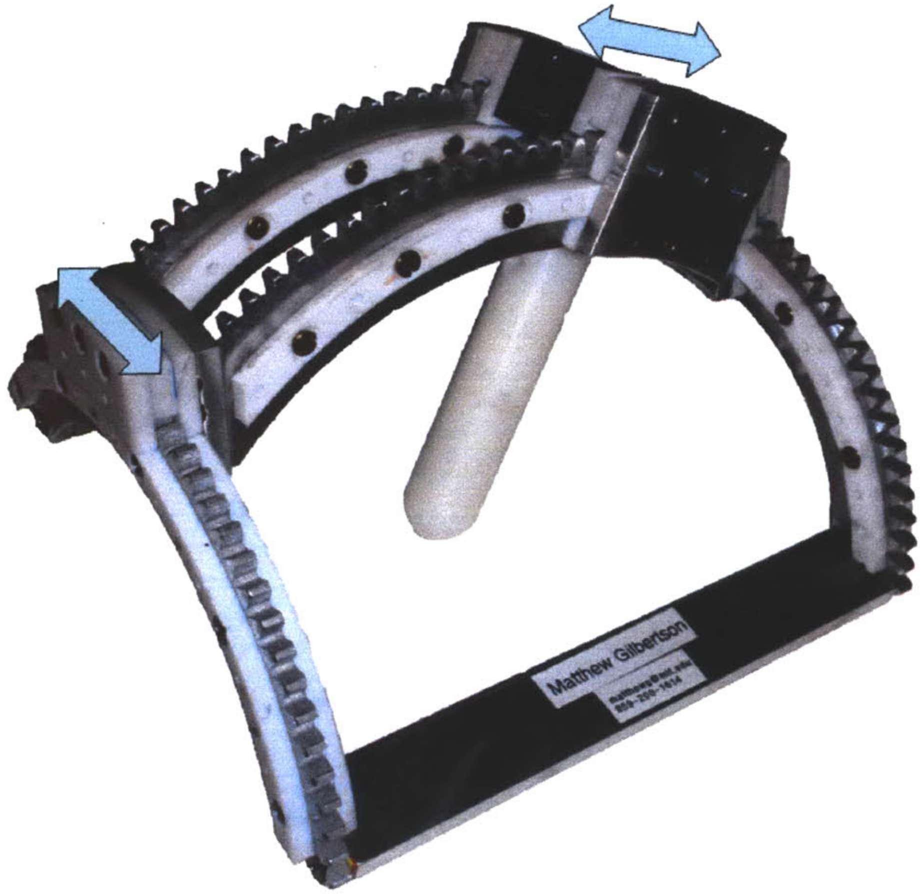

Figure 2-1: The SMF, with two rotational degrees of freedom.

an image and each desired configuration. Along with each image the control system would also record the position, orientation, and force at which each image was acquired. Using the position information a 3D image could be created. The goal of the device would be to replace the hand of the ultrasound technician for the purposes of generating high-resolution 3D images. After the first two prototypes were developed the focus of the project shifted to designing a one-DOF system that could simply control contact force, and this is described later in Chapter 3.

Other techniques have been used to construct 3D ultrasound images [12], in which a passive ultrasound probe is instrumented with a position tracking system to record the motion of the probe in the hands of a technician. However, an automated system could potentially be more rapid because it would choose an optimal path for gathering each image, instead of just relying on the orientations that the technician chooses to image at.

In designing the device we first investigated the typical hand motions of an ultrasound technician during an examination. We believed that the way in which the technician manipulates the probe could be inspirational in designing the degrees of freedom of the device. In a visit to Terason, Inc., an ultrasound technology company in Burlington, MA, we observed a real ultrasound examination. We observed that the imaging motions of the technician can be categorized into two scenarios:

1. Sliding the probe surface linearly across an area while maintaining orientation.

2. Rotating the ultrasound in pitch, yaw, and roll while maintaining a constant location on the patient's body.

Typically only one of these motions is performed at a time. Motion 1 is generally used to provide bulk motion of the ultrasound probe in order to locate a region of interest. For example the technician might use Motion 1 in imaging the arm in order to roughly locate a particular blood vessel. Once the blood vessel is located, the technician would then switch to Motion 2, in which he/she keeps the probe surface in a constant location while changing its orientation in order to look in different areas around the blood vessel. We termed Motion 1 "'Macro Motion" and Motion 2 "Micro Motion."

To reduce the complexity of the SMF while still providing valuable imaging capabilities we decided to focus on the Micro Motion. We assumed that either a human technician or a robotic arm would place the device in roughly the area of interest and that it would be up to the device to conduct the scanning. In a fixed position on the patient's body the device could perform elastography studies, in which an image is gathered at a range of forces to study the stiffness of the tissue. The force sensor should have approximately 0.1N of resolution or better in order to be able to accurately calculate the stiffnesses of the tissues.

2.1.2 Functional requirements of the Spherical Motion Frame

1. Safety. Above all, of course, the device must not pose a risk to the patient. There should be limits on the maximum speed and position of each axis. The device should thus monitor all three axes of force and three axes of torque in order to ensure that no force or torque is ever exceeded.

2. Backdriveable. The DOFs should be backdriveable so that if the device loses power it does not lock in a potentially harmful position (such as pinching the patient).

3. Fast. The device should be able to scan a particular body part in less than 60 seconds.

4. Accurate. The device must be able to measure the force to within 0.1N in order to provide the accuracy necessary for elastography.

5. Three intersecting rotational degrees of freedom. The Micro Motion requires three degrees of freedom for the ultrasound probe: pitch, yaw, and roll. It also requires that the center of rotation of the three axes be at the endpoint of the ultrasound probe. This would ensure that motion of any one of the DOFs would only result in an orientation change of the ultrasound probe.

6. Displaced center of rotation. The device must be capable of imaging numerous areas of the body such as the abdomen, arm, head, and neck. In order to fit into a concave area of the body such as the back of the leg, under the chin, or in the armpit area the device must have a center of rotation outside of the structure itself. Numerous devices exist that place the center of rotation of the axes within the device itself such as [25] [24], [9], [27], and [15]. But none of these would be suitable for imaging a concave area of the body. One functional requirement for the prototype was thus that the axes of rotation intersect outside of the device such as [10].

7. Small structural loop. The device needs to be localized on the patient's body in

order to provide for higher positional accuracy. In devices with a long robotic arm such as [14] or [28], if the patient moves during the imaging then there is a sudden loss of positional accuracy. In a device that is localized to the patient's body the device moves with the patient and positional accuracy is maintained.

8. Independent, parallel degrees of freedom. In order simplify the control of the device and decrease the necessary accuracy of the position encoders it is necessary to avoid "stacked" degrees of freedom. In a 6-DOF robotic arm such as [14], the base actuator must carry the other five actuators. The positional accuracy of the endpoint is thus the sum of the accuracies of each of the individual joints. This requires each joint to have locally higher positional resolution and the entire device to be stiffer, factors which increase the cost of the device. In addition, with [14] in order to conduct a simple pitching motion with the ultrasound probe all six degrees of freedom will likely need to be actuated synchronously. For these reasons it would thus be appealing if the device could have all of the actuators fixed in the same position and that driving one single actuator would result in a useful motion of the endpoint.

9. At least $\pm 50\,^{\circ}$ of rotation in both pitch and roll axes, along with $\pm 180\,^{\circ}$ in yaw and 3 inches of linear travel. These were found to be the typical ranges of motion of the ultrasound technician during an abdominal exam that we observed.

10. Be capable of applying at least the following forces and torques shown in Table 2.1, representative of a carotid artery exam:

Forces			Torques		
F_x	F_y	F_z	τ_x	τ_y	τ_z
±3.8N	±4.2N	±6.4N	±0.4Nm	±0.7Nm	±0.1Nm

Table 2.1: Maximum contact forces encountered during a typical carotid artery ultrasound examination [28]. DOFs refer to Fig 2-2.

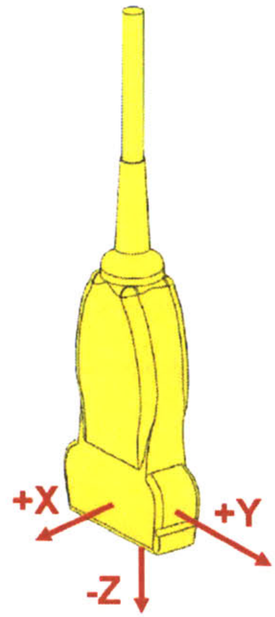

Figure 2-2: Degrees of freedom of the ultrasound probe.

2.1.3 Spherical Motion Frame: Design of a Dual Remote Center of Motion System

With these functional requirements in mind we developed the six motion concepts shown in Fig 2-3 (shown without actuators):

Concept A: Semicircular arm. Two rotational DOFs with intersecting remote centers. Biologic object shown with center of curvature placed at remote center of device.

Concept B: Two curved tracks. Remote centers interest *inside* device.

Concept C: Two curved tracks. Remote centers interest *outside* device.

Concept D: Two curved tracks. Remote centers interest *outside* device.

Concept E: 3D linkage with ball and socket joints.

Concept F: Two curved tracks. Remote centers interest *outside* device. Biologic object shown with center of curvature placed at remote center of device.

We next created the following FRDPARRC sheet to evaluate the six designs.

Device F was chosen because it satisfied the functional requirements better than the other five designs. Device F achieves a true remote and displaced center of rotation

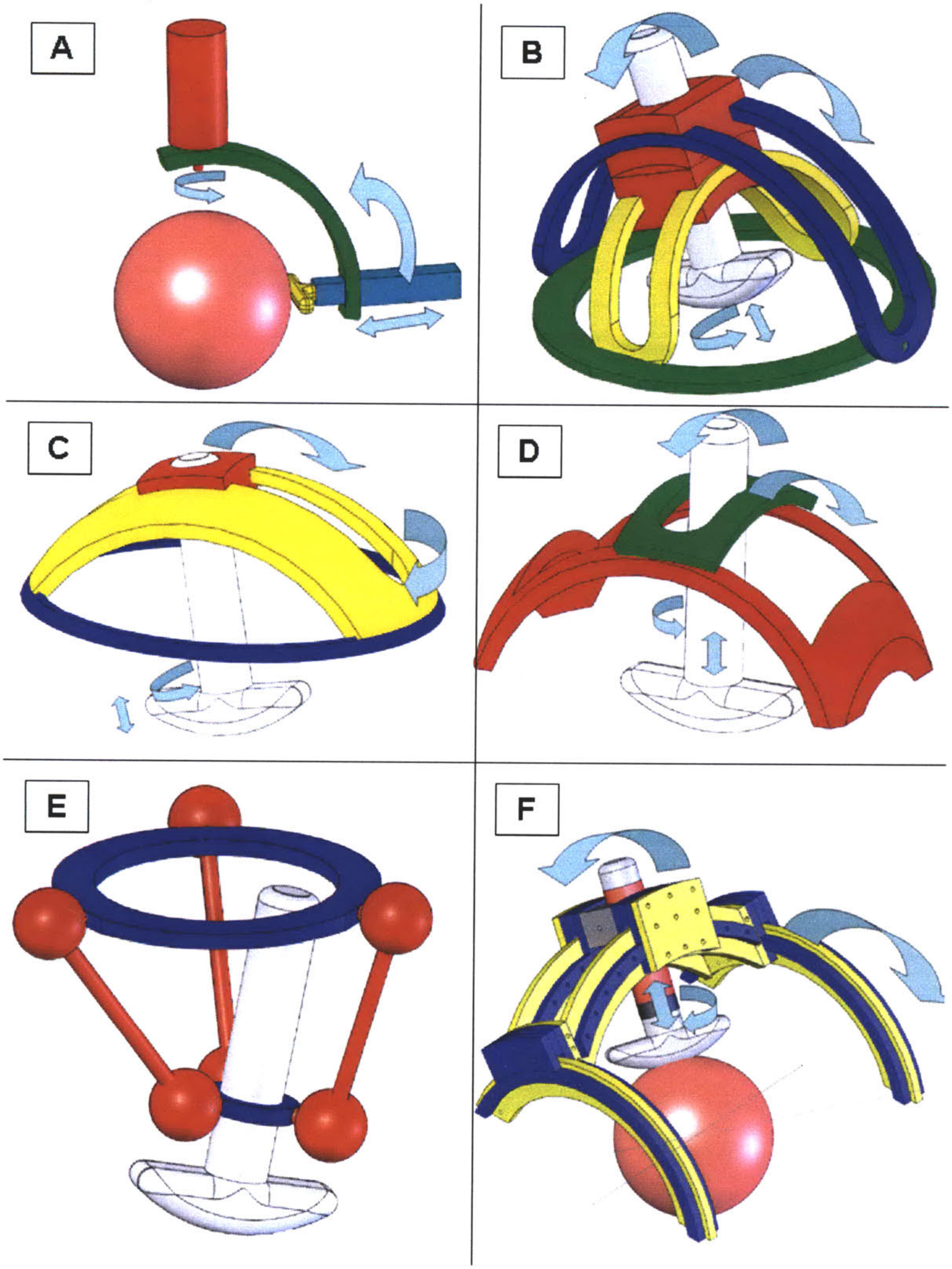

Figure 2-3: Concepts for SMF

Design Parameter	Analysis	References	Risks	Countermeasures
Concept A	Look at torque on motor axis	Simple physics	Too much radial load	One arm on each side for balance
Concept B	St Venant's to prevent binding	US Patent Application 2006/0229641 [15]	Can't image concave object	Only image convex objects
Concept C	St Venant's to prevent binding	FUNdaMENTALS book	Gimbal lock singularity	No obvious countermeasure
Concept D	St Venant's to prevent binding	FUNdaMENTALS book	Binding	Motor on each side
Concept E	Look at necessary actuator torque	Hexapod design? [30], Remote Center of Compliance devices [34]	Difficult to actuate, Doesn't have true remote center	Linear actuators to achieve remote center
Concept F	St Venant's to prevent binding	FUNdaMENTALS book	Binding	Motor on each side

Table 2.2: Evaluation of concepts for the SMF

unlike Designs E and B. Design B has a remote center of rotation but it is contained within the structure of the device itself. The 3D linkage of Device E is seen in other devices such as Remote Center of Compliance mechanisms [34] for peg insertion in non-aligned holes, but this device has only an approximate center of rotation. As shown in Fig 2-4 for a representative 2D 4-bar linkage, rotations of the endpoint link between about $\pm 10^\circ$ from vertical result in mostly rotational motions. Rotations greater than $\pm 10^\circ$ start to produce translational motions.

Thus a rotation of the ultrasound probe greater than $\pm 10^\circ$ would also mean translational motion of the probe endpoint. Since we require at least $\pm 50^\circ$ of rotation from Functional Requirement 8 along with independent degrees of freedom, Design E does not meet our functional requirements.

Device C achieves both a remote and displaced center of rotation but contains a singularity within its workspace, also known as "gimbal lock," which would eliminate a degree of freedom when the ultrasound probe is vertical. Device A achieves the

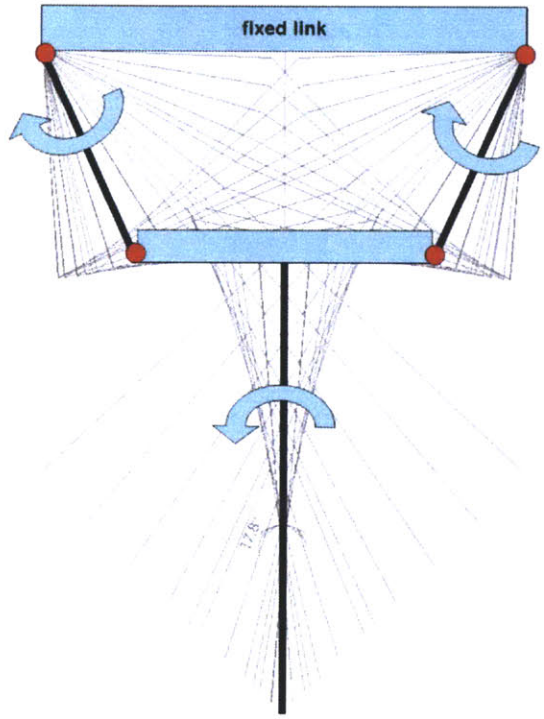

Figure 2-4: SolidWorks simulation of the motion of a 4-bar linkage. Pivot points are shown as red dots. The vertical black line ("output link") represents the ultrasound probe. Rotations of the input links causing greater than $\pm 10°$ of rotation of the output link would also lead to undesirable translational motion.

desired center of rotation but the necessary structural loop to anchor the device to the patient would be much larger than Device F, which could be placed directly on the patient, allowing it to move with the patient without losing positional accuracy. Because of its true displaced center of rotation, small structural loop, and singularity-free workspace Device F was selected for the SMF.

In creating a functional prototype from Device F we decided to first focus on the two curved degrees of freedom. Later prototypes could include the linear and rotational degree of freedom as well. In order to obey St. Venant's principle the width of the bearing surfaces needed to be greater than three times the width of the bearings. This would allow the stage to be actuated on one side without binding. The two arcs were about one-third of a circle, and the two arcs were placed with intersecting axes of rotation as shown in Fig 2-5. Since the arcs are less than one-half of a circle this allows the center of rotation to be placed outside of the device itself.

Materials: The main structure was machined from Aluminum due to its strength and low weight while Teflon (PTFE) was selected for the bearing surfaces due to its low friction. Bench level experiments later found that the friction coefficient between Teflon and machined aluminum was between 0.2 and 0.3. Most of the parts were machined using the very first OMAX Waterjet Cutting Center.

Fig 2-5 shows a solid model of the SMF along with a picture of the machined device. Both images depict the prototype without actuators. Future work would include adding two motors with gears, which would engage the gear pattern on each of the circular arcs and actuate the two degrees of freedom.

Advantages of the Spherical Motion Frame:

- Fully parallel degrees of freedom. Each of the two motors is fixed to the same part so that one motor is not "carrying" the other motor. In this way the two degrees of freedom are completely independent; the ultrasound probe can be translated without rotating it.

- Can image spherical objects using one DOF. In addition to providing the capability to image flat surfaces like the abdomen, this device would also be advantageous in imaging biologic objects with spherical geometry, such as at the head or breast. The linear degree of freedom could be moved and the entire device positioned so that the center of rotation of the two axes was the same as the center of curvature of the biologic object, as shown in Fig 2-6. In order to conduct a scanning motion in this configuration only one degree of freedom would need to be moved at a time and the device would maintain contact with the biologic object. This greatly simplifies the operation of the device.

2.1.4 Lessons learned from the Spherical Motion Frame:

- Large backlash in gears, especially with waterjetted gears.

- Making the bearing width more than 3-5 times the width of the rails satisfies

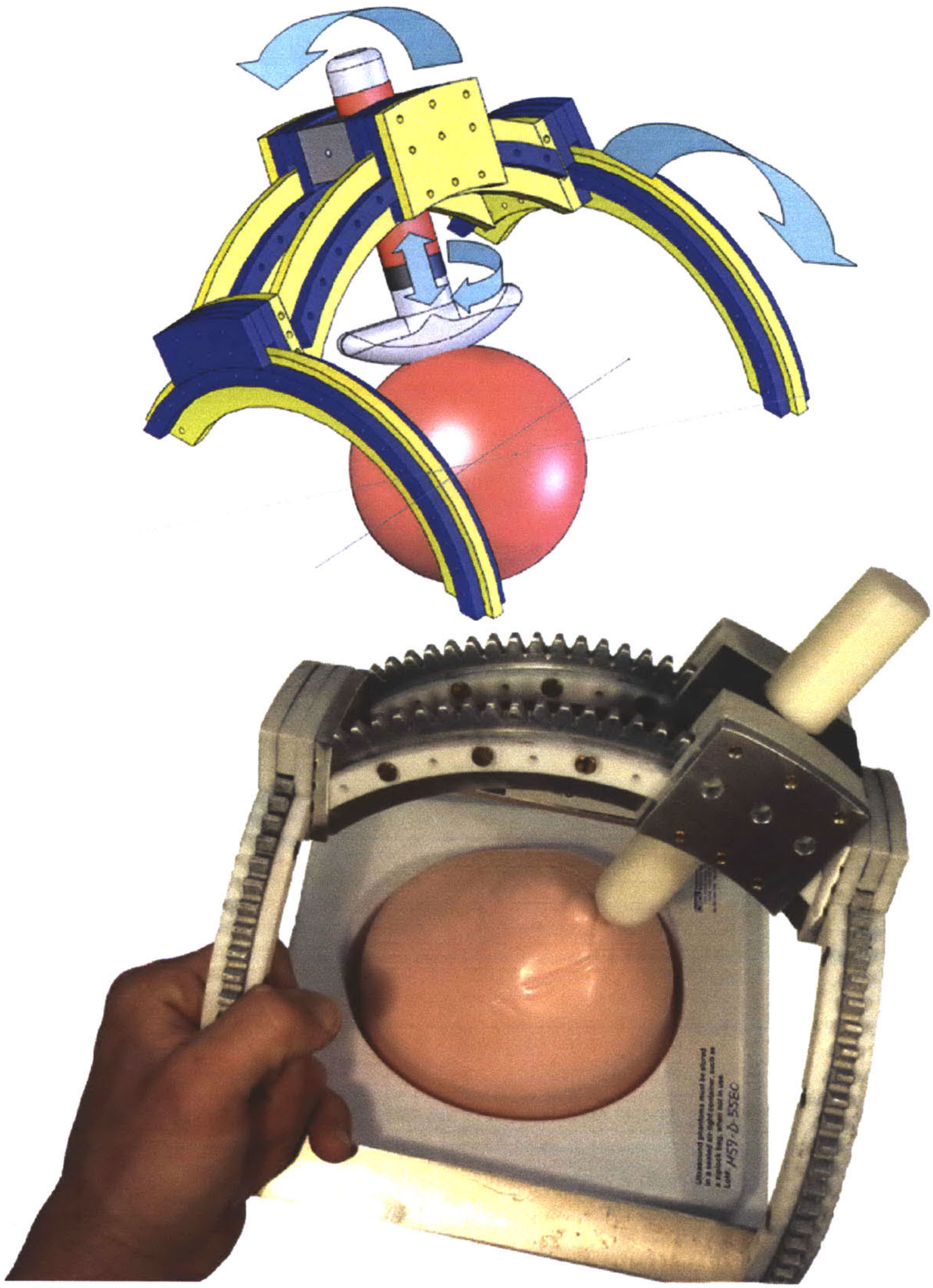

Figure 2-5: SMF: Solid model (top) and actual device (bottom), shown with breast phantom

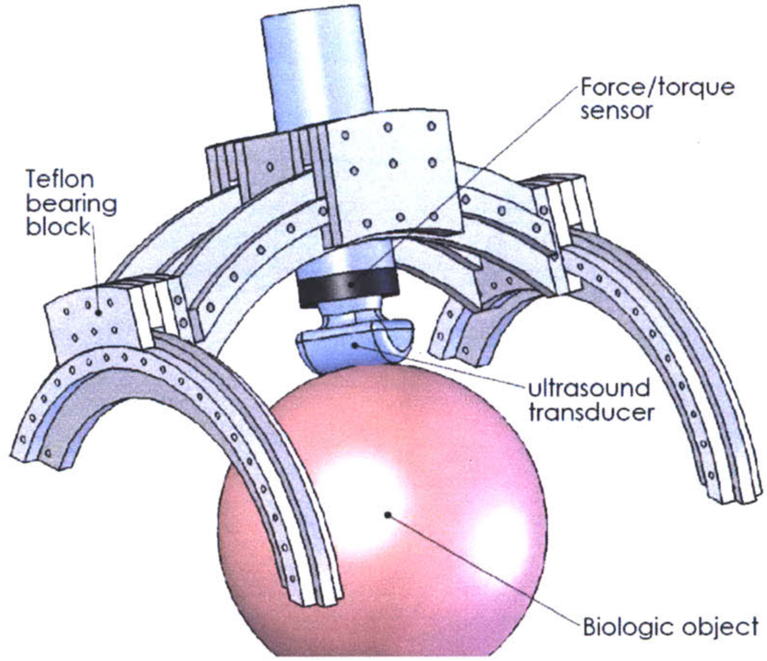

Figure 2-6: Solid model of the SMF imaging a spherical biologic object

St. Venant's principle and indeed prevents the axes from binding. As a result each axis only needs one motor.

- Difficult to deal with waterjetted parts due to the taper. Parts should be mated with opposing tapers.

- Teflon is very compliant and sometimes difficult to hold properly in the vise. It also deforms easily and introduces some compliance into the system, which also decreases positional accuracy.

- Mass = 1450g without motors.

2.1.5 Potential new directions of the Spherical Motion Frame

The following two concepts were considered as potential modifications to the SMF, but were not built.

Linear Scanning Axis: The dual remote center of rotation design of the SMF would be most appropriate for scanning biologic objects of spherical geometry, or for rotating the ultrasound probe about its endpoint on flat surfaces. It might be appropriate to adapt the geometry in order to image cylindrical body parts like the arm, leg, or neck. Fig 2-7 shows a different concept that replaces one of the rotational DOFs of the SMF with a linear DOF, allowing the device to scan down the length the arm, for example, while still providing the ability to change the orientation of the probe.

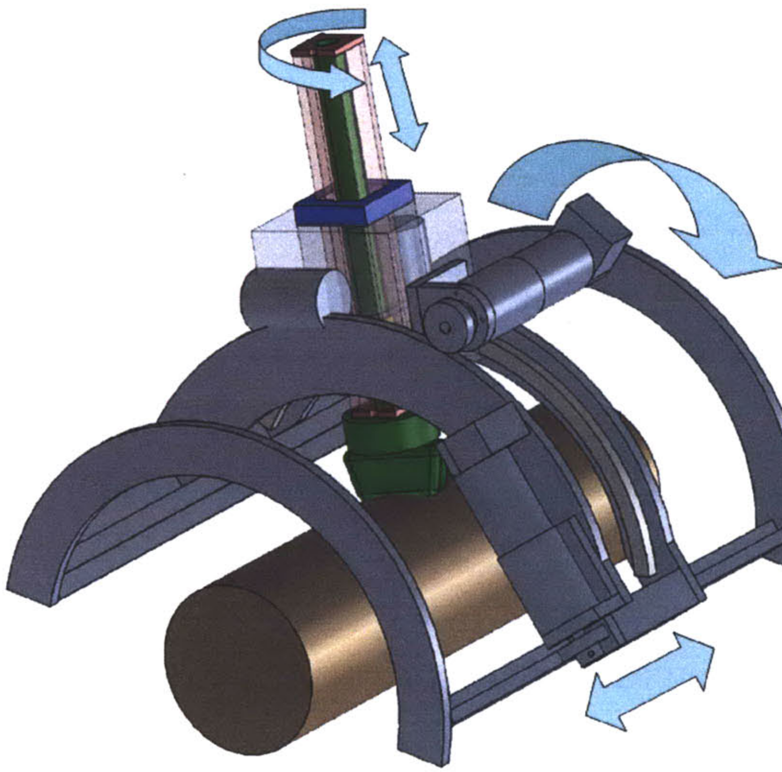

Figure 2-7: Linear + rotational DOF concept for a potential future prototype, which would be used in imaging cylindrically-shaped biologic objects.

Varying the center of rotation with actuated standoffs: The addition of linear actuators at the bottom of the SMF would enable the positioning of the centers of rotation of the axes and could increase the versatility of the design in imaging different areas of the body. The current design could be placed directly upon the patient to image the breast, for example. The center of rotation of the device would coincide with the approximate center of curvature of the breast, requiring the actuation of only one DOF at a time to conduct scanning along the tissue surface. But an additional mechanical modification to the device would be necessary in order to conduct scanning on other areas of the body. A linearly-actuated mechanical "standoff" could be used to place the center of rotation of the device at the desired location so that only one DOF is required to conduct scanning, as shown in Fig 2-8.

Description of the use scenario for each configuration:

Configuration A: Device rests directly on the patient. Standoffs (not shown) are fully retracted. Ultrasound probe is extended in radial direction. This places the center of rotation of the device on the surface of the patient, would be used for scanning in place, and would be used to image flat surfaces like the abdomen or back.

Configuration B: Device rests on patient. Standoffs (not shown) are fully retracted. Ultrasound probe is retracted in radial direction; remote center of rotation is placed at center of curvature of biologic object. Sweeping along the surface requires actuation of only one DOF at a time.

Configuration C: Mechanical standoffs extended slightly, this allows device to be swept across the surface of curved object like the arm or leg.

Configuration D: Mechanical standoffs extended fully, allows in-place scanning of arm or leg.

2.2 Cylindrical Motion Frame (CMF)

The goal of the CMF was to design the compact linear + rotational degree of freedom that could either fit in the SMF or by itself in the ultrasound technician's hand. The same functional requirements of safety, speed, accuracy, small structural loop, and parallel degrees of freedom were applied in the design of the CMF. Fig 2-9 shows six motion concepts considered for the linear + rotational stage (shown without actuators):

Concept A: Backdriveable screw. Rotational motion: axial constraint (not shown) holds screw in place while gear rotates. Axial motion: axial constraint disengages, gear rotates.

Concept B: Two Omni wheels oriented perpendicularly. Rotational motion: left wheel stationary while right wheel rotates. Linear motion: left wheel rotates while right wheel stationary.

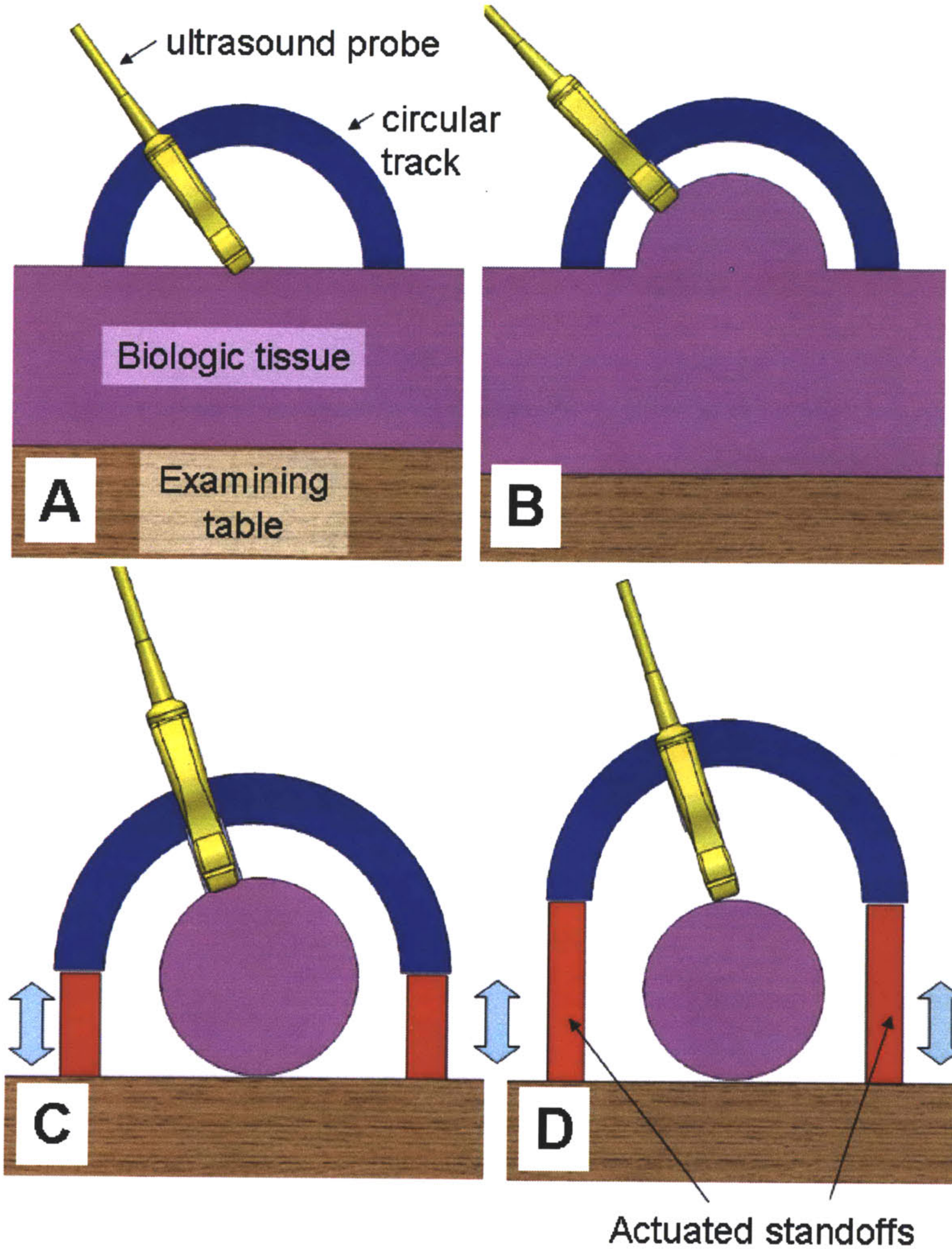

Figure 2-8: Using actuated standoffs to place the center of rotation of the circular track at the center of curvature of the body part.

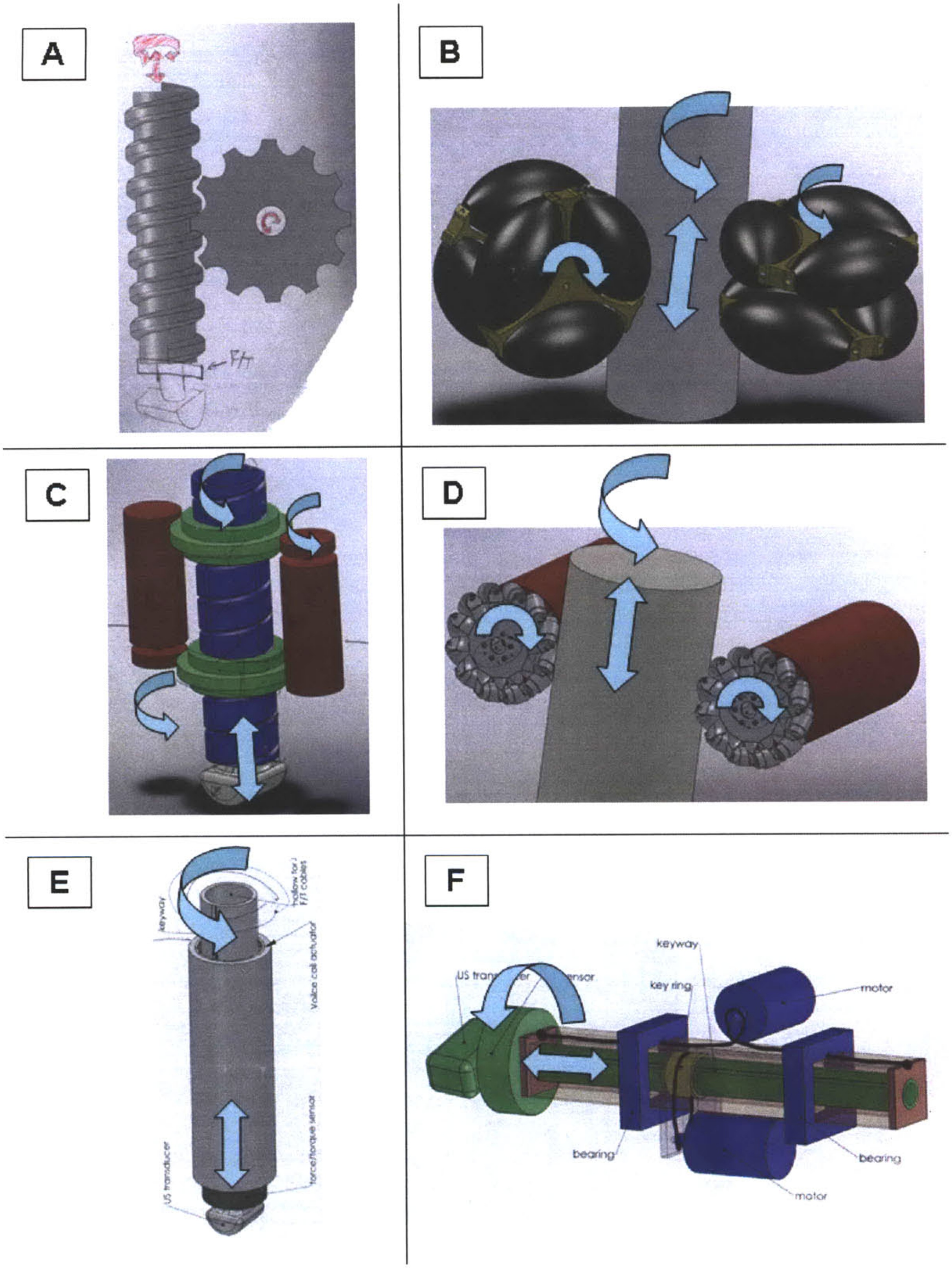

Figure 2-9: Concepts for the CMF

Concept C: Screw-spline. Rotational motion: both motors rotate in same direction. Linear motion: spline motor stationary while screw motor rotates.

Concept D: Two Meccanum wheels oriented parallel. Rotational motion: both wheels rotate same direction. Linear motion: wheels rotate in opposite directions.

Concept E: Voice coil actuator. Current is run through stationary coils to control linear position of shaft connected to permanent magnet. Rotational motion accomplished by motor engaging shaft's spline.

Concept F: Ultrasound connected to shaft which has spline. Rotational motion: one motor rotates a key-ring which engages the spline. Linear motion: motor rotates, translates ultrasound shaft. Permits independent rotation and translation and allows both motors to be fixed with respect to each other.

Table 2.3 shows the FRDPARRC sheet used to evaluate the six designs.

Design Parameter	Analysis	References	Risks	Countermeasures
Concept A	Look at screw pitch and friction coeffs	Bobbin winding devices	Tough to disengae axial constraint, too much friction and backlash	No obvious countermeasure
Concept B	Frictional analysis to prevent slip	US Patent 3,876,255 [20]	Slip, complexity	High friction interface
Concept C	St Venant's for bearing spacing	FUNdaMENTALs book	Dependent DOFs	No obvious countermeasure
Concept D	Frictional analysis to prevent slip	US Patent 3,876,255 [20]	Slip, complexity	High friction interface
Concept E	Calculate current to hold force	Numerous VCA vendors [5]	Too much power, too heavy	Smaller voice coil actuator?
Concept F	St Venant's for bearing spacing	FUNdaMENTALs book	Far apart bearings	Spline

Table 2.3: Evaluation of concepts for the CMF

Concept F was chosen because of its relative simplicity and independent DOFs. This design also presented the opportunity to use a low-backlash cable drive system

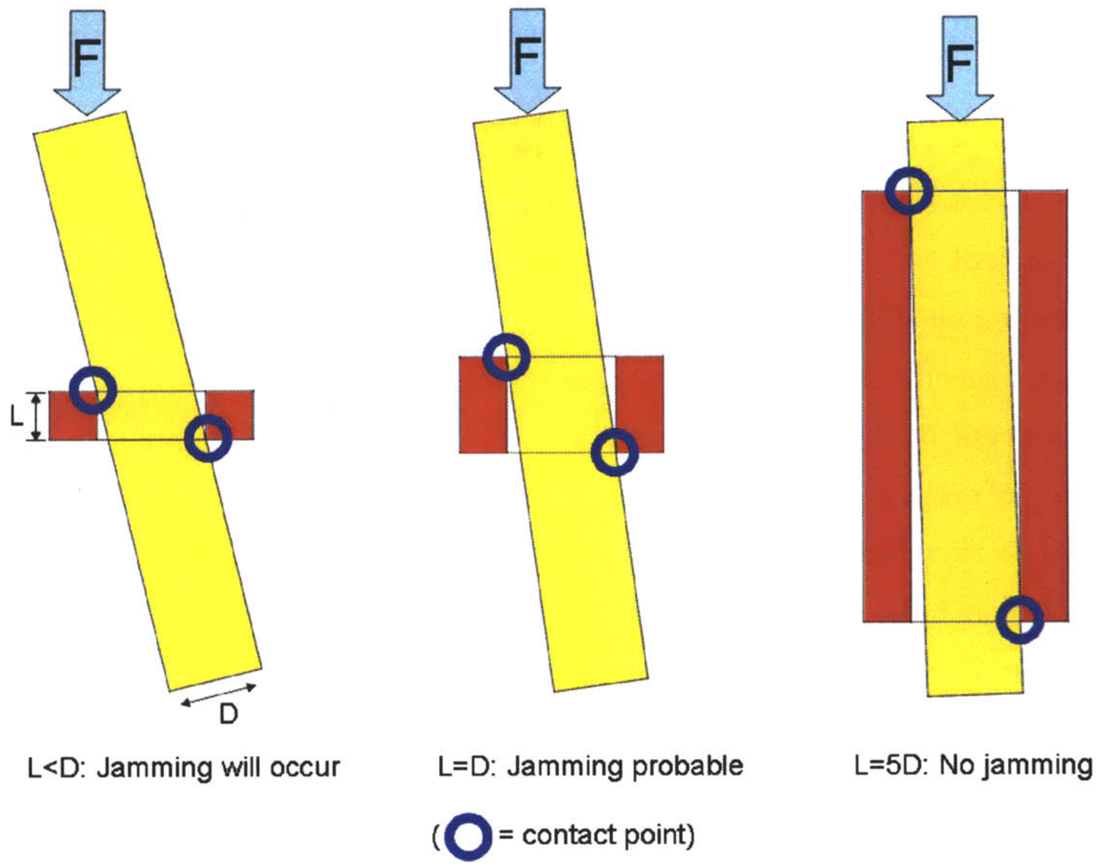

Figure 2-10: By St Venant's principle the bearing thickness L (dark color) needs to be at least 3 to 5 times the shaft diameter D to prevent jamming for an applied linear force F.

rather a more conventional but higher backlash rack-and-pinion or spur gear drive.

The challenge with any of these six designs was the need to space the bearings far enough apart to prevent jamming during linear motion. St Venant's principle for bearings means that for a sliding linear shaft of diameter D the bearings supporting the shaft should be spaced at least 3D to 5D apart to prevent jamming of the shaft, as shown in Fig 2-10.

2.2.1 Bearing design

Thus, for Design F, the bearings (shown in purple) need to be spaced apart by greater than 3 to 5 times the width of the linear shaft. Thus, if the shaft is one inch wide the bearings must be at least 3 to 5 inches apart (or one bearing 3 to 5 inches wide).

This problem becomes complicated by the fact that the ultrasound probe itself is on the order of 2 inches wide. If the design shown in Fig 2-9 Concept F was used, with the ultrasound probe placed in the middle of the tube, the tube would need to be at least 2 inches wide. Thus the bearings would need to be spaced at least six inches apart. If 3 inches of linear travel were desired the total shaft would thus need to be 9 inches long. It was decided that a 9-inch long shaft would be too cumbersome for an ultrasound technician to manipulate with enough dexterity to conduct a proper ultrasound examination. It became necessary to investigate designs that would reduce the necessary bearing spacing in order to decrease the overall size of the device.

Spline devices like the one shown in Figure 2-11 have the advantage that they can support linear motion of the shaft (shown in red) while also being able to rotate the shaft. As long as the length of each spline tooth is greater than 3-5 times the width of the tooth and the tooth is strong enough to support the loads, then the design satisfies St Venant's principle and will not jam during linear motion of the shaft.

This spline shape enables us to reduce the overall size of the device by reducing the necessary bearing spacing. The evolution of the design for the CMF using the spline concept is shown in Fig 2-12.

2.2.2 Cable drive system

The goal of this device is to enable 3D image reconstruction. The device would gather ultrasound images at a range of different positions, recording the positions with each image during the scan. After the scanning is complete the images could be compiled and, using the position information, a 3D image could be reconstructed in a process known as image registration. To perform high-quality image reconstruction the device must then have high positional accuracy. Several different types of drive mechanisms were considered for the CMF.

Gears are readily available and easy to attach to motor shafts, but exhibit backlash if not preloaded properly. Any backlash would decrease the positioning accuracy of the ultrasound probe. Belt drives are also appealing for their simplicity and compactness but some belts tend to stretch and, which effectively leads to backlash. High-frequency

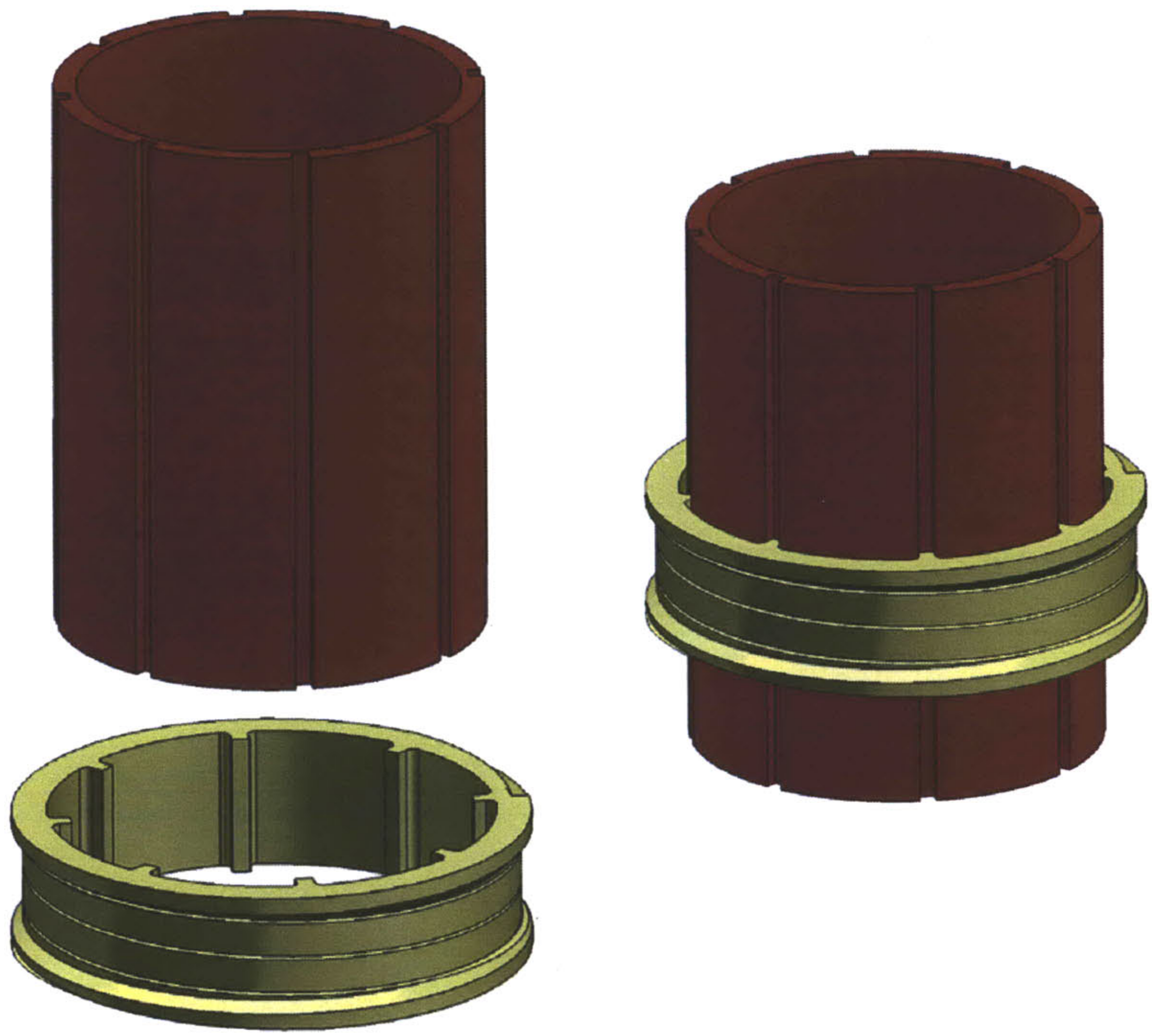

Figure 2-11: Spline and ring used to provide rotational motion while allowing translation

back-and-forth motion of the motor would cause any stretch in the belt to result in a loss of position accuracy. Cable drives, on the other hand, have been used successfully to provide highly compact, low-backlash drive systems in numerous devices such as photocopiers [21], micro surgical robots [22], and precision rotary positions systems [7]. Because of their compactness and high positioning accuracy we chose to design a cable-drive system for the CMF.

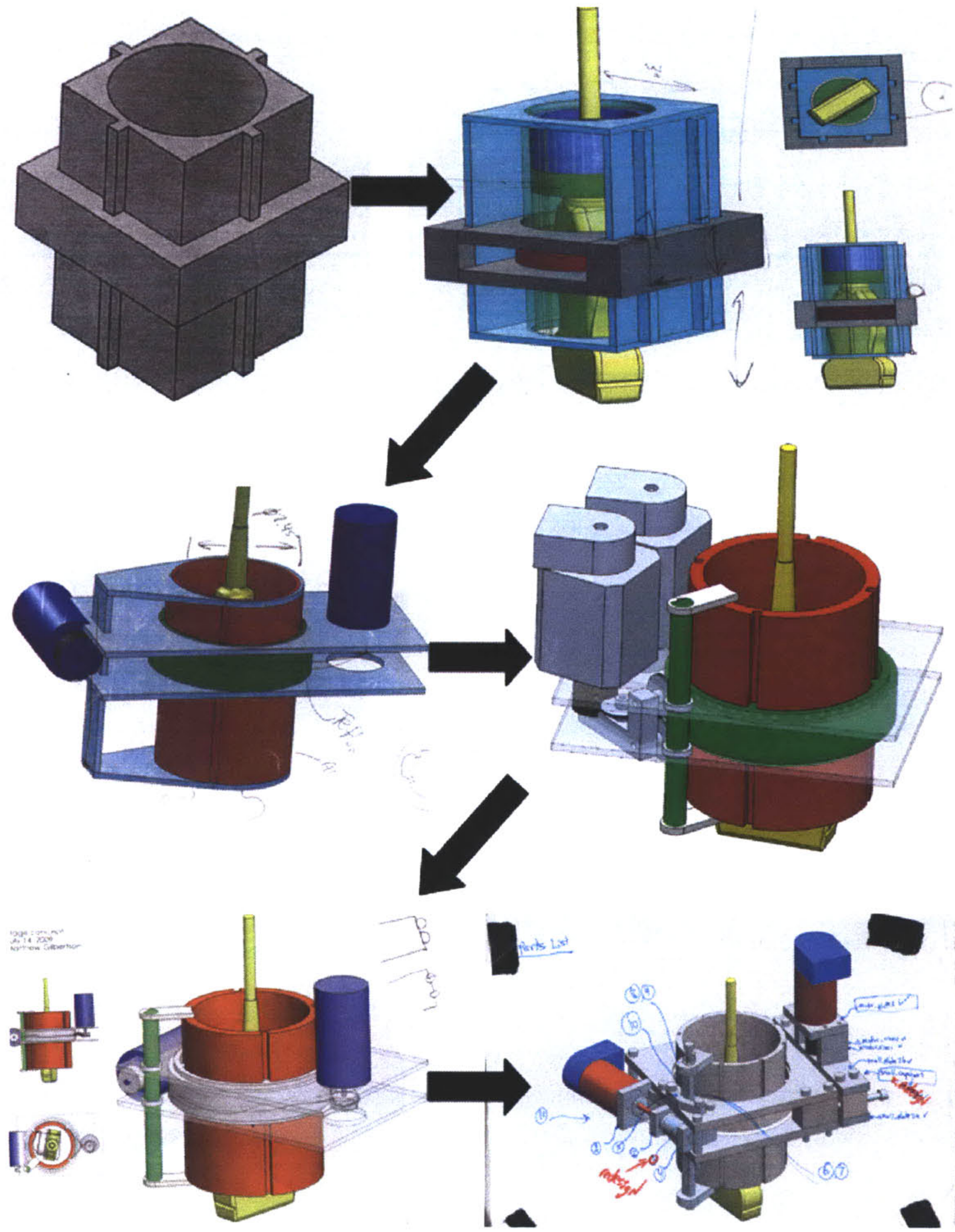

Figure 2-12: Design evolution of the CMF

2.2.3 Capstan effect

Cable drive systems take advantage of what is called the "capstan effect". The capstan effect occurs when a string, cable, or chain is wrapped multiple times around a cylinder and tensioned at each end. The more wraps, the higher the difference between the two tensioning forces can be without the cable slipping. This effect is sometimes used in large ships to raise the anchor. The anchor cable is wrapped a few times around a cylinder called the capstan. Crew members rotate the capstan to draw the cable in while one crew member maintains a small amount of tension on the other end of the cable to keep it from slipping. This allows the anchor to be raised without the cable ever being connected rigidly to the ship. In the same way a steel cable for example (also referred to as wire rope) wrapped over an Aluminum cylinder and tensioned on one side T_1 as shown in Fig 2-13 exhibits a different cable tension on the other side T_2 due to friction between the cable and capstan.

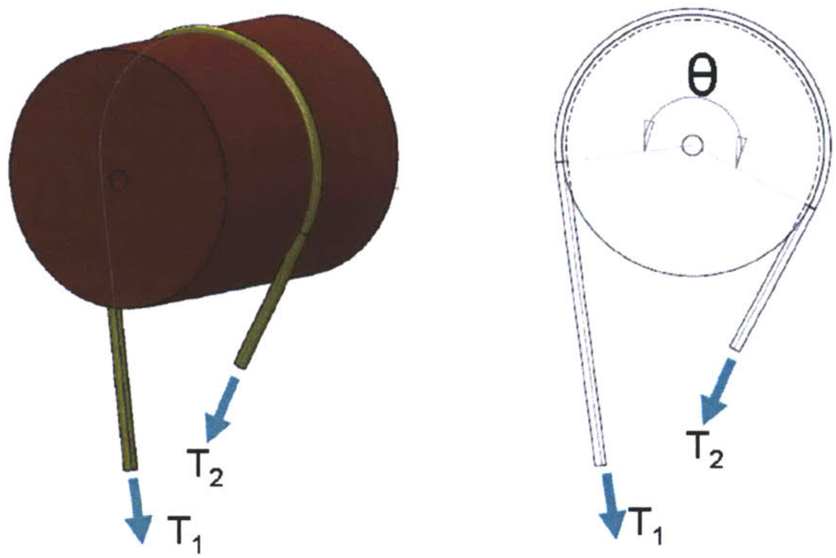

Figure 2-13: Increasing the wrap angle increases the difference between T_1 and T_2

For a cable wrapped at an angle θ around a capstan with frictional coefficient μ and with a tension T_2 applied on one side of the cable, the tension T_1 must satisfy the following inequality to prevent slip:

$$T_2 e^{-\mu\theta} \leq T_1 \leq T_2 e^{-\mu\theta} \tag{2.1}$$

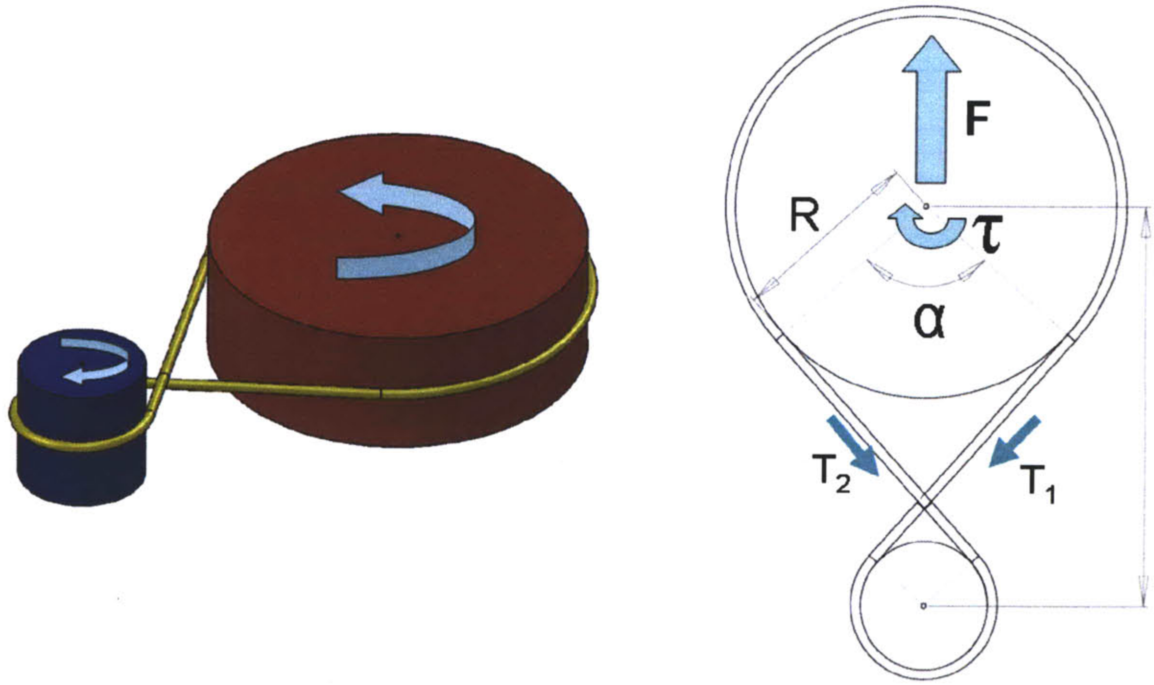

Figure 2-14: Figure-8 wrapping strategy

This means that if the tension T_1 is too small, then the cable will slip in the direction of T_2. On the other hand, if T_1 is too large then the cable will slip in the direction of T_1.

In cable drive systems, one capstan is often used to drive another capstan as shown in Fig 2-14. The capstans can have different diameters to enable speed reductions.

The cable is typically wrapped in a Figure-8 configuration and the two ends are joined together. The Figure-8 configuration increases the wrap angle and thus the cable-capstan friction force. In this configuration it is necessary to hold the two capstans apart with a force F to prevent the cable from slipping when torque is applied to one capstan.

Assume the small capstan is held stationary while torque is applied to the large capstan. A constant force F holds the two capstans apart. We would like to know the maximum torque that can be applied to the large capstan before the cable starts to slip. Using Equation 2.1 above, the slip torque is

$$\tau_{slip} = min\left(\frac{R_1 F}{sin(\frac{\alpha}{2})} \cdot \frac{1 - e^{-\mu\theta_1}}{1 + e^{-\mu\theta_1}}, \frac{R_2 F}{sin(\frac{\alpha}{2})} \cdot \frac{1 - e^{-\mu\theta_2}}{1 + e^{-\mu\theta_2}}\right) \tag{2.2}$$

Where θ_1 and θ_2 are the wrap angles of the two pulleys, R_1 and R_2 are the radii of the two pulleys, and α is the angle between contact points of the string. The minimum function means that slip will occur if the cable slips on either capstan. This equation can be used to design a cable-drive system that will not slip under the expected loads.

2.2.4 Cable properties

For the CMF we chose to use Kevlar thread instead of the more conventional steel cable because of its ability to bend to smaller radii. Many cable-drive systems employ stainless steel cable for its high strength and (weather) resistance. Cable manufacturers such as Sava Industries recommend a minimum cable bend diameter of 40 times the cable diameter. Thus, for a 32kg tensile strength steel cable of diameter 0.61mm, the minimum recommended bend diameter is about 24mm or about 1".

In the CMF it was desired to drive the rotational DOF with a 6:1 speed reduction from the motor. If steel cable were used this would mean that the large capstan needs to have a diameter of 146mm-about 6". This is prohibitively large for a handheld device. We chose instead to employ Kevlar thread, which can bend to a much smaller diameter than steel.

Kevlar thread has about the same tensile strength as steel for a given thread diameter. Through bench-level experiments we found that a 0.63mm Kevlar thread can be bent to a minimum diameter of about 3.2mm without the strands coming apart, which is about 5 times the cable diameter. Thus a 6:1 reduction would require a large capstan of diameter 16mm-about 0.63". Thus Kevlar thread enables us to reduce the overall size of the device because it can be bent to a smaller radius.

Although Kevlar thread is appealing for its tight bend radius it is considerably less durable than steel cable. We found that after about 100 rotations of the Kevlar thread about a small-diameter Aluminum capstan the yellow thread began to discolor

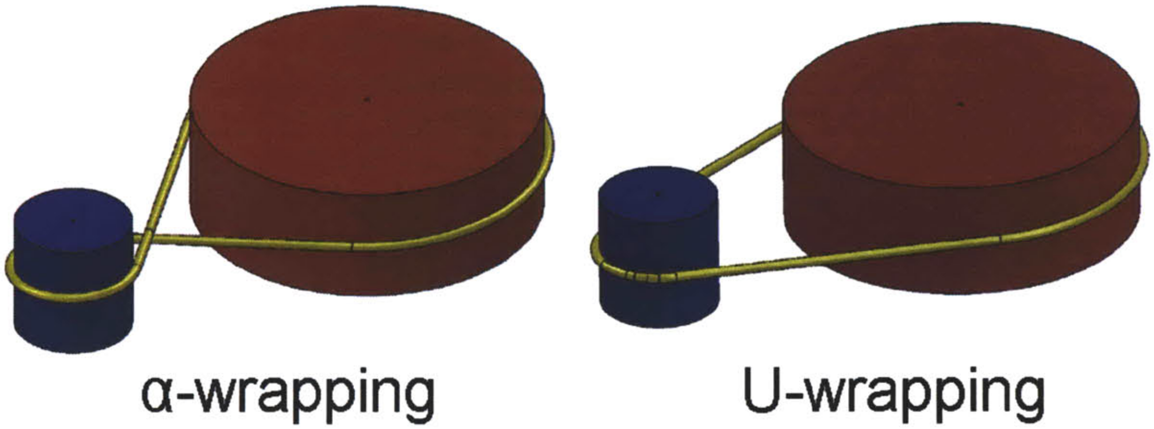

Figure 2-15: Two wrapping strategies. Alpha-wrapping enables more wraps around each capstan, increasing the available input torque

and the individual strands began to separate. However, we did not observe any of the threads failing in tension. For the CMF we chose to build a smaller device at the expense of thread durability and thus chose to use Kevlar thread.

2.2.5 Cable Wrapping Strategies

In designing the cable drive system we found that extreme care must be taken to ensure that the string wraps properly around the capstans. Two possible wrapping strategies are shown in Fig 2-15.

The wrapping scheme on the left shows so-called "α-wrapping" because the cable enters and exits the capstan in the shape of the Greek letter alpha [22]. (For a good discussion of cable-drive systems, refer to Akhil Madhani's PhD thesis: [22]). We shall similarly call the wrapping scheme on the right "U-wrapping". U-wrapping is perhaps the simplest capstan-to-capstan wrapping strategy because it permits continuous rotation. If it is desired to increase the number of wraps around each capstan in order to increase the friction then U-wrapping turns into α-wrapping.

We discovered that the biggest challenge with α-wrapping is a phenomenon we call "string wander," which occurs during rotation when the cable tries to climb on one capstan while descending on the other capstan. This greatly increases the force in the cable and causes it to start wrapping over itself, and eventually becomes tangled.

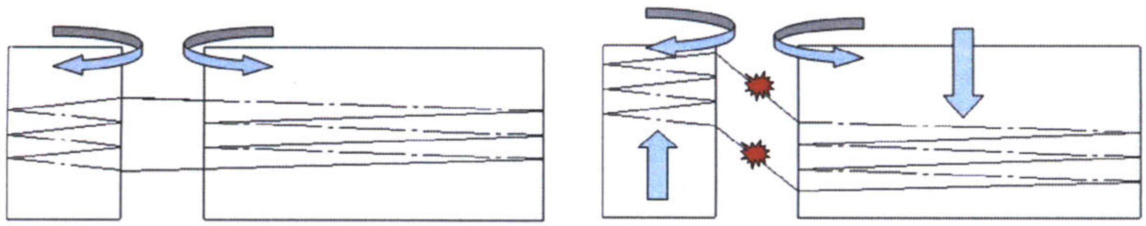

Figure 2-16: Wrapping with the same handedness on both capstans leads to differential string wander, which could cause the string to tangle or break.

The problem arises because the two capstans are rotating in opposite directions but the thread is wrapped with the same handedness (right-hand thread or left-hand thread) on each of them. The α-wrapping in Fig 2-15 shows both capstans with the thread wound in a right-handed manner, the same as most screw threads. When the small capstan rotates clockwise (as viewed from the top), the thread will rise up on the small capstan. As the same time the red capstan will rotate in the opposite direction-counterclockwise and thus the thread will tend to fall on the capstan. This will cause a differential movement of the thread as shown in Fig 2-16, leading to wrapping problems because the thread cannot elongate more than a few millimeters without breaking.

This problem of differential string movement is compounded by the fact that the capstans rotate at different rates. For example, if the larger capstan has a diameter six times that of the small capstan, it will rotate at one-sixth the rate of the smaller capstan. This means that if the thread is wrapped with the same pitch L on each capstan (spacing between threads), and right-handed on each capstan as well, for one rotation of the large capstan, the small capstan will rotate six times. In the meantime, the thread will rise on the small capstan by 6L, while falling on the large capstan by a distance of 1L. Through bench-level experiments we found that this naïve α-wrapping strategy will lead to string tangling and/or breakage. A new wrapping strategy was required.

We eventually created a wrapping strategy that would permit the capstans to rotate without the problem of string wander. First, the capstans must be wrapped with a different handedness because they rotate in different directions. For example, wrap the small capstan right-handedly and the large capstan left-handedly. Next, the pitches of the string wrapping must be related to the diameters of the capstans. If the small capstan diameter is D_{small} and the large capstan diameter is D_{large}, and the pitches of the wrapping on each capstan are L_{small} and L_{large}, then the following relation must hold to prevent differential string movement:

$$\frac{D_{large}}{D_{small}} = \frac{L_{large}}{L_{small}} \tag{2.3}$$

We found that in order to wrap the string with the proper pitch, it helps to machine threads into the capstans. Wrapping by hand is prone to error and can lead to extreme frustration. While not strictly required to machine threads in the capstans, it not only helps achieve the desired pitch, but also reduces the tendency of the string to flatten out, and reduces string wear and moving friction. The threads should be machined at a depth to hold one-third of the diameter of the string [22].

Wrapping the capstans with different handednesses introduces a new complication. The string can no longer be wrapped into a closed loop. The solution was to anchor the two ends of the string to the top of the large capstan, then wrap continuously downward, including the small capstan. Three of these wrapping strategies are shown in Fig 2-17.

We employed Method 3 of Fig 2-17 in the CMF because it was the only method that did not produce differential string movement. This strategy still results in string wander, but the string wanders by the same amount on both of the capstans. For example, if the small capstan is rotated clockwise (as viewed from the top), the string will rise on the small capstan while the string gap will rise on the large capstan at the same rate. Since the capstans have finite length, the angular range of motion of the capstans is limited. The capstans should not be rotated far enough to let the string derail on either side. Thus, the taller the capstans are the greater the range of motion.

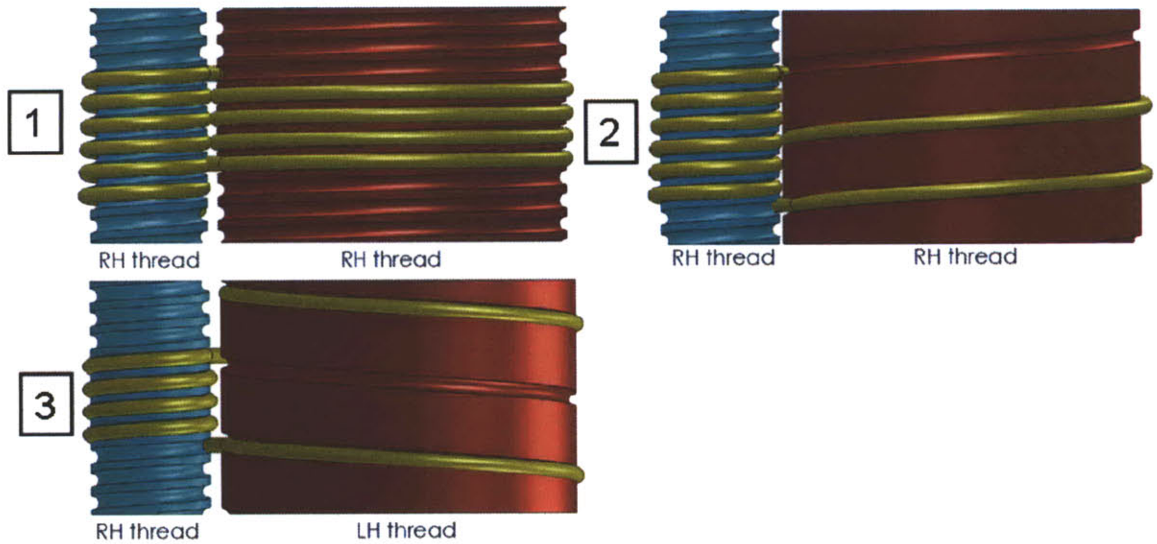

Figure 2-17: Three wrapping methods. Methods 1 and 2 result in differential string movement. We used method 3 in the CMF because it was the only method we discovered that did not result in differential string movement.

2.2.6 Tensioning system

From Eqn 2.2, the amount of torque that can be applied to the capstan without slippage increases as the tensioning force increases. Thus, the cable drive system must have a mechanism that allows the string tension to be increased. We found that the best assembly method was to first wrap the string then tension it properly. For the CMF we designed a screw-tensioning system that applied an approximate tensioning force F of 10N. The tensioning system is shown in Fig 2-18.

2.2.7 Materials Selection

The spline ring from Fig 2-11 has unique design requirements. It must be strong enough to transmit at least 1.0Nm of torque to the central spline tube (a 10X safety factor over the torque requirements in [28], while allowing the tube to translate linearly. It must accommodate for side loads of $\pm$4N (from Table 2.1) while satisfying St Venant's principle to prevent binding.

To simplify and expedite design of the prototype, we chose to use Teflon for the spline ring because of its low friction. This would permit the sandwiched ring to rotate

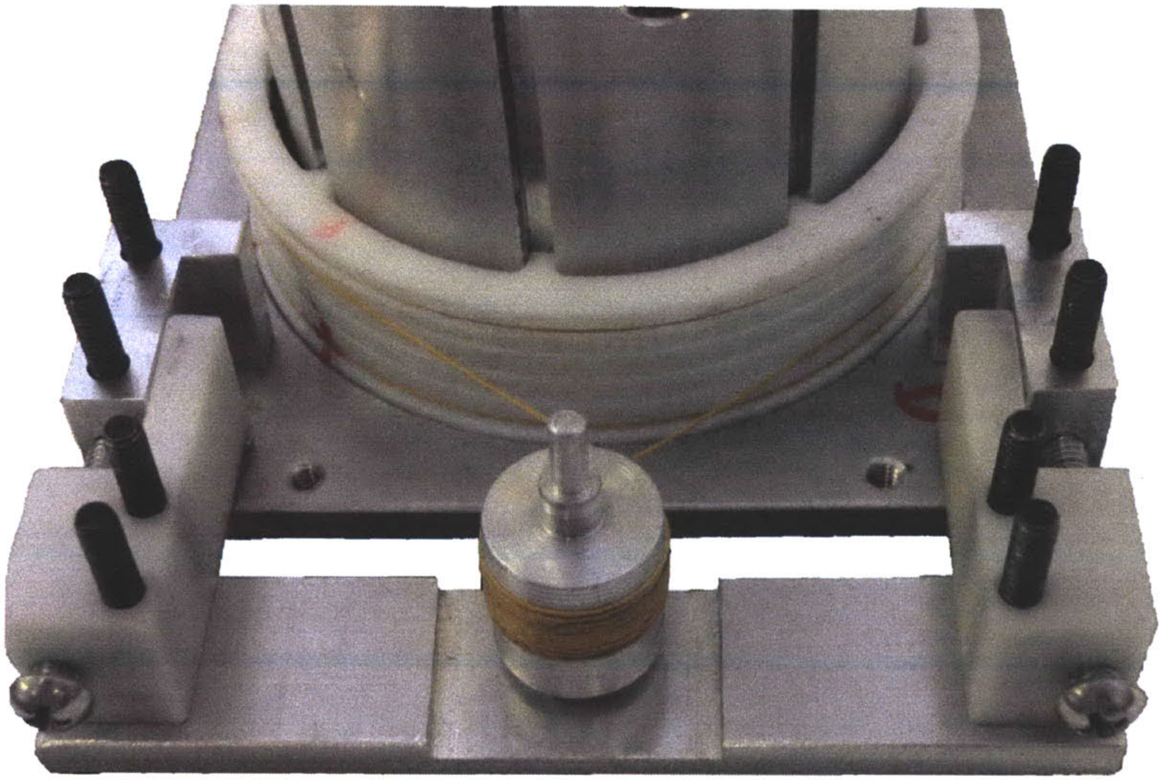

Figure 2-18: String tensioning system and wrapping scheme. By turning the screws the distance between the two capstans can be varied. The plastic (white) L-shaped piece is threaded and the screw makes surface contact with the other aluminum L-shaped block.

with low friction between the upper and lower plates, while allowing the spline to slide easily through the middle. Since, from wrapping Method 3, the string terminates on the ring itself, this does not need to be a high-friction interface. The small capstan was machined from aluminum because it exhibits higher friction with Kevlar thread and allows more torque to be applied without slipping

2.2.8 Linear DOF

We also applied a cable-drive system for the linear DOF to reduce backlash. A small capstan drives a linear shaft (essentially an infinite-diameter large capstan). The problem of string wander still occurs with the linear DOF but the string does not wander as far because it rotates through fewer rotations to drive the linear DOF to its limits. The small capstan was made from Aluminum, the same for the linear shaft.

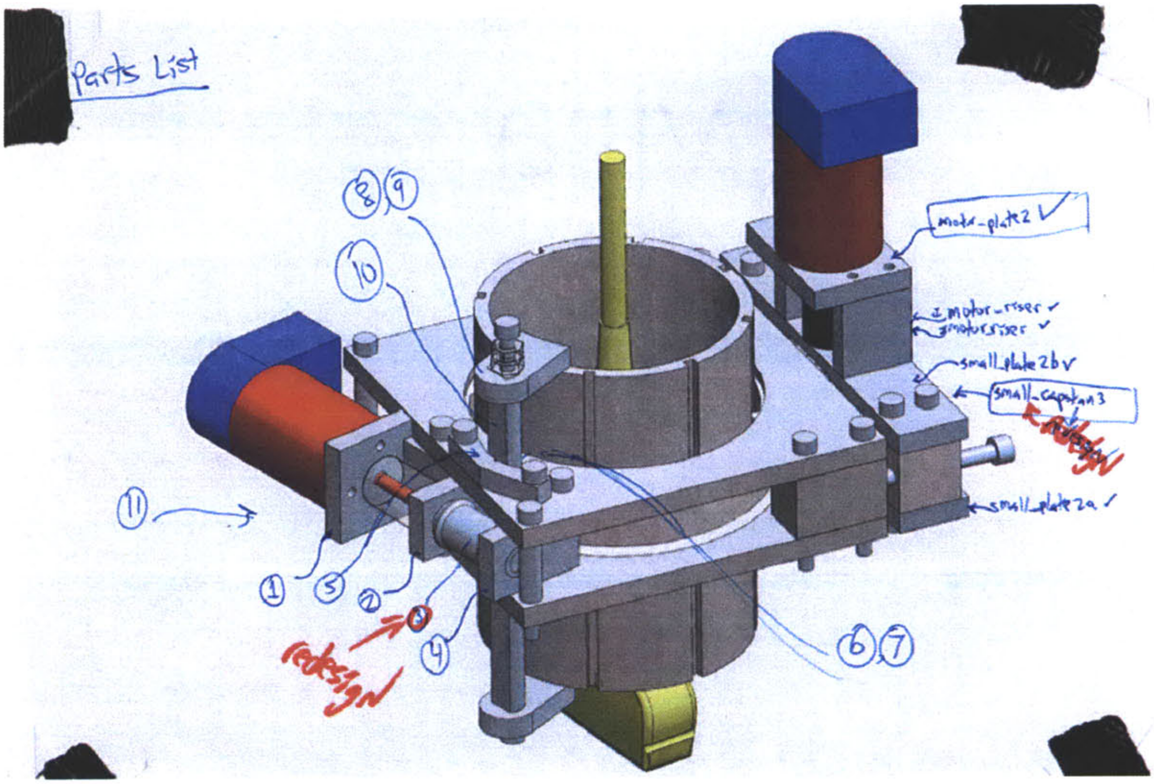

Figure 2-19: Solid model of the CMF.

A solid model of the CMF along with a photograph of the actual device are shown in Figs 2-19 and 2-20.

2.2.9 Results from the Cylindrical Motion Frame

The completed CMF was able to achieve two decoupled DOFs: one linear and one rotational. The prototype proved that the concept of using a cable-drive system is a promising way to reduce transmission backlash. Several specific lessons were learned:

- The spline shape indeed prevented the linear DOF from binding, but the softness of the Teflon spline ring made it very difficult to machine precisely. A slight non-parallelism between the top and bottom surfaces led to a slight "wiggle" between the ring and the top and bottom plates. The Abbé error amplified the wiggle into a 3 to 5mm movement at the tip of the ultrasound at full extension, which is unacceptably large for high position accuracy.

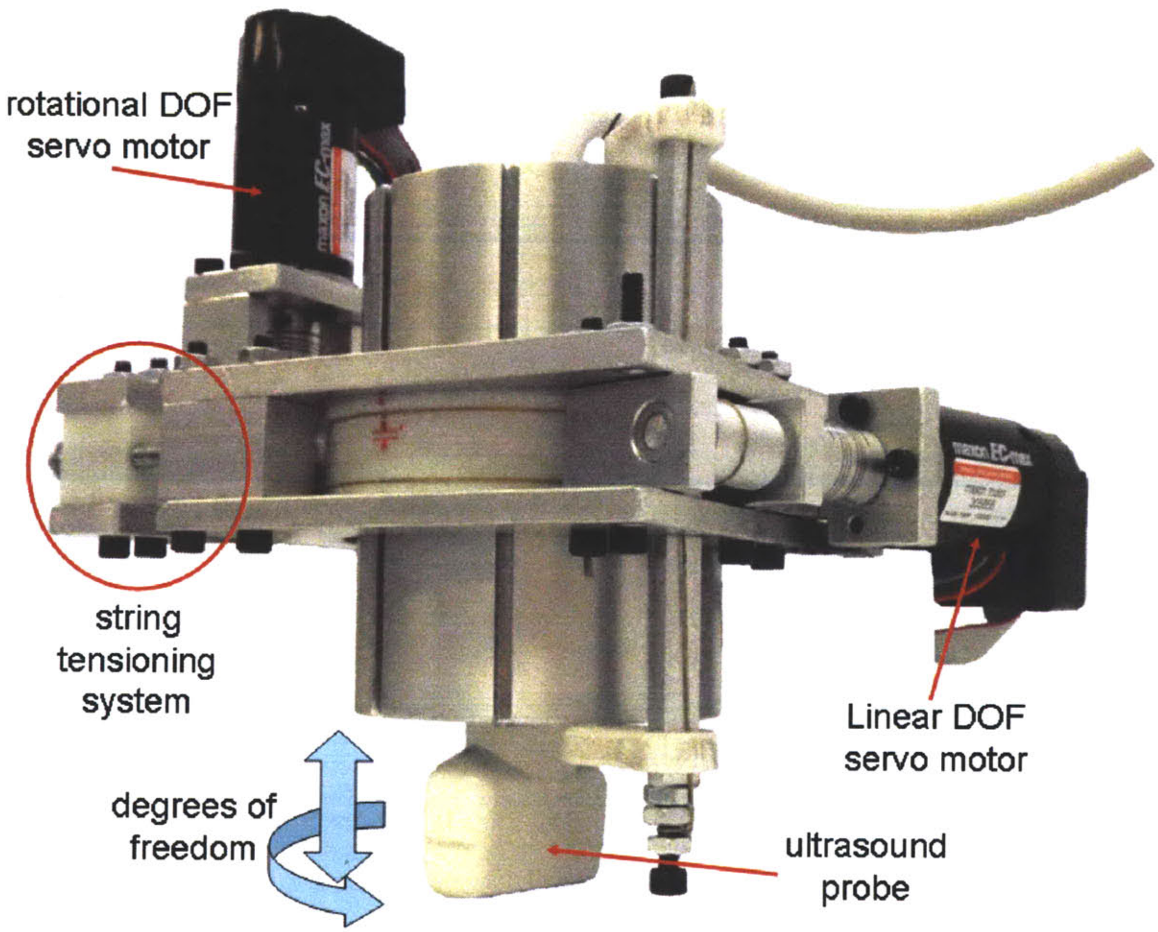

Figure 2-20: Photograph of the CMF

- Mass = 932g without motors, size: about 23cm x 18cm x 8cm. This device did not fit comfortably in a person's hand.

- Kevlar string will lay properly in a tight helix if there is enough tension and threads are machined into the capstans.

- Kevlar string can bend to a very small radius, on the order of 5 times the thread diameter (compared with 50x for steel cable), without unraveling.

- Teflon is very compliant, making it very difficult to machine the desired shape with tight tolerances.

- Loops can be made in the string with a simple square knot.

- Grooves in the capstans reduced the flattening of the string and seemed to increase its lifetime.

- For back-and-forth motion like this, care must be taken not to let the cable wrap over itself. By wrapping over itself the capstan effectively increases in diameter and tries to elongate the cable, which increases the tension. It also increases the likelihood that the cable will become tangled. This requirement makes the design of cable drive systems significantly more complex than simple one-direction cable wrapping schemes like those seen in car winches or fishing reels.

2.2.10 Future work for the Cylindrical Motion Frame

Although the device achieved the desire degrees of freedom, the overall size (roughly 23cm x 18cm x 18cm) and mass (932g without motors) made it extremely cumbersome to hold in a person's hand. Future work on the CMF includes making it much smaller and lighter so that a technician can dexterously manipulate it. Also, the sliding Teflon bearings should be replaced with higher-performance, tighter-tolerance ball bearings to decrease friction and position backlash.

2.3 Summary

This chapter described the design of two prototypes to vary the position and orientation of the ultrasound probe. The Spherical Motion Frame pivots the ultrasound probe about its center while the Cylindrical Motion Frame controls the 'spin' of the ultrasound probe as well as its linear position. The SMF demonstrated the effectiveness of teflon bearings in reducing friction and demonstrated that the two DOFs will not bind. The CMF showed that two independent, parallel, cable-driven degrees of freedom can provide linear and rotational motion for an ultrasound probe. Future work on the CMF would include reducing the size and mass while eliminating the backlash caused by the compliance of Teflon.

Chapter 3

Linear Motion Stage for Force Control

Since the two DOFs of the Cylindrical Motion Frame proved too cumbersome to fit into a technician's hand, and a linear DOF will be necessary for any future design, we decided to redirect our efforts into designing a high-performance single linear DOF. A robust version of the design could be integrated into future prototypes. The goal of the Force-Controlled Stage (FCS) was to create a handheld device that allows the ultrasound technician to apply a programmable contact force with the patient. This chapter describes the design of a single-DOF system to apply a constant contact force using a linear ballscrew actuator.

3.1 Six Concepts

The same functional requirements of safety, speed, low backlash, backdriveability, and accuracy from the Spherical Motion and Cylindrical Motion Frames applied in the design of the Force-Controlled Stage. Additionally, since the device will be held in a person's hand, it must compensate for any movement including hand tremors. Typical human hand tremor frequency starts at 7-12Hz and slows to 4-6Hz after 30 minutes of physical activity [19]. Thus the actuator will need to be capable of moving at well over 20Hz in order to be faster than the fastest tremor. From these functional requirements six concepts were generated, and are shown in Fig 3-1.

Concept A: "String and pinion." Cable-driven to reduce backlash. Motor capstan drives cable, which translates the linear DOF.

Concept B: Similar to Concept A, but this configuration allows the motor to be oriented parallel to the direction of motion, decreasing the size of the device. The light blue pulleys allow the cable to change directions.

Concept C: Spiral pulleys. Similar to Concept B, but the green pulleys contain a spiral shape to permit string wander. The motor capstan actuates the red string, connected to the spiral of the pulleys. The cylindrical parts of the pulleys engage the purple string, which move the ultrasound probe back and forth.

Concept D: Voice coil actuator. Stationary magnet and moving coil. Current through the coil causes it to translate [1].

Concept E: Rack and pinion. The rack would need to be preloaded in order to prevent backlash. [2]

Concept F: Low-backlash ballscrew [3].

The six concepts are evaluated in Table 3.1.

3.2 Discussion of the design concepts

Concepts A, B, and C all show cable-drive systems that could be used to reduce backlash in the system. The challenge with a cable-drive system is once again cable wander and device compactness. Device A shows a simple concept for transmitting the rotation of the motor into translational motion of the ultrasound probe (shown in lighter color). The motor protrudes from the side and make the device bulky. Device B mounts the motor at 90 degrees away from Device A and uses two pulleys to route the string. The challenge with Design B is that the string wander that occurs at the motor capstan will tend to elongate the string, as in Fig 2-16, since the pulleys are stationary. This will cause a significant increase in necessary motor torque and is not acceptable. Device C redesigns the pulleys of Device B so that the pulleys essentially have a varying radius, which allows the cable to wander without increasing the cable

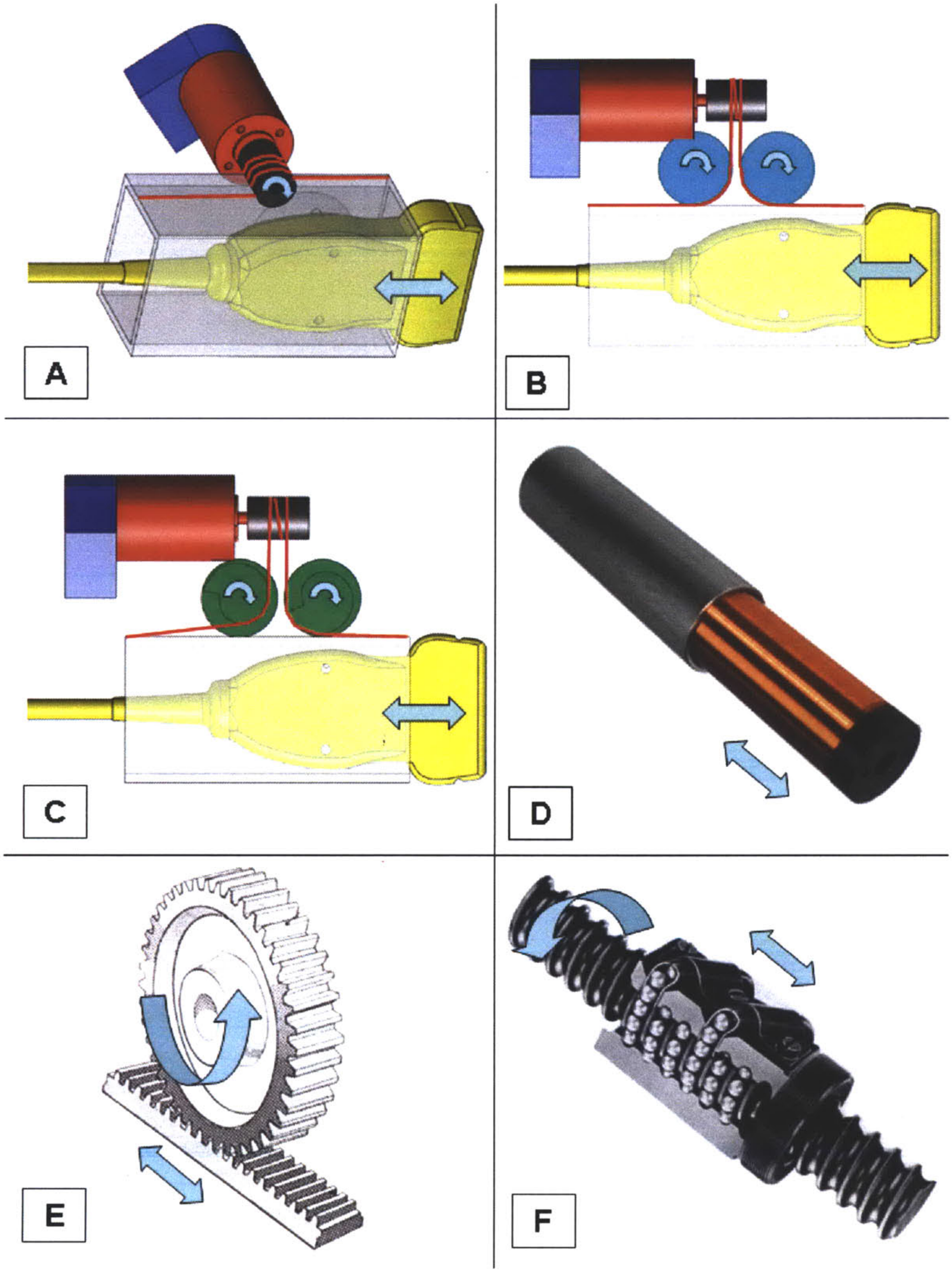

Figure 3-1: Six design concepts for the FCS

Design Parameter	Analysis	References	Risks	Countermeasures
Concept A	Calculate cable tension to attain desired torque	Eqn 2.2	Shape too cumbersome to fit in person's hand	Concept B
Concept B	Cable slip calculation	Eqn 2.2	String wander	Concept C
Concept C	Cable slip calculation, shape of spiral	Eqn 2.2	Torque varies through range of motion	No obvious countermeasure
Concept D	Holding current	F=i*LxB, VCA literature [5]	High power to hold in place	Make actuator weight = desired force
Concept E	Analysis to prevent cog breakage, slip	FEA	Too much backlash	Preload
Concept F	Screw pitch to get desired speed, force	$F=\tau/P$, P=pitch	Not backdriveable	Steepen screw threads

Table 3.1: Evaluation of concepts for the FCS

tension. But since the pulleys have varying radii this leads to varying torque and differential movement between the cylindrical portions of the pulleys, which would cause the cable to break.

Voice coil actuators are appealing because of their simplicity, easy backdriveability, and widespread commercial availability, but the problem is that these devices typically require high power to maintain a desired force. In order to hold 10N of force, for example, a typical voice coil actuator from BEI Kimko requires 90W [5].

The rack and pinion system of Device E suffers from high backlash. Quickly rotating the motor rotor back-and-forth (to counter the hand tremor of the technician) would cause the gear to "see" the backlash, and cause a lower positional accuracy at the ultrasound endpoint. Any additional gear-based reduction would further increase the backlash. One alternative would be to apply a constant linear force to the actuator that is greater than the maximum normal force expected to be exerted with the ultrasound probe. This would cause back-and-forth motions of the motor pinion to maintain gear engagement and keep positional accuracy. But preloading the gear increases the necessary torque of the motor. Another alternative is to use a set of two pinions that are preloaded torsionally (with a torsional spring, for example) with respect to each other, but this option was not explored.

The best device for achieving low-backlash linear motion seems to be a ballscrew actuator. We selected a Precision NSK Monocarrier linear actuator with pitch 2mm, travel 100mm, and a specified backlash of less than 3μm [6].

3.3 Design of the Force-Controlled Stage

An electrically-commutated Maxon EC-Max 30 motor was selected to drive the ballscrew actuator. The 2mm-pitch ballscrew was selected because it permits a maximum normal force of 80N to be applied at the endpoint when the Maxon motor is at stall torque (160mNm), giving a 10X safety factor in maximum normal force from Table 2.1. From the spec sheet, the maximum translational speed of the ballscrew actuator is 100mm/sec (50 rotations per second) because the ball bearings cannot be recirculated any faster. A picture of the FCS is shown in Fig 3-2.

3.4 Use scenario

The technician grasps the 1/16" aluminum plate on the back of the device. A Vermon 7L3V 5 MHz ultrasound probe is mounted to the end of the actuator. A Mini40 six-axis force/torque sensor from ATI Industrial Automation measures the force between the device and the ultrasound probe. The probe is assumed rigid; this force will be essentially the same as the contact force between the ultrasound probe and the patient's body. The force sensor is mounted to an aluminum plate that connects to the carriage of the NSK Monocarrier ballscrew actuator. The Maxon motor rotates the ballscrew, which drives the actuator. The technician grasps the back plate and places the device in contact with the patient. The control system commands the motor to move based on the applied force, in order to achieve the desired contact

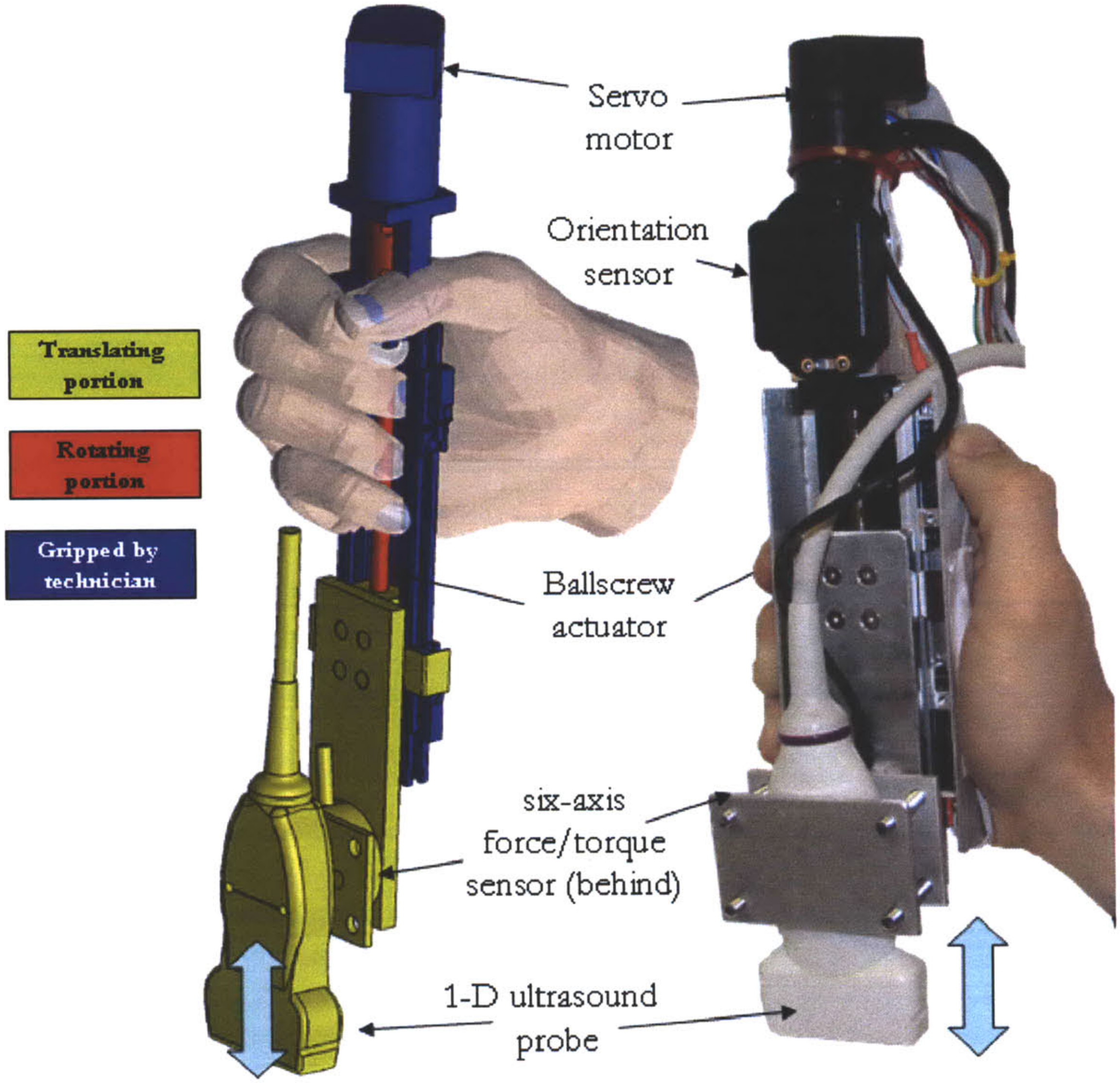

Figure 3-2: The FCS

force.

The system performs gravity compensation to account for the weight of the ultrasound probe. Since the ultrasound probe has mass, as the technician changes orientations the contact force read by the sensor will change, even though the actual contact force might remain constant. In order to correct for the changing weight of the ultrasound transducer, a Motion Node orientation sensor measures the angle between the ballscrew axis and the gravity vector. This angle is used to subtract off the weight of the probe, and this allows a constant contact force to be applied in any

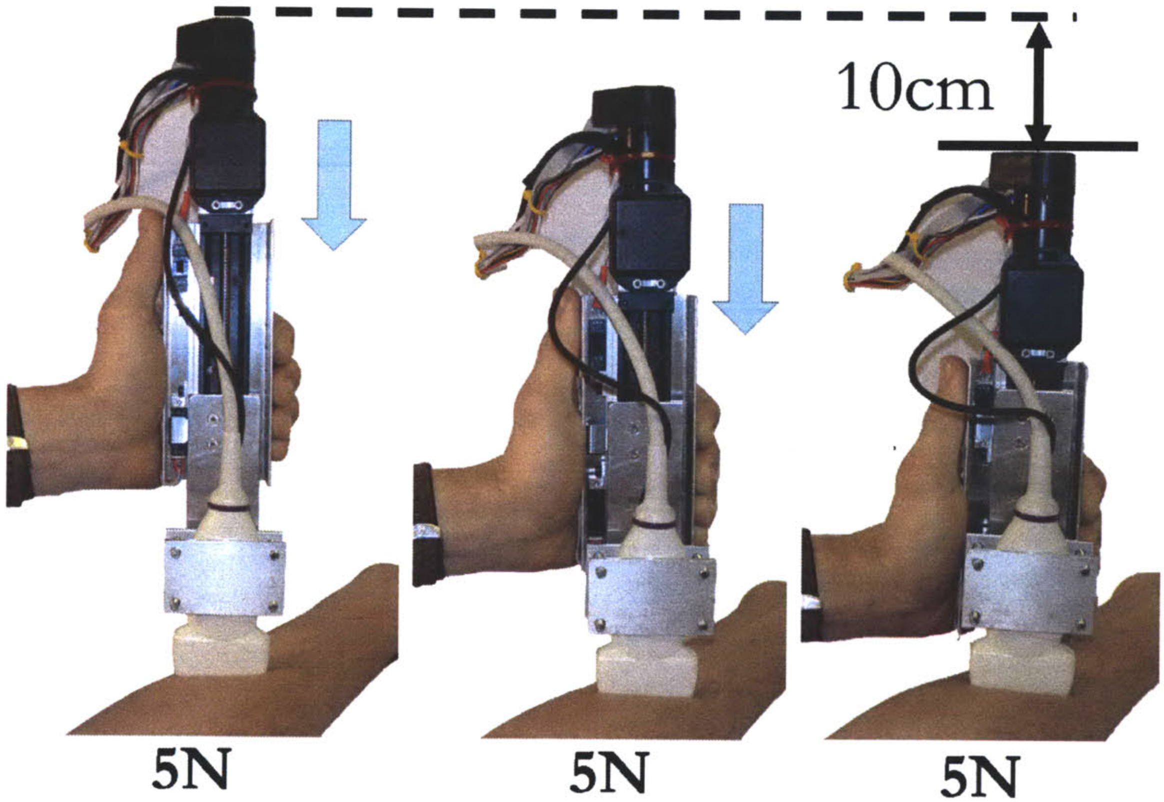

Figure 3-3: Range of motion of the device

orientation.

Since the device is controlling a target force and the actuator position varies in order to attain that force, the travel of the actuator needs to be wide enough to accommodate for position drift in the technician's hand. We selected a ballscrew with 10cm of travel, which makes the device rather large but allows us to explore the range of motion that the technician actually needs. A picture of the range of motion of the actuator is shown in Fig 3-3 .

3.5 Safety features of the FCS

Numerous safety features were incorporated into the FCS to make it safer to use with "humans in the loop." These safety features would be a subset of the necessary features on future prototypes. The features are listed below:

- Master emergency stop button to cut power to the amplifier

- Omron optical limit switches disable the amplifier when the stage reaches a limit
- Position is software-limited to 10mm before the limit switches
- Velocity is software-limited to 40 rotations/sec
- If any force exceeds 15N or torque exceeds 0.7Nm the amplifier is disabled.
- Amplifier is current-limited to 6A peak and 2A continuous.

3.6 Lessons learned from the Force-Controlled Stage

While the Force-Controlled Stage fits in the hand of an adult and can be used to gather images, it would be easier to use if it were much smaller. The total mass of the FCS including the motors is 902g, making it about 50% lighter than the Cylindrical Motion Frame. A machined U-shaped channel allows the user to hold on to the device. The total length is about 36cm. One potential way to reduce the size would be to build a custom housing for the ultrasound transducer electronics, which allows the ultrasound and force transducers to be much more integrated into the device. Using a cable-driven actuator might also make the device smaller.

3.7 Summary

This chapter described the design of a handheld linear-DOF stage to control the force applied by the ultrasound probe. The device uses a ballscrew linear actuator to convert rotational motion of the motor into linear motion of the ultrasound probe. The technician holds the device by its handle, and the contact force is measured by a force sensor. While the device could be held in a person's hand, future work is needed to make the device smaller and lighter, so it will be even more ergonomic to use.

Chapter 4

Force control hardware

This chapter provides an overview of the hardware used to control the device along with a description of each electronic component. The hardware was purchased piece-by-piece and integrated by the author.

4.1 Overview

The goal is to control the contact force between the ultrasound probe and the patient. A high-level diagram of the system we built to accomplish force control is shown in Fig 4-1.

The motion of the system is controlled with a LabVIEW program. The program sends out commands to a PXI chassis, which contains a motion controller card and DAQ card. The motion card generates a trajectory, and the voltage is sent to a Copley amplifier. The amplified signal is sent to the Maxon motor on the device. The force and other safety parameters (see Section 3.5) are read and sent back to the LabVIEW program. Based on the force and other safety parameters the LabVIEW program calculates the next move in order to attain a constant contact force. The LabVIEW program is described more in Section 5.

A picture of the hardware setup we created for controlling the device is shown in Fig 4-2.

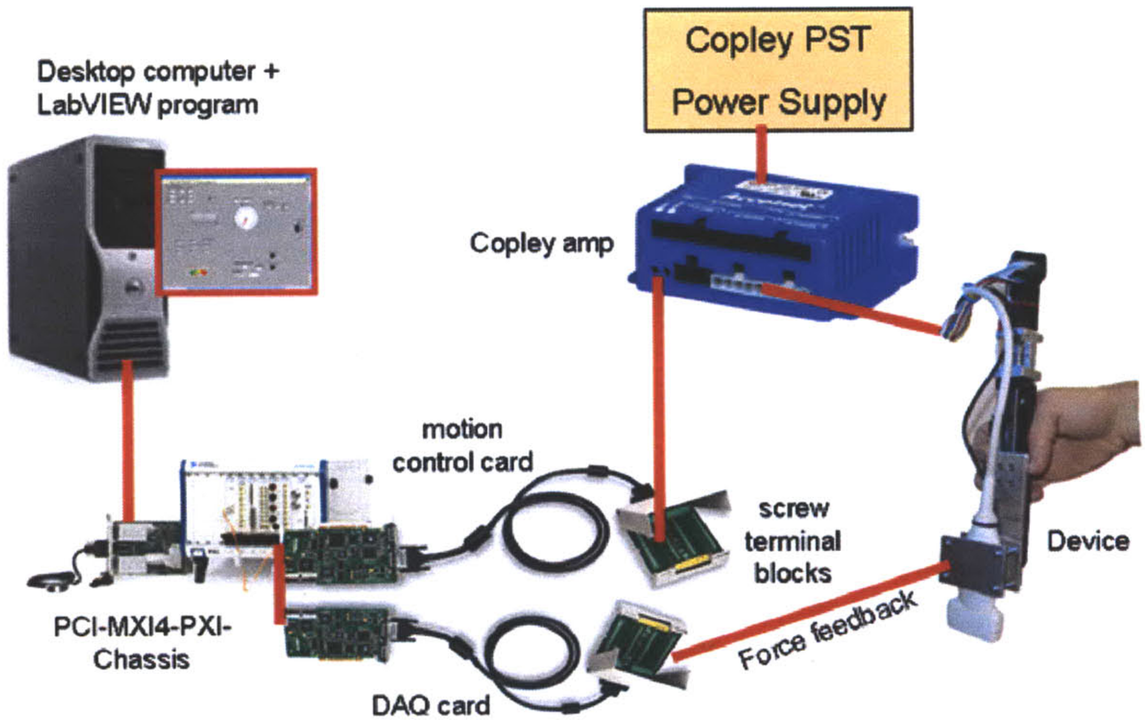

Figure 4-1: Hardware used to control the device

4.2 Description of the components

The setup consists of components from National Instruments, Copley Controls, ATI Industrial Automation, Maxon Motors, NSK Monocarrier, and MotionNode. Figs 4-3 to 4-5 show the components, along with a description and the manufacturer.

4.3 Summary

This chapter provided an overview along with a detailed description of the hardware used to control the force applied by the device. The most significant portion of the control is performed with National Instruments components, which communicate with a Copley Controls amplifier. The next chapter describes how these electronic components interact with the LabVIEW program to control the applied force.

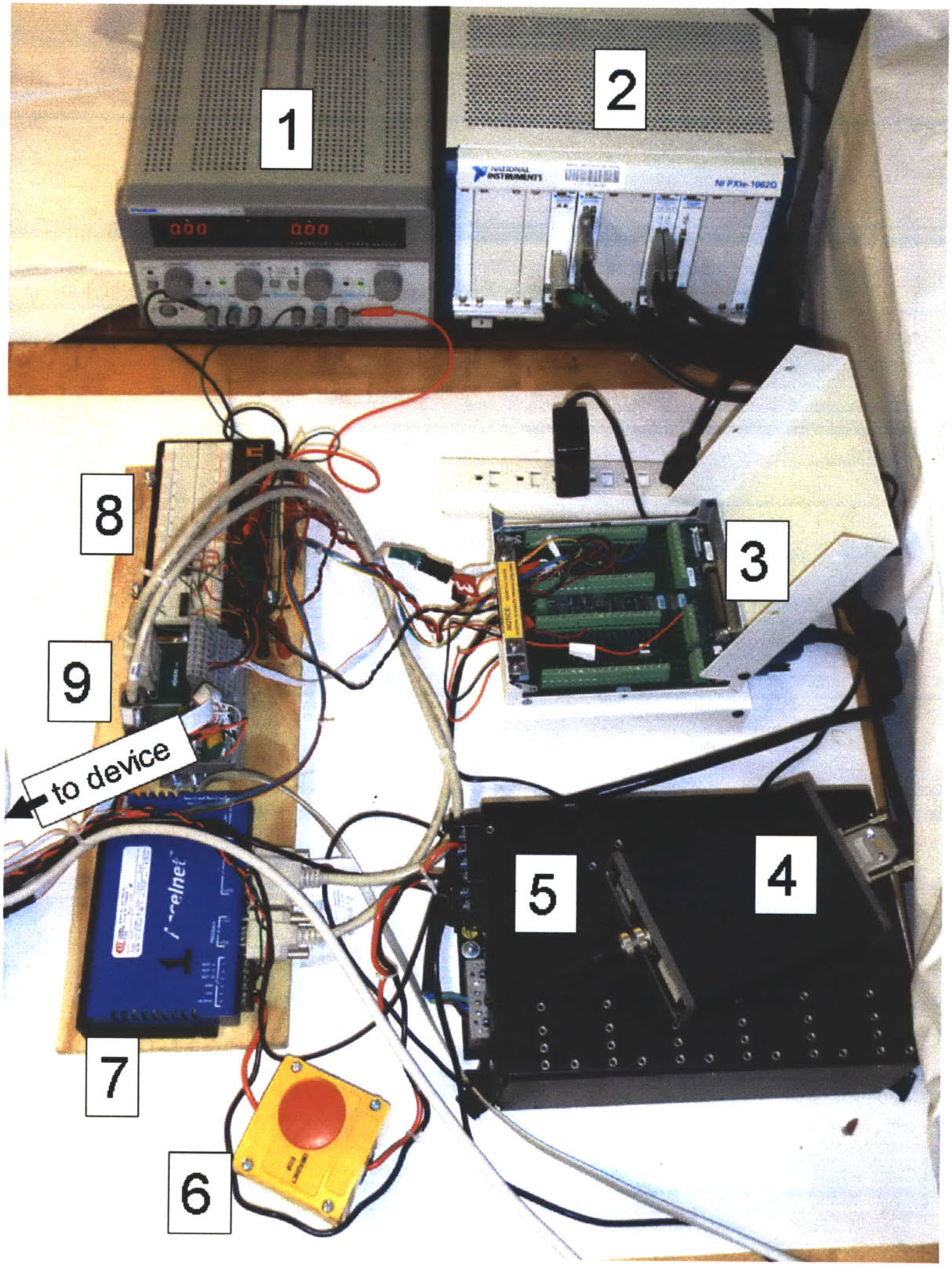

Figure 4-2: Components involved in controlling the device

	1. Protek 3205L Lab power supply	Supplies +10V to the analog circuit
	2. NI PXIe-1062Q Chassis	10 slot PXI chassis houses the DAQ and motion cards (below), provides room for expansion
	2a. NI PXI-6363 X-Series DAQ Card	Reads in the force sensor voltages and outputs analog voltage proportional to applied force
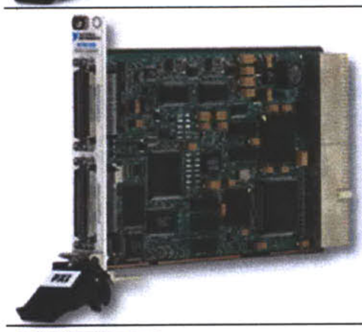	2b. NI PXI-7358 8-axis motion controller card	Sends out motion commands to the Copley Amplifier, reads limit switches
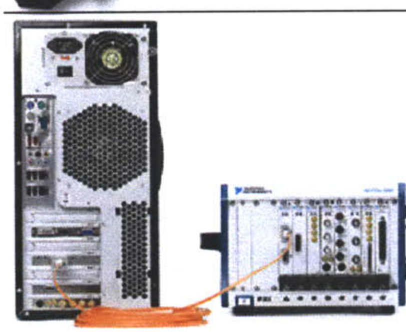	2c. NI MXI-4 link	Provides high-speed link between computer and PXI chassis

Figure 4-3: Components involved in controlling the device

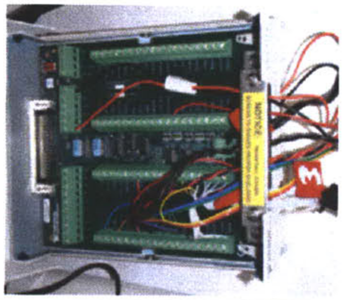	3. NI UMI-7774 screw terminal connector block	Provides easy connectivity between motion card and amplifier, limit switches, etc.
	4. ATI FTIFPS1 DAQ F/T Signal converter box	Conditions force sensor voltages, supplies power. Calibration is programmed into this box.
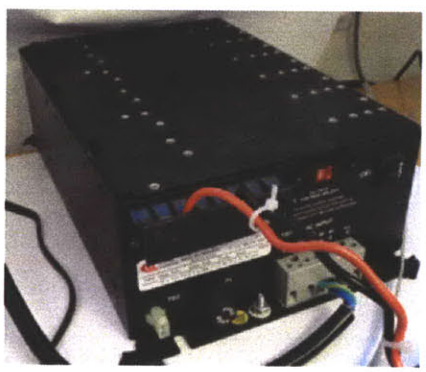	5. Copley Controls PST-040-13-DP 40V power supply	Supplies 40V to the Copley Amplifier
	6. Baco latching emergency stop switch	Kills power to the Copley Amplifier
	7. Copley Controls Accelnet ADP-090-09 amplifier	Amplifies motion signal to motor, passes through encoder signals.

Figure 4-4: Components involved in controlling the device

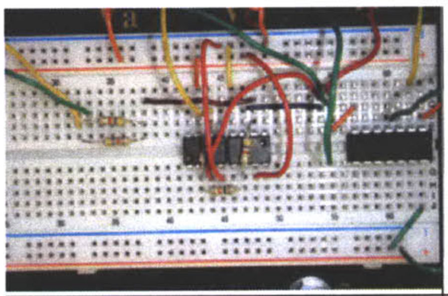	8. Custom-built analog circuit with OR gate	Sums the signals from the two axis. Digital OR gate enables the amplifier
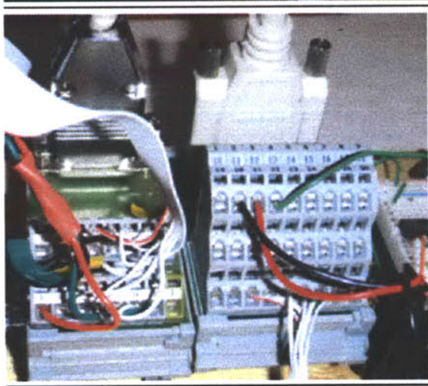	9. Wago easy-connect block	Provides easy connection to Copley amplifier from motion card and motor + encoder

Figure 4-5: Components involved in controlling the device

Chapter 5

Force control with LabVIEW

A custom LabVIEW program controls the force applied by the device. This chapter describes the operation of the LabVIEW program. The LabVIEW program calculates the actual contact force based on the raw force readings and orientation of the device. It then sends out an analog voltage proportional to that contact force. The analog voltage is fed into the built-in controller on one of the axes, which subtracts the actual force from the desired contact force and resulting force error is sent through a PID controller. The output signal from the PID controller sent to the amplifier, which provides power to the motor.

We found that the greatest bottleneck in the execution of the program is the calculation of the contact force, which occurs at 250Hz. This step must be performed closer to 1000Hz to ensure smooth control. The performance of the system could be improved in the future with either a dedicated, deterministic processor, or with an analog system that rapidly outputs a voltage that is proportional to the applied force.

5.1 Control System Overview

A block diagram of the basic force control strategy used in the LabVIEW program is shown in Fig 5-1.

The desired force is input into the LabVIEW program by the user. A PID controller on the motion card compares the desired force with the actual force and gen-

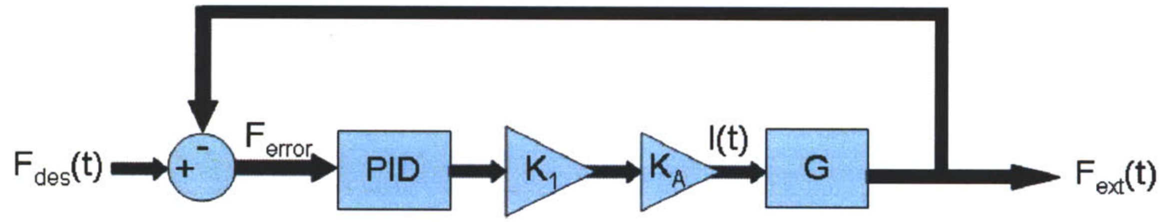

Figure 5-1: Simple force control system

erates a command signal, which is scaled by a factor K_1 in the program (see Section 5.4), and then amplified by the amplifier gain K_A. The resulting current is sent to the motor G, which applies a force with the environment.

5.2 The LabVIEW virtual instrument

A program (also called a "Virtual Instrument") was created using the LabVIEW visual programming system. A screenshot of the program showing the significant steps is pictured in Fig 5-2.

The steps involved in the process are listed below:

1. Setup the axis for "absolute position control" (but since the feedback is actually an analog voltage proportional to the force, this becomes force control.)

2. Run Loop #2: Read the angle of the device with respect to gravity from the orientation sensor. The orientation sensor is used to compensate for gravity and is described in Section 5.3.4.

3. Run Loop #1: Read the raw force voltages output by the force sensor, perform a calculation (see Section 5.3.2), then subtract off the weight of gravity to find the actual probe contact force. Also in Loop #1:Monitor the safety parameters (see Section 3.5), if any safety limit is reached, abort the program

The program performs Step 1 once, then continuously and simultaneously executes Steps 2 & 3 as fast as possible.

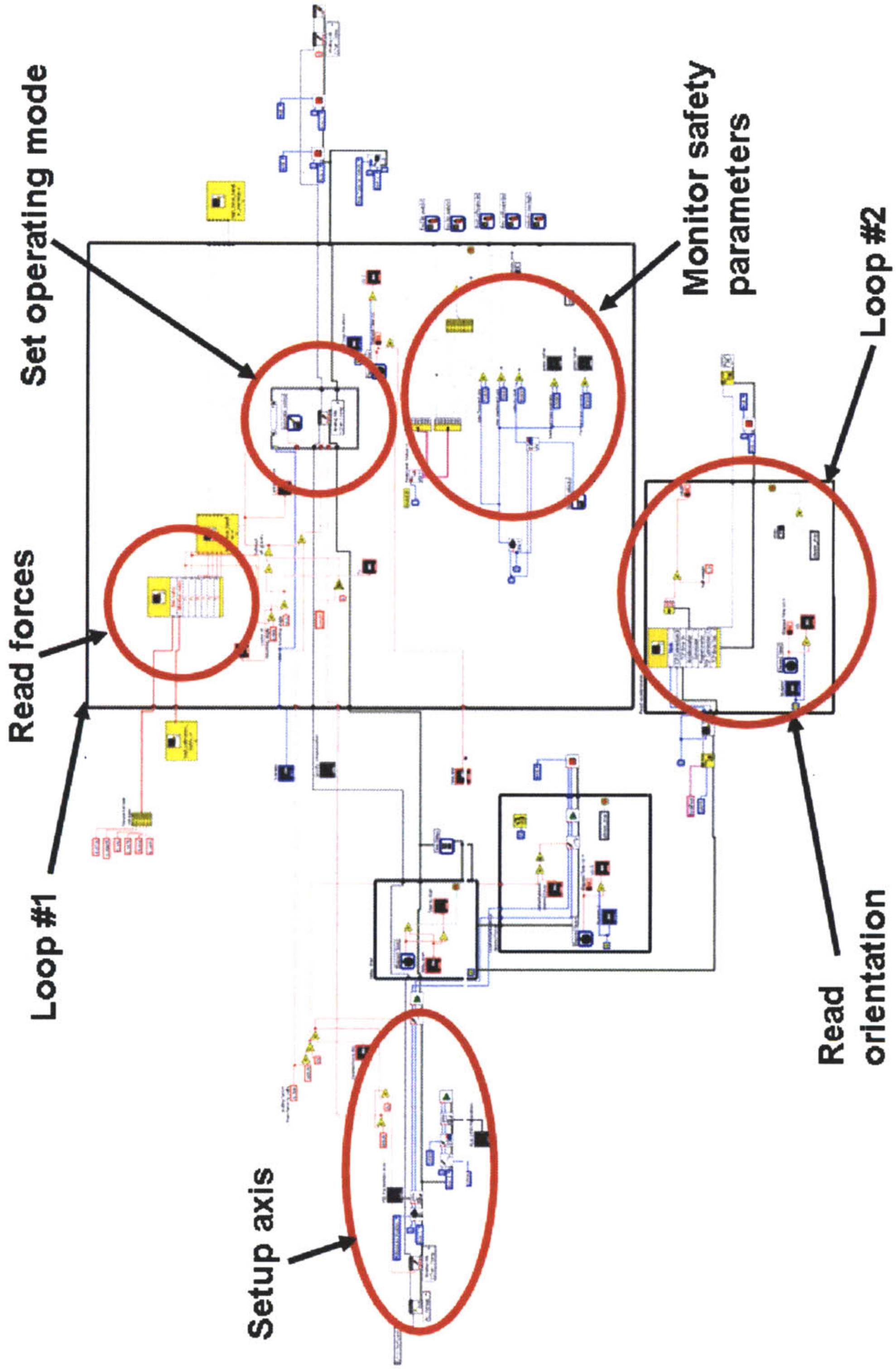

Figure 5-2: Screenshot of the LabVIEW virtual instrument used to control the contact force

5.3 Calculating the Contact force

The parameter that the LabVIEW program seeks to control is the contact force. Determining the actual complex force is complex for three reasons: 1) a non-linear calculation needs to be performed on the raw force sensor voltages to calculate the raw contact forces 2) the force sensor is mounted at a non-orthogonal angle on the device and 3) the measured contact force changes when the orientation of the device changes. This section describes the process of calculating the actual contact force.

5.3.1 Reading the raw force/torque sensor voltages

The program starts by reading the output from the Mini40 six axis force/torque sensor from ATI Industrial Automation, a picture of which is shown in Fig 5-3.

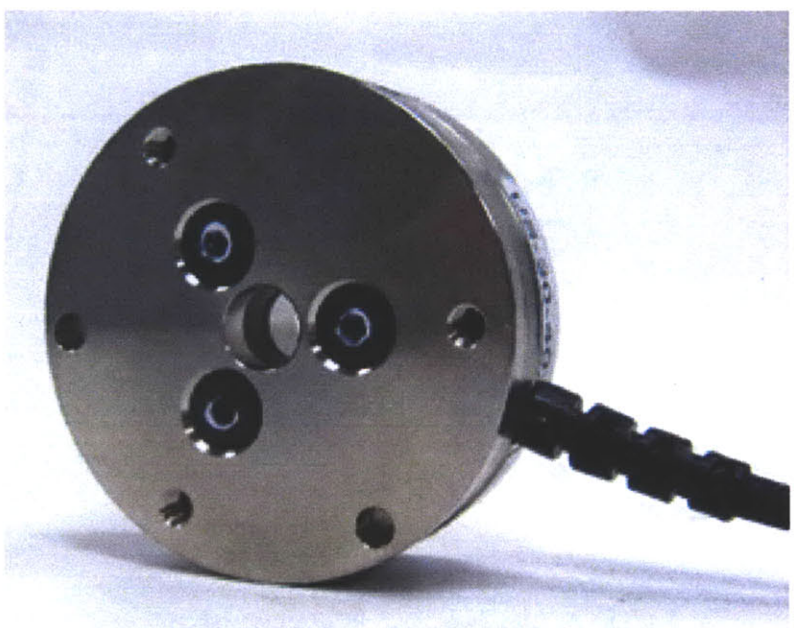

Figure 5-3: Mini40 six-axis force/torque sensor. Diameter = 40mm.

We used a Mini40 force/torque sensor with SI-40-2 calibration, which is one of the six calibrations available from ATI. Each calibration gives the sensor a different sensitivity and range. We chose SI-40-2 calibration because it gives the sensor a resolution of 0.01N in X and Y axes and 0.02N in the Z axis, and a sensing range of

± 40N (X and Y) and ± 120N (in Z). The maximum single-axis overload is ± 810N (X and Y) and ± 2300N (in Z). Without smoothing on the force sensor output we were only able to attain a 0.1N resolution in X and Y.

5.3.2 Converting analog voltages into forces and torques

The ATI Mini40 force sensor outputs six raw voltages V_F that are not proportional to force, and must thus be decoded using the LabVIEW program. These voltages read by the National Instruments PXI-6363 16-bit Data Acquisition (DAQ) card. Each A/D has a range of ± 10 volts, so each A/D converter converts the voltage to counts by the factor $K_{A/D} = 2^{16}cts/20v = 3277$cts/volt. Thus, the LabVIEW program decodes the number of counts read by the device into voltages by the inverse of $K_{A/D}$, which we call $K_{D/A}$.

The force voltages-to-Newtons calculation is performed as specified in the ATI Mini40 user manual. First, with the device horizontal and not in contact with the environment, the six voltages output by the force sensor are measured (using ATI's software provided with the device). This reading is called the bias voltage reading V_{bias}. To calculate the actual applied forces and torques $F_{applied}$, the bias voltage matrix is subtracted from the actual voltages $V_{reading}$ and the result is premultiplied by the ATI-provided calibration matrix C. The result is the three applied forces and three applied torques. The calculation is shown below in Eqn 5.1.

$$F_{applied} = \begin{pmatrix} F_x & F_y & F_z & \tau_x & \tau_y & \tau_z \end{pmatrix}^T = C_{6x6}(V_{reading} - V_{bias})_{6x1} \tag{5.1}$$

As the LabVIEW program runs, it performs this calculation with each loop cycle. The torques are monitored for safety but not controlled.

5.3.3 Compensating for the mounting angle

The next step in calculating the applied force is to compensate for the mounting angle of the force/torque sensor. Since the X-axis of the force sensor is mounted at a $+30°$ angle with respect to the linear axis of the device, it is necessary to take the vector sum of the measured forces $F_x{}^*$ and $F_y{}^*$ in order to calculate the linear applied force F_L. Fig 5-4 shows the coordinate frames of the ultrasound, force/torque sensor, and device.

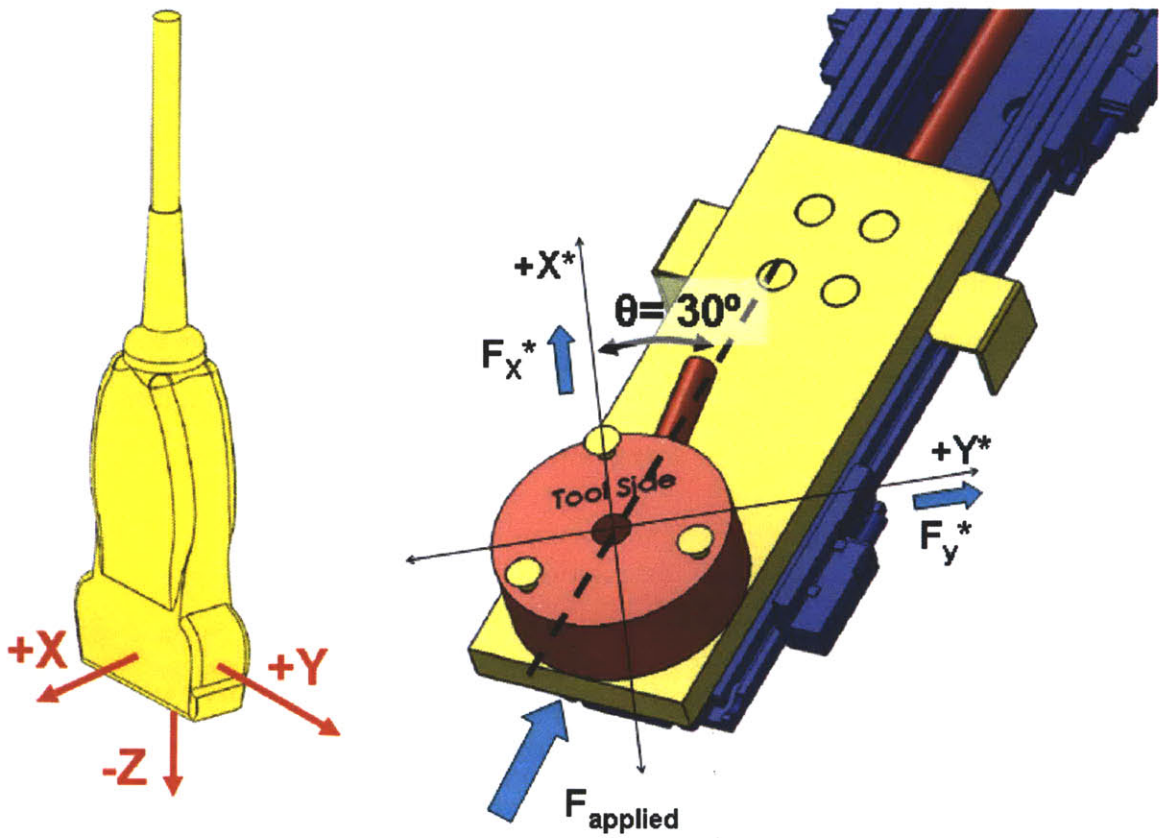

Figure 5-4: Coordinate frame of ultrasound probe (left) and coordinate frame of force/torque sensor. The sensor is mounted with its +X* axis at a 30° angle from the ultrasound transducer's -Z axis, so the $F_x{}^*$ and $F_y{}^*$ components must both be used to calculate $F_{applied}$.

The equation relating the linear applied force to the measured forces is

$$F_L = -\frac{1}{2}F_y^* + \frac{\sqrt{3}}{2}F_x^* \tag{5.2}$$

5.3.4 Gravity Compensation

The final step that must be performed to determine the contact force is to subtract off the weight of the ultrasound probe. Since the ultrasound probe has mass, when the technician varies the angle of the device, as would be common during a real ultrasound exam, the force sensor will measure the weight of the probe along with the contact force. In order to subtract out the weight of the ultrasound probe we use a 3-axis accelerometer from MotionNode [4]. Using this sensor we can calculate the component of the ultrasound probe weight vector in the direction of F_L and subtract this out from F_L in order to get the actual contact force $F_{contact}$.

5.4 Using the Calculated Contact Force

The next step in the LabVIEW program is to compare the actual contact force with the desired contact force. In constant-force mode, before the program is run the user enters into LabVIEW the desired contact force. This is multiplied by $K_{A/D}$ and the constant K_1 to get the desired force in counts. K_1 is a user-defined constant which determines the scaling from Newtons to Volts. It was found that a value of 1N/0.008V for K_1 gave the system the best performance. Any higher and the device would frequently reach a velocity limit, any lower and the response of the device would be more sluggish.

This desired force value in counts is then sent to the NI PXI-7358 Motion Controller card for Axis 1. In order to feed the force back to Axis 1 we use the analog output of the PXI-6363 DAQ card. The actual force F_{actual} in Newtons is multiplied by K_1 and $K_{A/D}$ and the resulting value in counts is sent out of the DAQ card through an analog output port. The resulting voltage is then fed into the feedback channel for Axis 1. The built-in 4kHz PID controller (whose gains are programmed in advance, see Section 5.7) on the PXI-7358 controller card looks at the desired force (in counts) and compares it with the actual force (in counts). Based on the gains it then calculates the $\pm$10V analog control signal and sends this voltage to the Copley Accelnet amplifier.

5.5 Amplier Operation

The amplifier takes the input voltage and applies a constant current proportional to the voltage by the factor K_A, which we set to equal 0.1A/V. A control loop built-in to the amplifier is used to increase the consistency of the current signal. We found experimentally that the amplifier's control loop has negligible dynamics, and the amplifier can be treated as a simple gain from volts to amps.

Motor commutation is handled by the Copley amplifier. Since the motor is electrically commutated, the outputs from the three Hall sensors are fed back to the amplifier. The voltage command is sent from the National Instruments PXI-7358 Motion Controller card to the Copley Amplifier. A block diagram depicting the control system Fig 5-5.

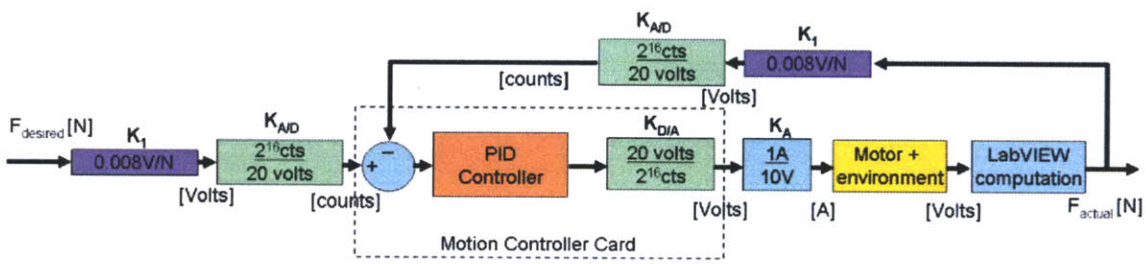

Figure 5-5: Flow of information in the system.

5.6 Control System Performance

We found that the force could be read at a maximum rate of 254Hz, while the orientation could be read at 60Hz.

The rate of 254Hz for reading the force is about $\frac{1}{4}^{th}$ of the speed we would prefer for smooth control. The bottleneck of the code is in reading the six force voltages and setting the DAQ voltage to be proportional to force. But this step cannot be eliminated because the six voltages output by the force sensor are meaningless until they are multiplied by the calibration matrix and output through the DAQ card. One alternative would be to purchase a \$1700 analog device from ATI that takes the six raw voltages and (essentially instantaneously) converts these to six analog voltages proportional to the forces and torques.

Another limitation of this setup is that it is very difficult to measure the frequency response of the closed loop system. Ideally, in order to generate a Bode plot we would like to vary the desired force F_{des} at a certain frequency, then record the magnitude and phase of the output force. We would like to vary F_{des} at a range of frequencies including 1kHz. But since the force setpoint can only changed at 100Hz, if we wanted to change F_{des} sinusoidally and smoothly with 10 points per period, we could attain a maximum speed of only about 10Hz. In Section 8.1 we use the step response in place of frequency response to investigate the dynamics of the control system.

5.7 PID Controller

At the core of the control loop is a PID controller that is built into the PXI-7358 motion controller card. The gains of the controller are specified within the LabVIEW program. The maximum update rate is 4000Hz and the transfer function is given from the spec sheet as

$$G_1 = K_p + \frac{K_i}{s} + K_d s \tag{5.3}$$

5.8 Summary

Fig 5-6 summarizes the flow of information in the system, as discussed in this Chapter.

This chapter described the operation of the LabVIEW program to provide a constant contact force. The most complex and time-consuming portion of the control loop is to calculate the actual contact force based on the raw force sensor voltages, the orientation of the device, and the mounting angle of the force sensor on the device. The built-in PID controller on the motion card then compares the desired contact force with the actual (calculated) contact force and the resulting signal is sent to the Copley amplifier. The Copley amplifier finally sends power to actuate the motor.

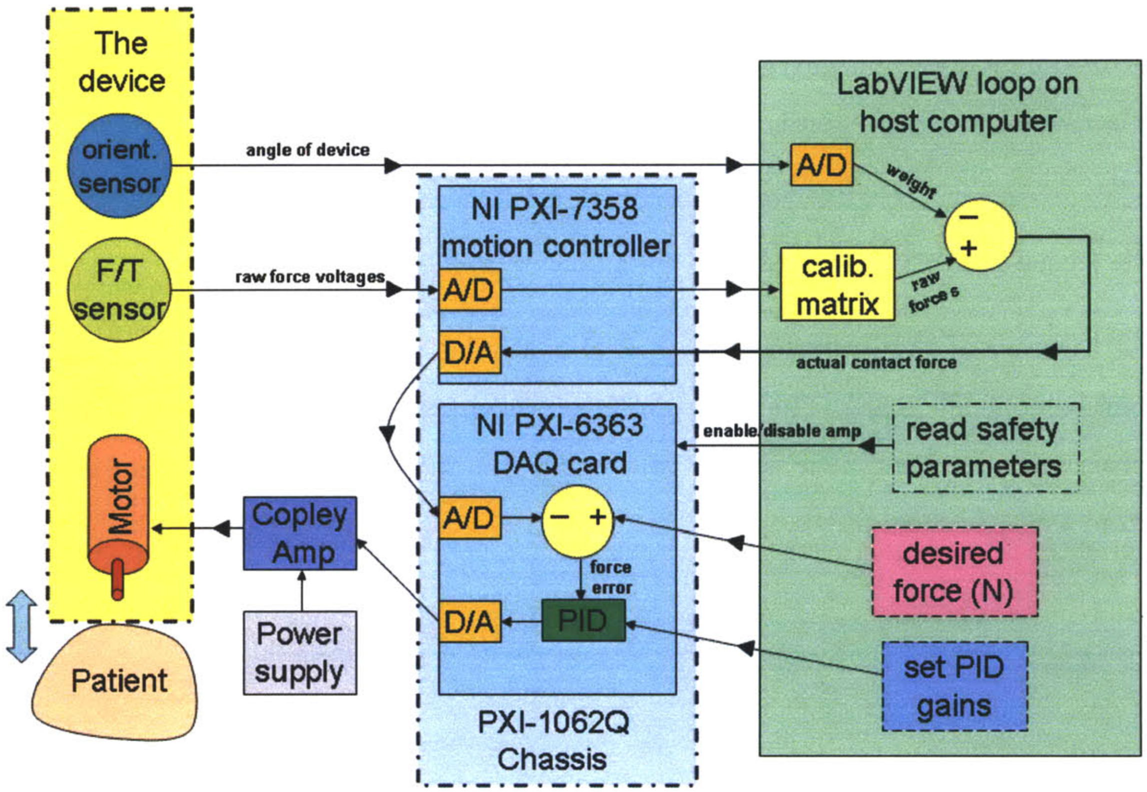

Figure 5-6: Flow of information in the system

Chapter 6

Improving usability with high-level logic

The previous Chapter discussed the operation of the LabVIEW program to provide a constant contact force. Next we investigate improvements to the control strategy that make the device easier to use. The improvements take the form of modifications to the LabVIEW program and some additional custom circuitry.

6.1 Beyond pure force control

Force control is useful for maintaining a constant contact force when the device is in contact with the patient. A problem arises when the technician lifts the device and breaks contact with the patient. With the traditional control strategy, the device will always try to maintain 5N of contact force, for example. When contact is broken the device will experience a very high control effort at the as controller tries to actuate the motor to attain 5N. The motor will rotate very quickly and rocket the stage in one direction until the device reaches a limit or exceeds the maximum allowable velocity. This is problematic because it means that the device will need to be reset, wasting time and creating frustration of the user. A more user-friendly strategy is thus needed to ensure that the actuator can safely "make and break" contact.

A number of control strategies are possible to prevent unwanted actuator movement when the actuator is out of contact with the patient's body. One is to place a limit on the maximum allowable derivative of force. This way, abrupt changes in contact force like those that would be experienced while making and breaking contact would cause the control signal to be capped to limit the actuator to a safe and reasonable speed.

6.1.1 Impedance Control

Another possible strategy would be to control a combination of two parameters simultaneously: force & position or force & velocity. In order to provide a control signal based on two system parameters, two of the controller card's built-in PID loops must be used because control in LabVIEW is relatively slow (250Hz). The control efforts from both of these commands must be added together because it is not possible to control two parameters on a single-DOF system simultaneously.

One strategy for controlling a combination of force and velocity simultaneously is to use Impedance Control [18]. A block diagram for impedance control is shown in Fig 6-1.

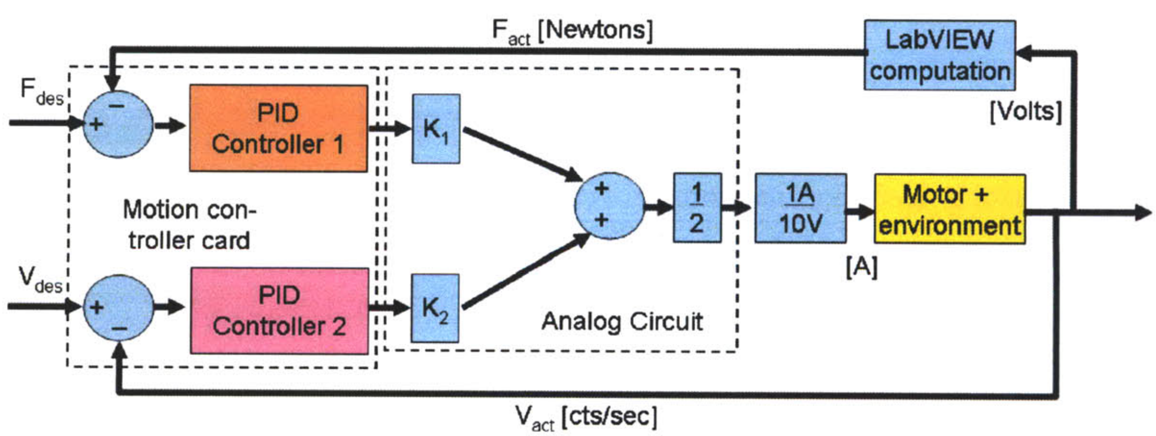

Figure 6-1: Impedance control

In impedance control, a desired force and desired velocity are programmed into the system. Since the motor can only accept one input the control signals from the force and the velocity loops must be added.

The problem with this strategy of simultaneously controlling a combination of two system parameters is that when the actuator is not in contact with the patient it will tend to drift to one side or the other because it is difficult to make the force reading exactly zero. We found that as the actuator drifts to compensate for the non-zero contact force, it will eventually reach a limit. One possible solution might be to instead control position & force instead of velocity & force. That way, the device would have a preferred position in the middle of the actuator (for example) and would be less likely to drift out of range while not in contact with the patient.

Such a simultaneous position & force control strategy would give the actuator a preferred force and a preferred position, although it would be unlikely that both would ever be simultaneously satisfied. The challenge is that we want to retain the ability to maintain a constant force when the device is in contact with the patient. Thus, there needs to a method of switching between a pure force control and a hybrid force + position control scheme depending on whether the device is in contact or not.

Intuitively, we would expect a hybrid force + position control scheme to act like two opposing springs with different equilibrium positions. The force control loop would have a virtual spring trying to move the actuator to attain 5N contact force, for example. At the same time, the position control loop would behave similar to a real spring and try to move the actuator to its equilibrium position. As a result of these two forces the actuator would settle at a certain position and force that balances the control efforts exerted by the two control loops. The general control scheme would look the same as in Fig 6-1, with a target position instead of a target velocity. The preference to either a target position or target force would depend on the relative magnitudes of K_1 and K_2.

6.1.2 Control using high-level logic

But impedance control is unnecessarily complex. Because the user will only ever be in one of two use scenarios: either in contact or not in contact, it is far simpler to have a high-level supervisory control system that switches between either pure force control or pure position control (but never both simultaneously). We created a system that maintains a constant contact force when the device is in contact with the patient, and when the device is removed from contact the actuator travels to a 'home' position.

The user starts out by placing the device in contact with the patient. The device maintains a constant force. If the user decides to break contact, as soon as he/she removes the device from contact the large control signal resulting from the large force error will likely cause either a velocity limit to be reached to a limit switch to be triggered. This generates a fault. The supervisory control system monitors whether or not a fault has been generated. If a fault is generated the system immediately disables the force control axis and enables the position control axis, which returns the actuator to the a home position in the middle of its range of travel. When the home position is reached it then disables the position control axis and reenables the force control axis.

As with impedance control, since the amplifier can only accept one command the $\pm$10V commands from the two axes must be added. The signals are added with an analog circuit (See Section 6.3), and the result is divided by 2 to keep it within the $\pm$10V range. The resulting voltage is sent to the amplifier and then the motor.

6.2 Use Scenario

In the control system we designed the user can go from In-Contact to Not-in-Contact by simply letting the actuator reach a limit of travel, or by pulling up on the actuator rapidly. If the device is pulled upwards rapidly enough (set at 7.5cm/sec due to the maximum ball bearing recirculation rate), the controller will assume the technician wants to break contact with the patient. It will pause for 1 second and then automatically enter position control mode, and move the actuator to the home positon. It will move the actuator to its center of travel, and then wait for the user to match the desired force (See Section 6.4.1), at which point it will enter back into force control mode.

The safety limits mentioned in Section 3.5 are monitored at all times. If any force or torque exceeds the maximum programmed value the actuator halts and an error message appears on the computer screen. The user must acknowledge the error by clicking OK before the actuator will resume motion.

With this strategy, only one of the two control loops will be on at a given time. The force loop will never be 'fighting' the position loop.

At all times the user must avoid placing the device in contact with a rigid environment. We found that when the device was held in the hand and placed in contact with a stiff surface such a table top the device began to chatter and the velocity limit was quickly reached, forcing the actuator into position control mode.

6.3 Signal Summing Circuitry

In order to add the two analog signals together rapidly we use a summing op amp followed by an inverting op amp. A diagram of the circuitry along with a picture of the actual circuit are shown in Figs 6-2 and 6-3.

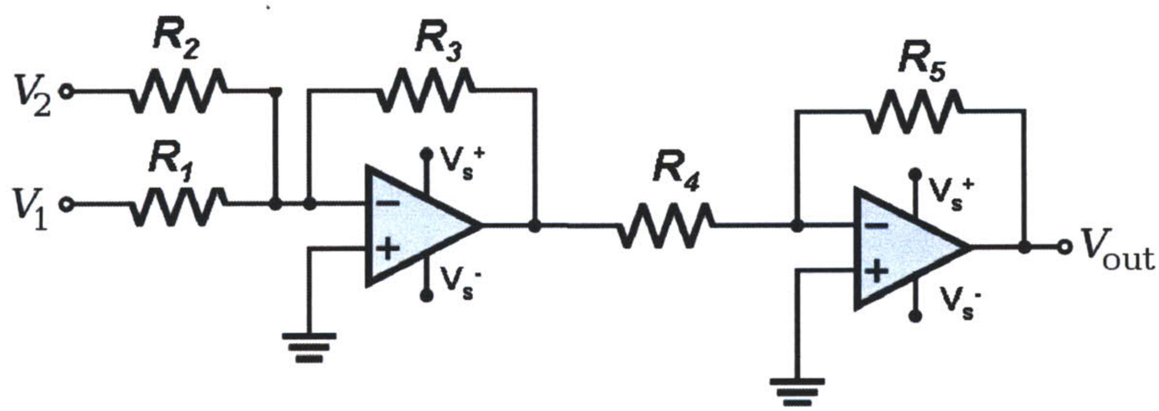

Figure 6-2: Summing + inverting circuit diagram

Since the motion controller update rate is 4kHz the op amp circuit must respond faster than 4kHz in order for its dynamics to be negligible. We investigated the frequency response of the circuit using a function generator and oscilloscope. The setup is shown in Fig 6-4. The Bode plots are shown in Fig 6-5.

From the magnitude plot, the cutoff frequency of this op amp circuit looks to be around 70kHz, which is much faster than the 4kHz update rate for the built-in PID loop. We also see that the response has at least a $+140°$ phase margin at the cutoff

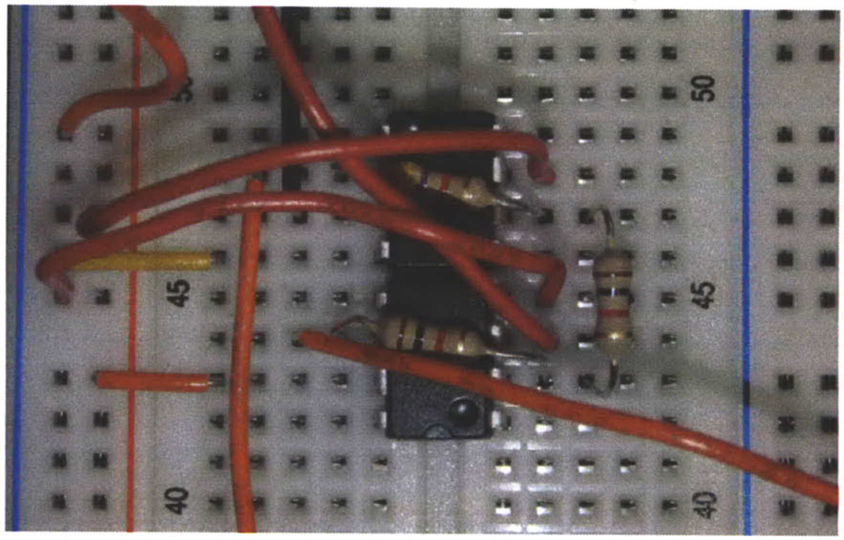

Figure 6-3: Picture of circuit. Op amp used was the LM741 from National Semiconductor.

frequency, which means it should be stable. Thus, we expect the dynamics of the op amp circuit to be negligible in this application.

By changing the values of the resistors R_1 and R_2 we can change the relative gains of the force and position loops K_1 and K_2 (from Fig 6-1), To avoid confusion when rewiring the circuit we chose to use the same resistor values R_1 and R_2 so that K_1 and K_2 were equal. The equation relating the output voltage signal to the input signals based on the resistor values is

$$V_{out} = \frac{R_5 R_3}{R_4}\left(\frac{V_1}{R_1} + \frac{V_2}{R_2}\right) \tag{6.1}$$

In this circuit we use $R_4 = 10\text{k}\Omega$, $R_5 = 5\text{k}\Omega$ so that the inverting op amp inverts the signal and reduces it by one-half, so that the output stays between +10V and -10V even if both of the axes are ever accidentally enabled at the same time. We use $R_3 = 10\text{k}\Omega$, $R_2 = 10\text{k}\Omega$, and $R_1 = 10\ \text{k}\Omega$, where R_1 and R_2 are the resistors of the force and position loops, respectively.

The PID gains of the force and position loop are set in software and are shown in Table 6.1.

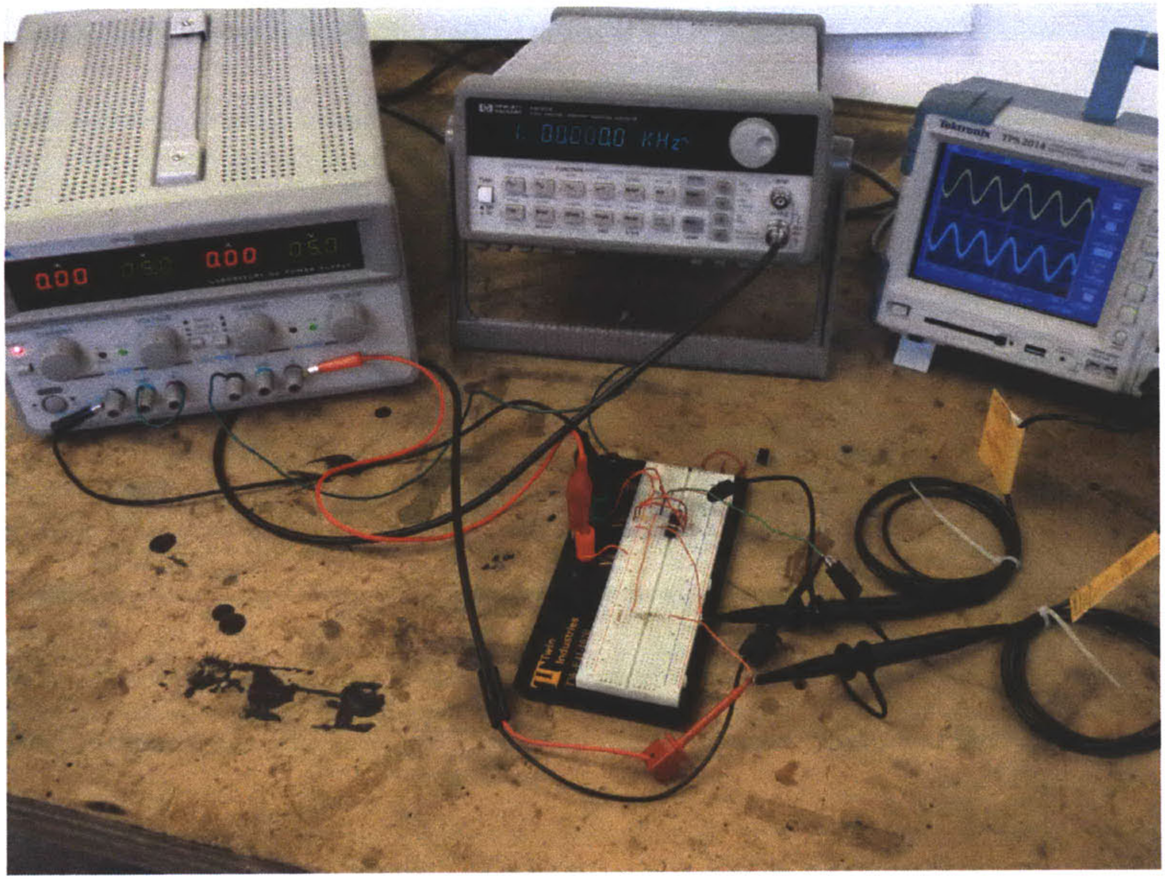

Figure 6-4: The hardware setup used to measure the frequency response of the op amp circuit.

6.4 Further improvements to the device usability

Several additional improvements to the control system were made in order to make the device easier and more natural to use.

6.4.1 Improving usability with a 'soft start'

We found that it was difficult for the user to begin using the device. As soon as the program runs, it tries to attain the target contact force. If the operator is not holding the device in contact near the target force, or not even holding the device in contact at all, the control signal will start out high and in several experiments the actuator often reached its maximum speed and was forced to stop. This showed that it is difficult for an untrained person to know exactly what a contact force of, for example,

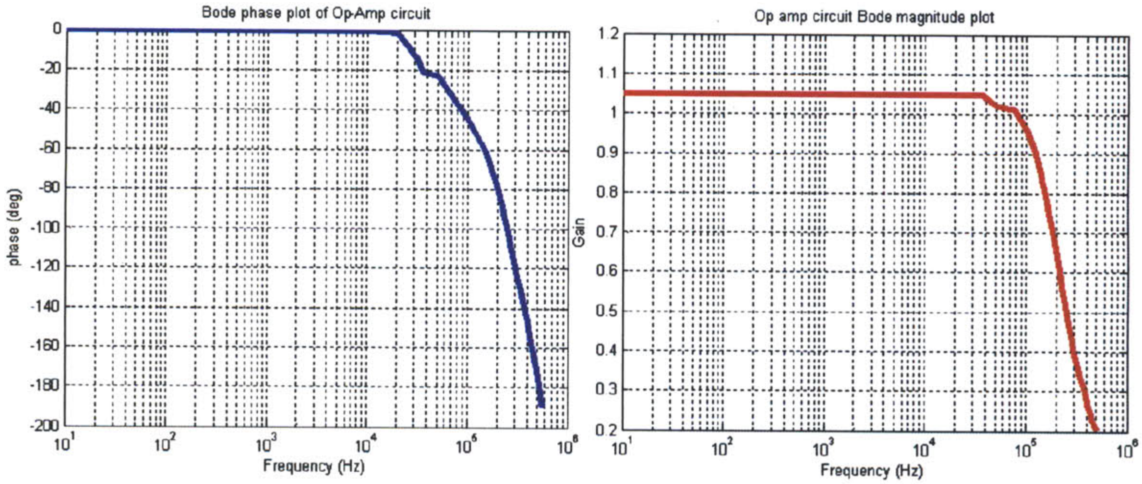

Figure 6-5: Bode magnitude (left) and phase plots (right) of summing + inverting circuit

	K_p	K_i	K_d
Force Loop	1000	10	100
Position Loop	1000	10	0

Table 6.1: The software-set gains for the force control and position control loops

5N feels like before they start using the device.

We thus found the need to implement a 'soft start' so it would be easier for the user to start using the device. We added to the LabVIEW program some logic that as soon as the program starts running, the actuator waits until the desired force is exceeded before the controller turns on. This allows the user to start the program running while the device is not in contact, then place the device against the phantom and manually increase the contact force, until the desired force is attained, at which point the actuator smoothly assumes control of the force. This 'soft start' greatly improved the usability of the device by making it easier for the operator to begin using it.

6.4.2 User control panel

The controls on the front panel of the LabVIEW program enable users without programming experience to control and monitor the device. A screenshot of the Lab-

VIEW program's front panel is shown in Fig 6-6.

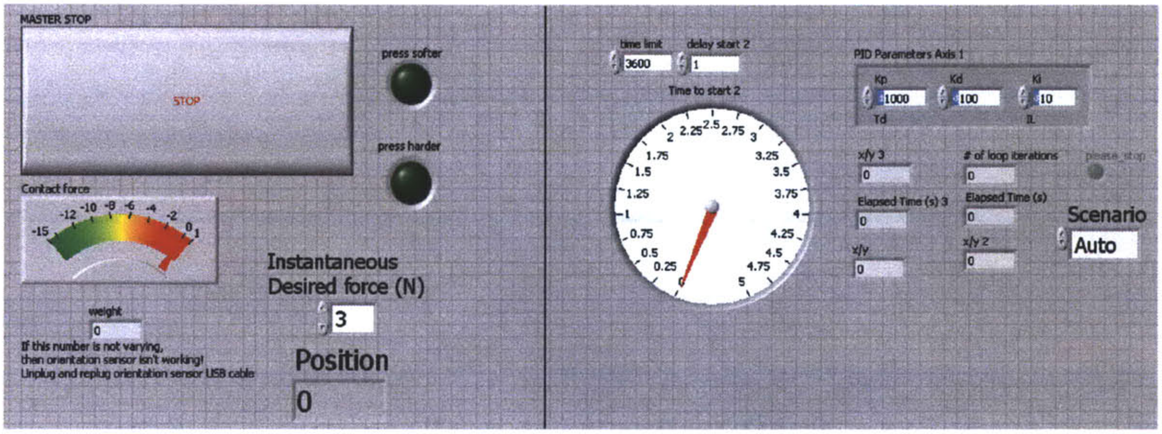

Figure 6-6: Screenshot of the front panel. This is the interface that the user interacts with to control and monitor the device.

The interface is split into two sections. On the left side of the front panel are the basic controls and on the right side are the more advanced controls. Starting with the left side, the user can type the desired contact force into the text box. Then the user presses the RUN button (not shown) and the device starts controlling the force after a programmable time delay. The user can change the desired contact force 'on the fly' while monitoring the position with the numeric readout and the contact force with the force gauge. Two green lights alert the user if the actuator is getting close to its travel limits.

The right side of the front panel enables the user to change the length of the delayed start and the time the program runs for. The user can change the P, I, and D gains of the force PID loop. The user can also monitor the control loop rate, which could potentially slow down if the computer if performing another task, such as an unexpected virus scan.

6.4.3 Terminating the LabVIEW program

The user can stop the movement of the device and exit the LabVIEW program by pressing the STOP button of Fig 6-6. Providing this functionality proved challenging because in order to safely stop the device the amplifier needs to be disabled. Each axis has an Enable Output signal, but the Copley amplifier only has one Enable Input port. The challenge was combining these two Enable signals to turn inhibit the output of the amplifier at the desired time. The solution was to use a digital OR gate, shown in Fig 6-7.

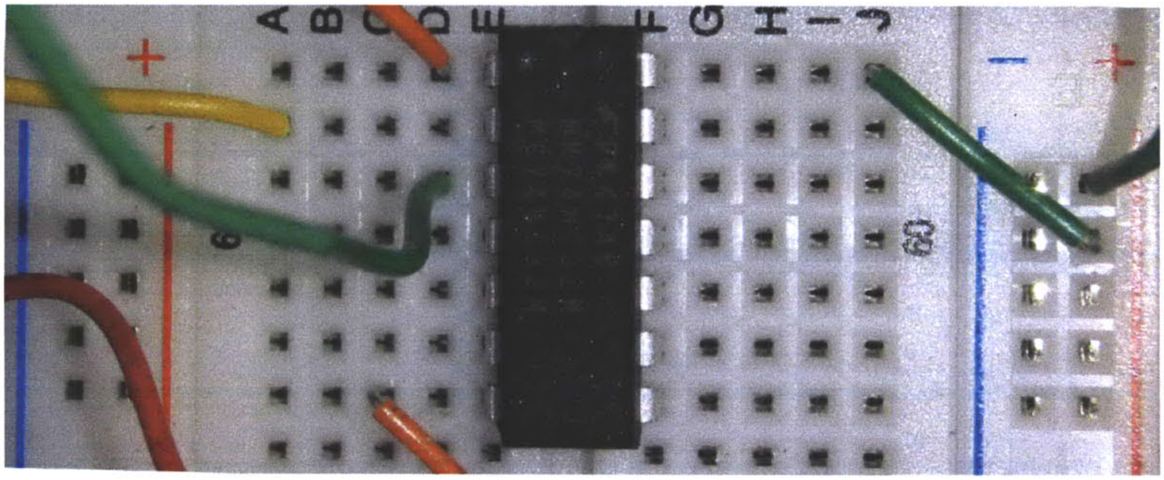

Figure 6-7: Digital OR gate used to OR the two Enable signals. Chip is a MM74HC32 Quad 2-input OR gate from Fairchild Semiconductor

When either axis is enabled, the output of the OR gate is high, and the amplifier is enabled. When both of the axes are disabled the output is low and the amplifier is disabled. Future work to improve the safety of the system would be to use an exclusive or (XOR) gate so that if both of the axes are mistakenly enabled at the same time then the amplifier is disabled.

6.5 Summary

This chapter described improvements to the usability of the device over the pure force control strategy of Chapter 5. These improvements included high-level logic that stops controlling the contact force when it detects that the device is no longer in contact with the patient. It moves the device into its center position so that the next time the user makes contact he/she is less likely to reach a limit. Another improvement was a 'soft start' that makes it easier for the user to begin using the device. The user controls the contact force, monitors the position, and stops the device via the user-friendly front panel.

Chapter 7

Modeling

This chapter describes the modeling that we performed in order to improve the design of the control system. The first section models the device when it is not in contact with the environment, and can be described by a first-order system with damping. Next we model the system when it is affixed rigidly to a frame and placed in contact with a tissue phantom. This can be described by a second-order system. In the last section we model the device when it is held in the hand of the ultrasound technician and placed in contact with the environment. We describe this interaction with a 6^{th}-order model. We evaluate the validity of the first two models with experimental data. We found that the actual responses were slower than expected, which could be the result of unmodeled trajectory smoothing by the motion controller.

7.1 Position Control

We first investigate the performance of the device when it is fixed rigidly to an external frame and not in contact with the environment. The frame is constructed from 80/20 extrusion and enables the device to be placed as the desired distance from a tissue phantom. A picture of the frame is shown later in Fig 7-7. We would like to see how well the device can achieve a target position. A diagram of the setup is shown in Fig 7-1.

In this setup the ultrasound probe, force sensor, and mounting plates are not

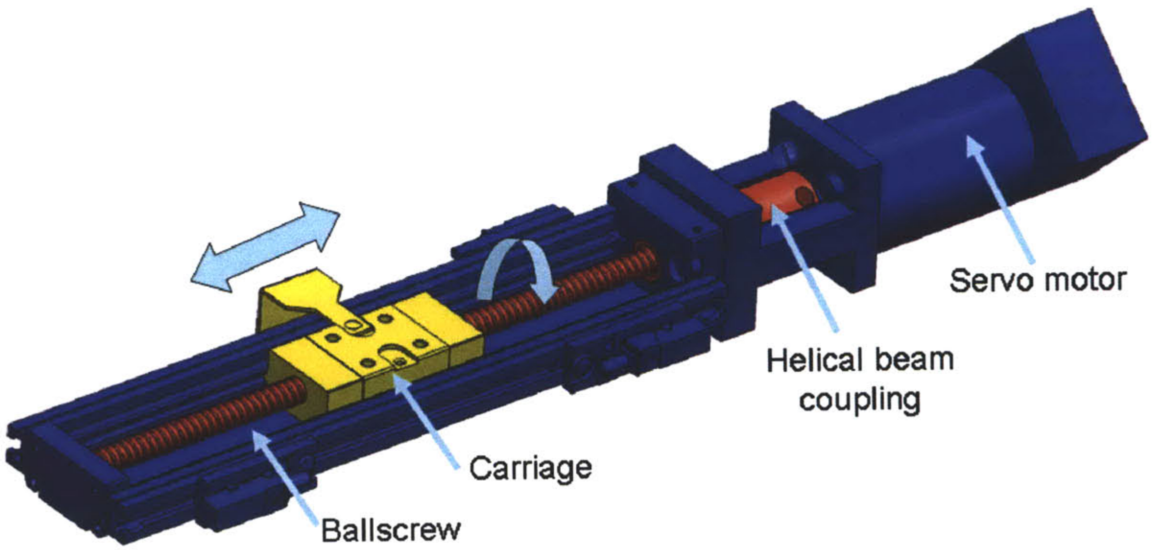

Figure 7-1: System used to validate the model for position control. The outside of the actuator (blue) is fixed rigidly to the frame. The ballscrew is free to rotate and the carriage is free to translate.

attached and the carriage is empty.

In modeling the system we first identify the independent energy storage elements. Since the device is not in contact with anything, there is no stiffness, only moving masses. The rotating mass consists of the motor rotor, coupling, and ballscrew shaft, which rotate together (we assume for now that the helical-beam coupling and shaft are infinitely rigid). The translating mass is simply the actuator carriage. As the shaft rotates a given angle, the carriage translates a proportional amount. Since the screw pitch is 2mm, the carriage translates 2mm each time the screw rotates once. Thus, the motion of the carriage and the screw are coupled. This means that there is only one independent energy storage element, a translating mass, which makes this a first-order system.

Since the only way we have of measuring position is from the encoder output, we constuct a model in the rotational domain. This enables us to more easily compare the model prediction with the experimental data. Since the rotation of the shaft is coupled to the translation of the carriage we look for a way to represent the two inertias as one. A kinetic energy balance enables us to map the translational inertia of the carriage into an effective rotational inertia by Equation 7.1:

$$\frac{1}{2}J_{eff}\omega^2 = \frac{1}{2}mv^2 \tag{7.1}$$

Where J_{eff} is the effective rotational moment of inertia seen at the motor, caused by the translation of the carriage of mass m at velocity v; ω is the rotational speed of the shaft. Since the carriage translational speed is related to the ballscrew rotational speed by the screw pitch L (in m/rad), the effective rotational inertia of the carriage J_{eff} is then

$$J_{eff} = L^2 m \tag{7.2}$$

The total rotational inertia is thus

$$J_{tot} = J_{eff} + J_{rotor} + J_{ballscrew} + J_{coupling} \tag{7.3}$$

The inertial contributions from each element are shown in Table 7.1

Parameter	J_{tot}	J_{eff}	J_{rotor}	$J_{ballscrew}$	$J_{coupling}$
Value (*$10^{-9}kgm^2$)	**2104**	4	1100	170	830

Table 7.1: Rotational inertia contributions from each moving element

From Table 7.1, we see that the effective rotational inertia of the carriage is negligible.

7.1.1 Friction

The rotation of the shaft is impeded by three sources of friction: 1) friction between the shaft and its ball bearings at each end, 2) friction between the shaft and the ballnut contained in the carriage, and 3) linear friction between the carriage and the wall. We assume that all of these sources of friction can be combined into one parameter b_{rot}. The model then involves one rotating element which is resisted by friction, as shown in Fig 7-2.

There are a number of possible forms the damping coefficient could take. It could

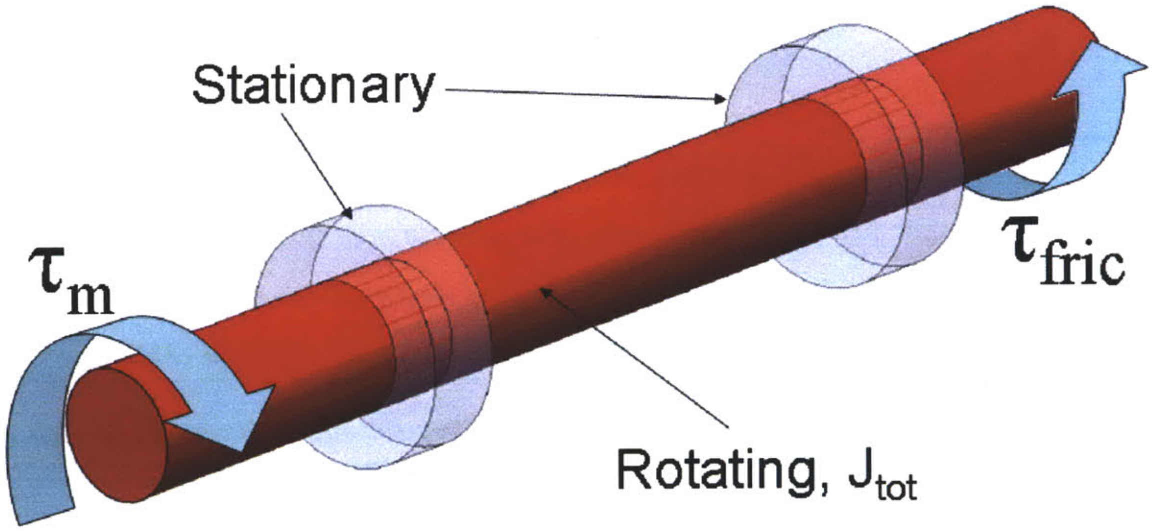

Figure 7-2: 1^{st}-order model. Rotation of shaft is opposed by friction torque τ_{fric} caused by friction with the stationary bearings

contain either a viscous damping term or a Coulombic friction term. The force of friction in each of these regimes is shown in Fig 7-3.

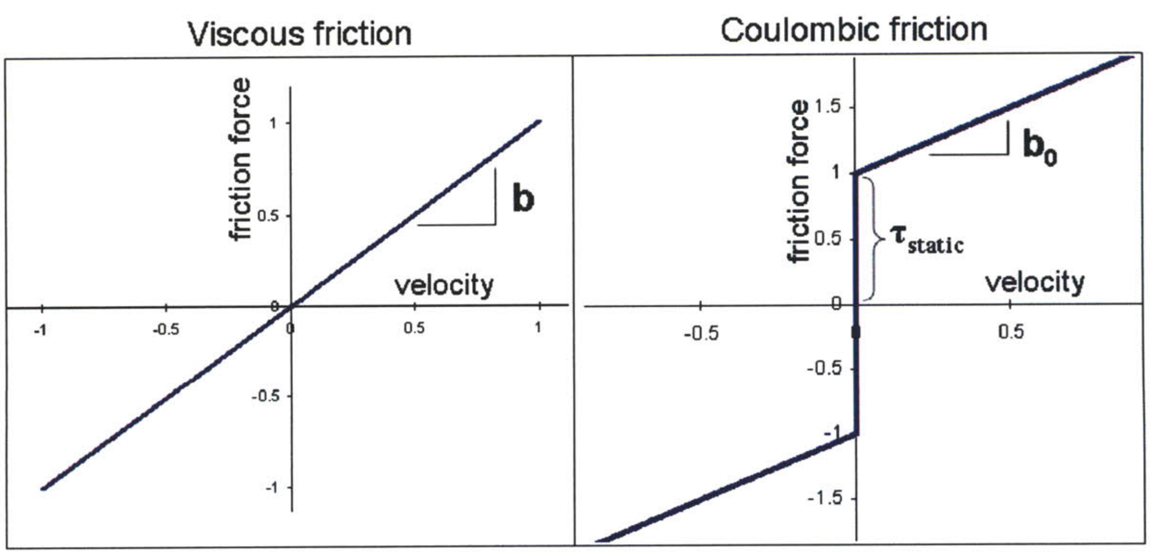

Figure 7-3: Viscous and Coulombic friction

Pure viscous friction is by far the simpler of the two to model. It represents a force that is proportional to the rotational velocity of the shaft. The constant of proportionality is b from Fig 7-3. The Coulombic friction, on the other hand, consists of a static term and a dynamic term. When the torque exerted on the shaft is less than a certain value, τ_{static}, the shaft does not move, and the resistive torque on the shaft matches the applied torque. When the applied torque exceeds τ_{static}, the shaft starts to move and enters the dynamic regime. In this regime the resistive torque on the shaft is essentially a constant value, although it might increase slightly with velocity by the constant of proportionality b_0 from Fig 7-3. Coulombic friction is thus more difficult to model.

We created a first-order model in Simulink and included a general Coulombic friction block. A block diagram of the model is shown in Fig 7-4.

The block diagram includes velocity and acceleration saturation blocks because the controller limits the velocity and acceleration. The output voltage from the PID controller is limited to ± 10V by the D/A converter. By changing the τ_{static} and the b_0 parameters in the Coulombic friction block, the friction can be made to be either of the two types from Fig 7-3.

The major unknowns in this model are the τ_{static} and the b_0 parameters of the Coulombic friction block. Two experiments were performed to estimate these values. The τ_{static} term represents the static torque that must be overcome to make the motor start moving. To estimate this parameter we hung known weights on a string attached to the circumference of the coupling. We recorded the mass required to make the shaft just start to move, and from this calculated the static friction torque. There was much variability and non-repeatability in the static torque value, from 9mNm to 15mNm, and sometimes the shaft would start moving and then stop again. Perhaps certain areas of the shaft had less lubrication than others.

The parameter b_0 represents the dependence of friction torque on the rotational speed of the shaft. In order to determine this parameter we ran the motor at constant known velocities and recorded the input current. Since the input current is proportional to the applied torque by the torque constant K_t we expect the current to increase as velocity increases. We found however that the friction torque is roughly constant across velocities, suggesting that b_0 should be zero. The actual friction torque experienced by the shaft is shown in Fig 7-5.

Our model approximated the data in the following test: we commanded a 125

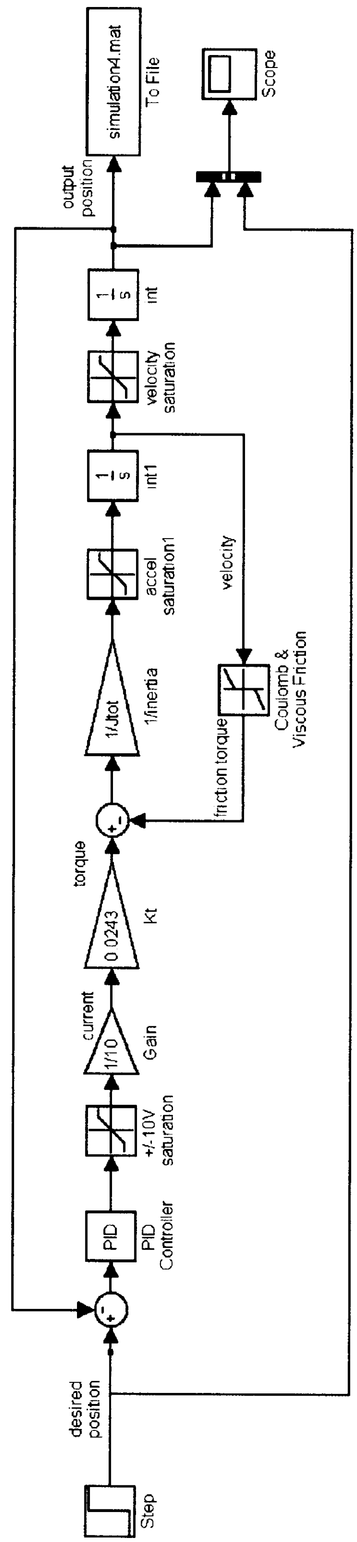

Figure 7-4: First-order simulink model to predict position response to step change in desired position when not in contact.

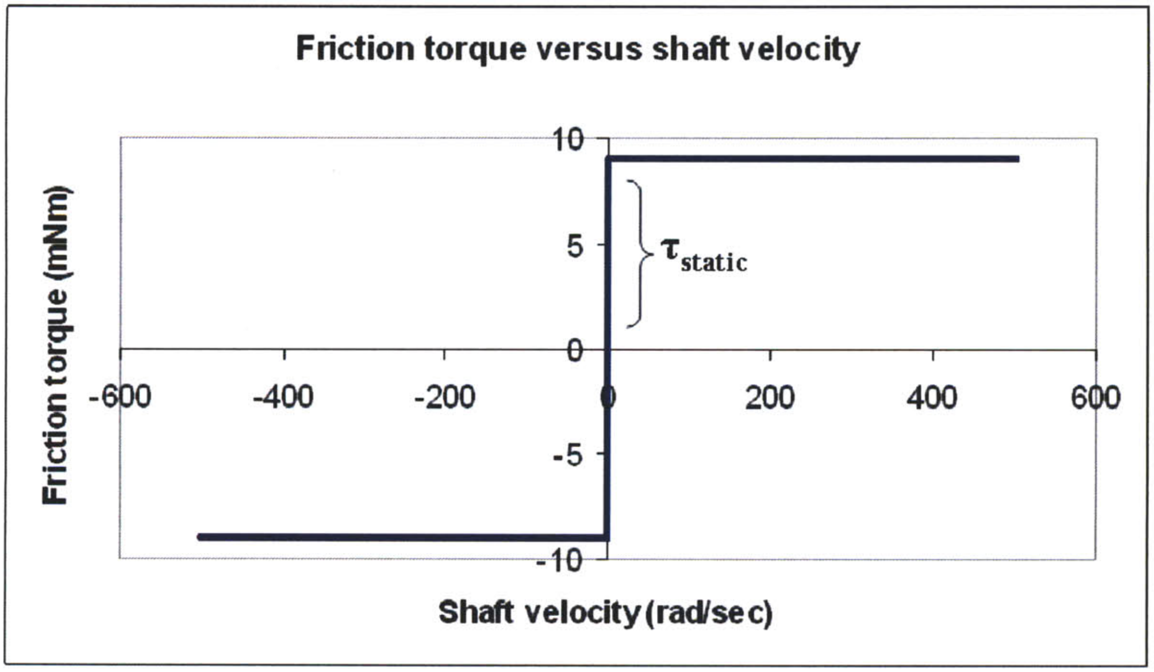

Figure 7-5: Measured frictional torque on ballscrew shaft.

count (22.5 ° since the encoder is 2000cts/rotation) step change in desired position and recorded the output position. We set the acceleration and velocity limits high enough so that the limits were not encountered. We kept the step size around 125 counts or less otherwise the output from the PID controller would reach the +10V ceiling and the response would be difficult to model.

Since there was still a great deal of uncertainty in τ_{static} and the b_0, we adjusted these parameters in the model until there was good agreement between the model and the actual data. A comparison of the model with the actual data is shown in Fig 7-6.

The 'basic simulation' is from a simulation assuming only viscous friction with coefficient b_{rot} and without acceleration and velocity limits. The value for b_{rot} that gives the closest approximation to the real data (in the least-squares sense) was found to be $b_{rot} = 0.005\frac{Nm}{rad/sec}$. The second simulation takes into account the acceleration and velocity saturation limits. The third simulation takes the saturation limits into account along with full Coulombic friction. The values for b_0 and τ_{static} that produced the closest (qualitative) approximation were $b_0 = 0.015$Nm and $\tau_{static} = 0.002\frac{Nm}{rad/sec}$.

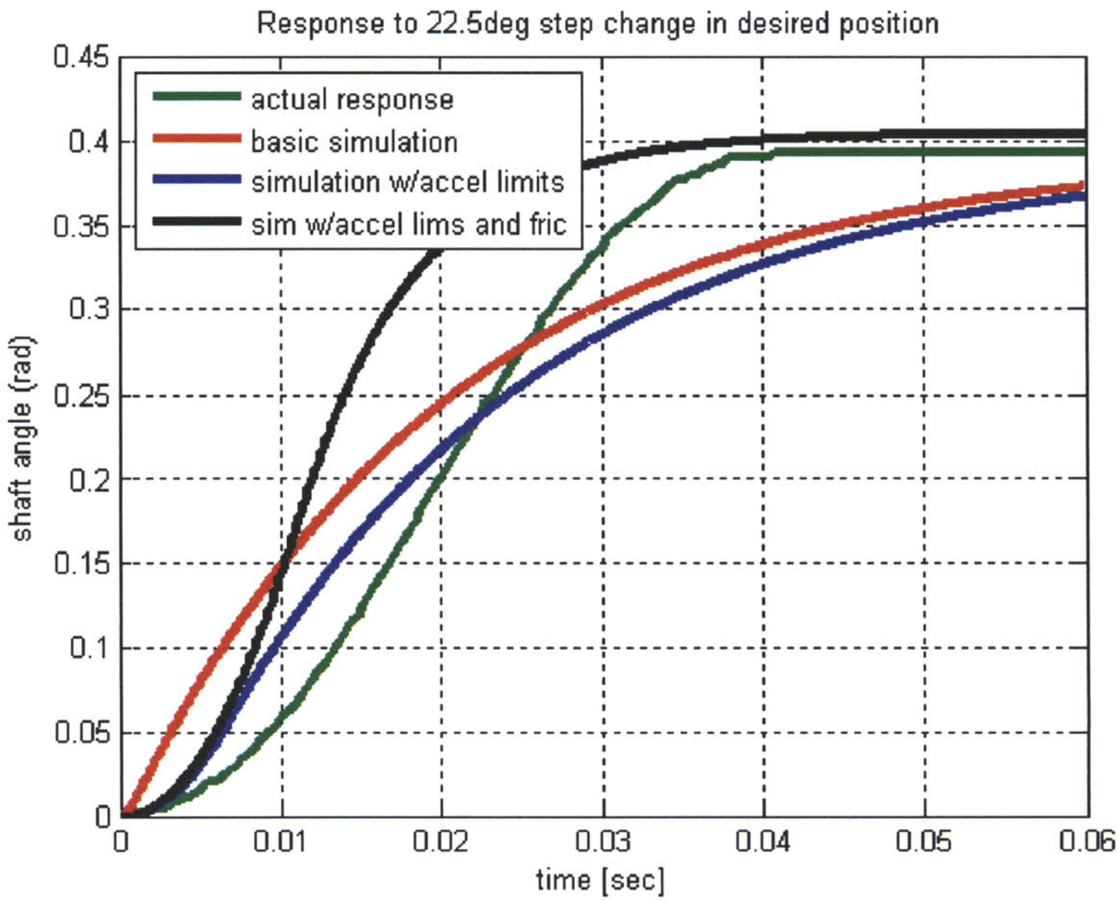

Figure 7-6: Comparison of 1^{st}-order models with actual data.

These parameter values were used in the more complex model, the 2^{nd}-order model.

From Fig 7-6, the simulation with acceleration limits that includes coulombic friction (last model) matches the data the best. However the response of the actual system is slower than expected, which suggests some unmodeled dynamics are at work.

7.2 Force Control

Next we increase the complexity of the model and place the device in contact with the environment. Eventually we would like the model the interaction between the device and actual human tissue, but first we model the interaction with a more repeatable and consistent object, a tissue phantom. The phantom is a material that has roughly the same mechanical properties as human tissue.

We fix the device rigidly to a frame and place it in light contact with the phantom. Then we command a step change in the desired contact force. We record the position response of the motor. The setup is shown in Fig 7-7.

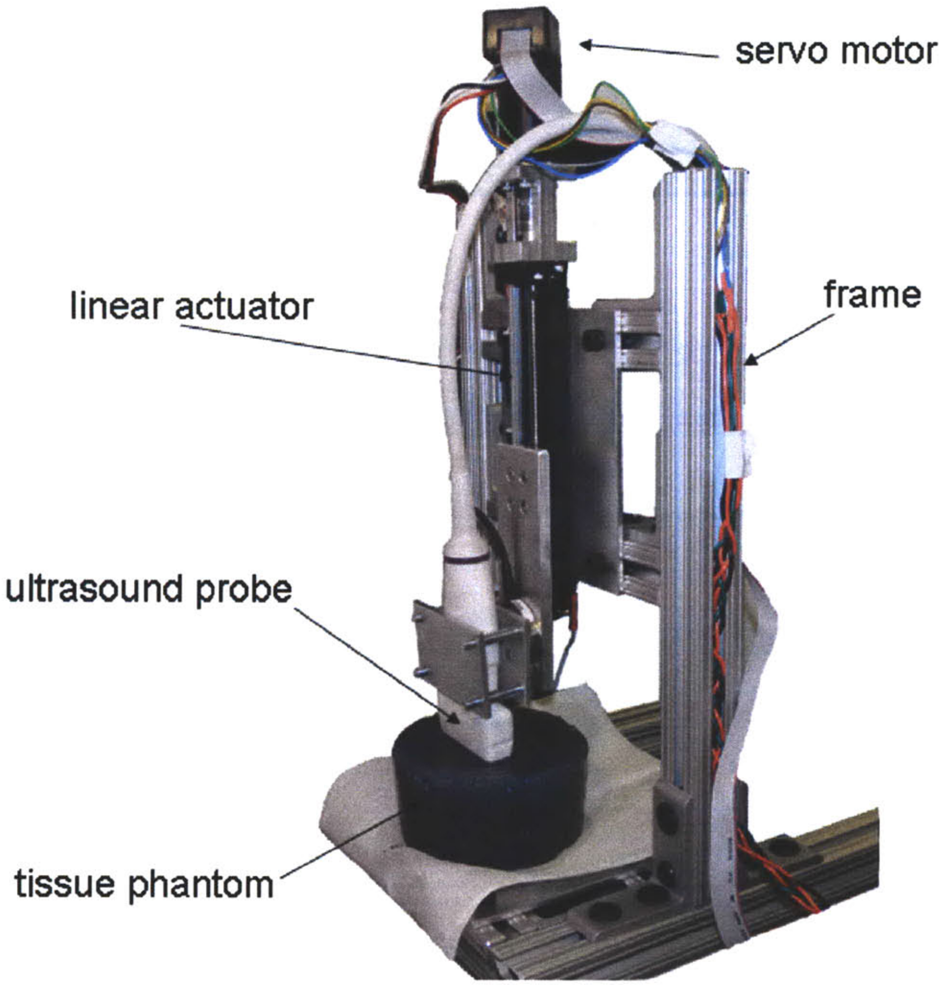

Figure 7-7: Test setup. Ultrasound probe system is fixed to rigid frame. The probe is shown in contact with a tissue phantom, a material with similar mechanical properties to those of human skin.

The simplest model that could describe the dynamics of the system consists of a single moving mass which makes contact with the phantom, shown in Fig 7-8.

The moving mass consists of the ultrasound transducer, force/torque sensor, along with the mounting hardware and is shown in orange. In the same manner as the 1^{st} order model the translational inertia of the ultrasound probe, force sensor, and

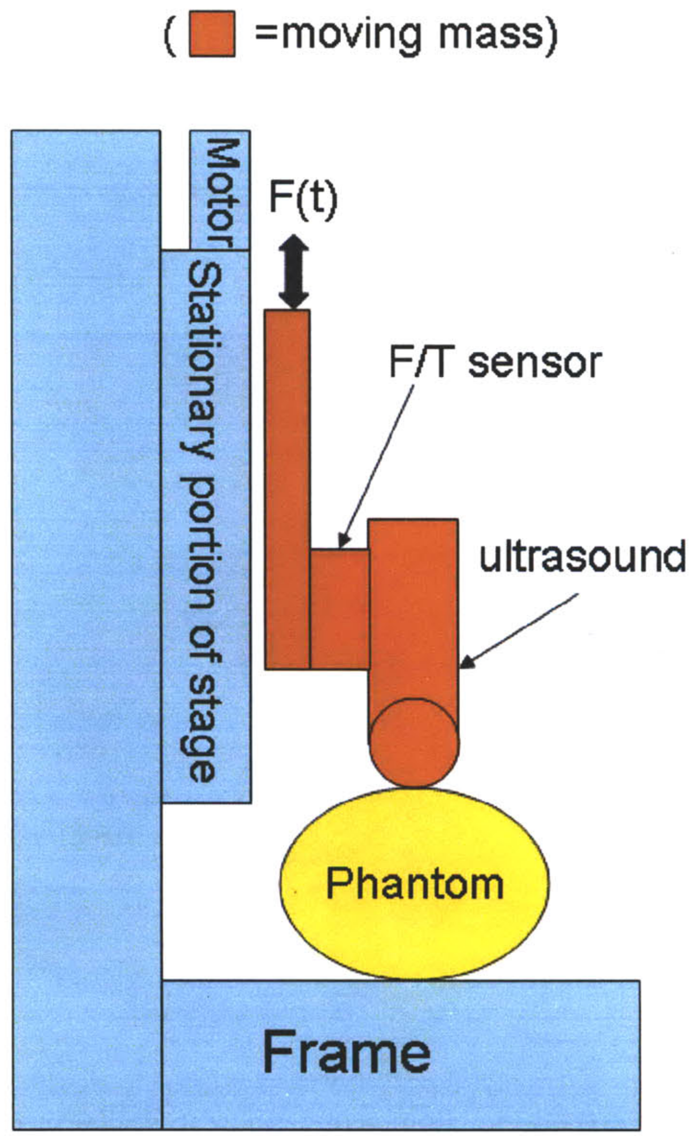

Figure 7-8: Second-order model for actuator in contact with phantom. Orange indicates moving mass.

mounting plate can be mapped to an effective rotational inertia seen at the motor called $J_{ultrasound}$. The contributions of each inertia to the total effective rotational inertia are shown in Table 7.2.

Parameter	J_{tot}	J_{eff}	J_{rotor}	$J_{ballscrew}$	$J_{coupling}$	$J_{ultrasound}$
Value ($*10^{-9} kgm^2$)	**2140**	4	1100	170	830	36

Table 7.2: Rotational inertia contributions from each moving element. As before J_{eff} refers to the effective rotational inertia of the carriage.

We see from Table 7.2 that once again the inertial contribution from the translating masses is negligible (<2%) because the screw lead is small.

The interaction between the device endpoint and the environment (the phantom in this case) is characterized by a stiffness k_e and a viscous damping b_e. We switch momentarily to the linear domain to describe the mechanical properties of the phantom. In the same way we mapped the translational inertia of the ultrasound, force sensor, etc., to a rotational inertia, we can also map the rotational inertia of the rotating elements into an effective translational mass, which combined with the actual translating masses gives a total mass M_{tot}. A 2^{nd}-order model of the device in contact with the phantom is shown in the linear domain in Fig 7-9.

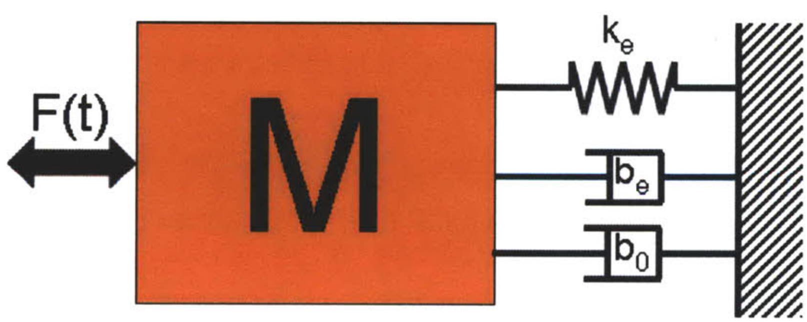

Figure 7-9: 2^{nd} order model of the system in the linear domain

The phantom parameters are k_e and b_e, and the rotational friction is represented in the linear domain as b_0. The goal is now to map the phantom parameters into the rotational domain. First we map the linear stiffness k_e into a rotational stiffness k_r. In the linear domain, we know that $F_{spring} = k_e x$. We would like to convert this into the form $\tau = k_r \theta$. Since the ballscrew converts rotation into translation as well as torque into force, the following equations are true: x = Lθ and F = τ/L. Rearranging the equations gives Equation 7.4:

$$\tau = \frac{k_e}{L^2}\theta \tag{7.4}$$

Thus, $k_r = k_e L^2$. Similarly, since we assume that the phantom exhibits only viscous damping, the linear viscous damping coefficient b_e mapped into the rotational domain is $b_r = b_e L^2$. The entire system can be modeled in the rotational domain as a shaft with an external stiffness and two damping sources, as shown in Fig 7-10.

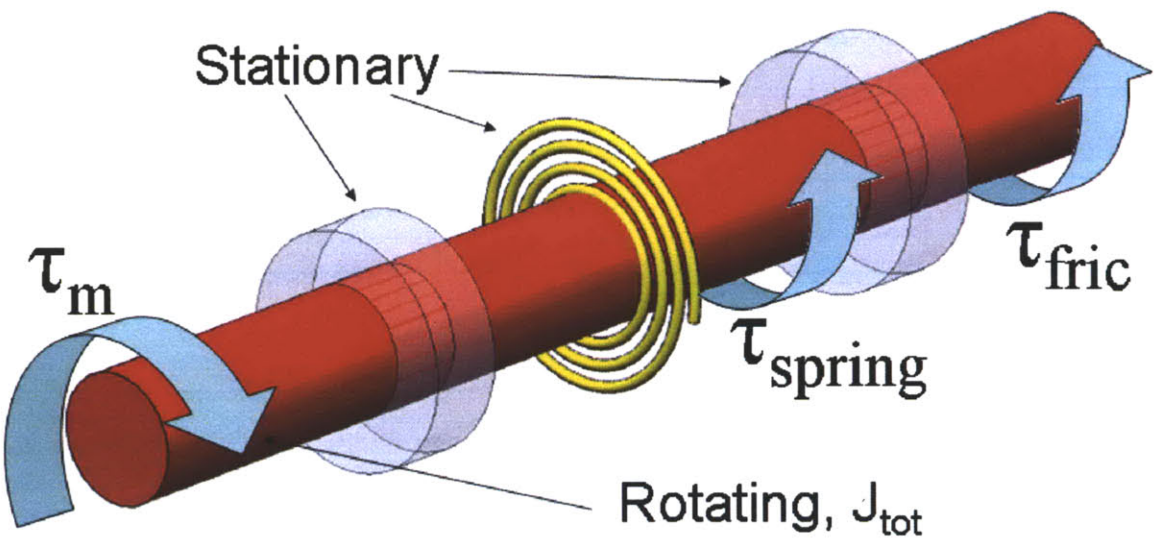

Figure 7-10: 2^{nd} order model in the rotational domain

The motor current provides the input torque τ_m which is resisted by the effective spring and damping terms. The Simulink block diagram for the second order model is shown in Fig 7-11.

In this block diagram, the input is the desired force F_{des} and the output is the actual position. Ideally we would like to compare the desired force with the output force, but unfortunately we cannot record the output force fast enough. Since a calculation needs to be performed on the force voltages in order to calculate the actual forces, this calculation must be done in LabVIEW. The maximum rate for reading the forces was only 250Hz, far too slow to observe the complete dynamics of the system.

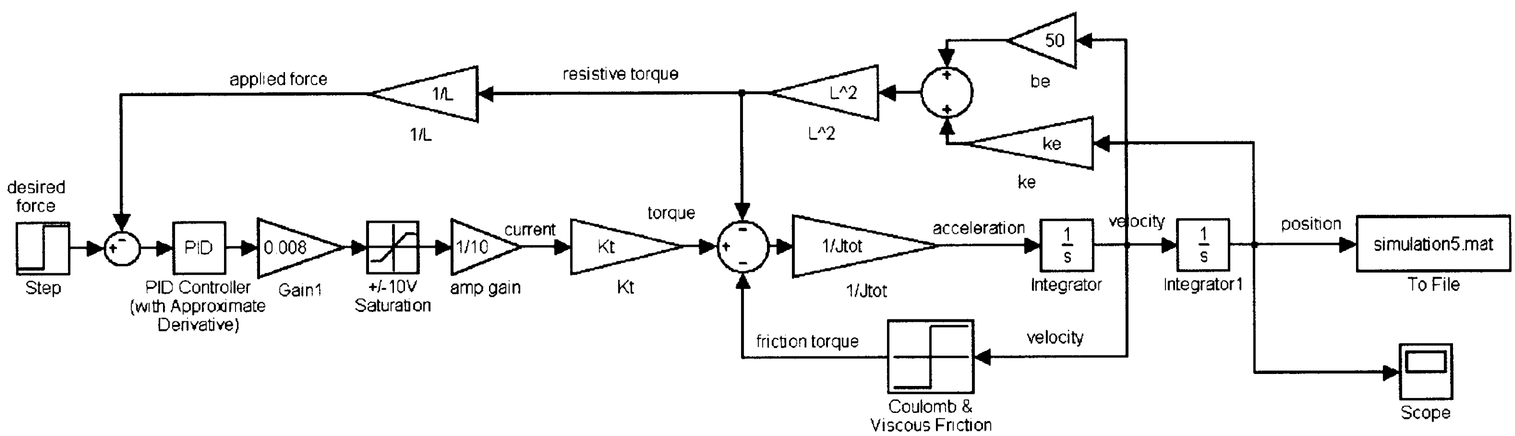

Figure 7-11: Block diagram of second-order system

We considered using an oscilloscope to speed up the force reading rate. Since the force output consists of six signals which require computation to determine the actual force, the scope would need six inputs. At the time this thesis was written we did not have the hardware to perform this experiment.

However, the Copley amplifier has a built-in software oscilloscope that can be used to rapidly record parameters like motor position, velocity, and currents. We used the Copley CME2 software to record the position at a rate of up to 17kHz, sufficiently fast to record the dynamics in which we are interested.

7.2.1 Phantom Stiffness and Damping Calculation

The phantom stiffness was calculated by increasing the contact force between the phantom and the probe while recording the indentation depth. It was found that the force was proportional to the indentation depth by about 3000N/m, which represents the phantom stiffness. Once again, the parameters with the highest uncertainties in this model relate to the damping and frictional terms, especially the viscous damping term for the phantom.

To attempt to find the viscous damping coefficient of the phantom, we placed the device in contact with the phantom and commanded the actuator to move at a constant velocity. We recorded the increase in force as the indentation depth increased, until the actuator had indented 6mm into the phantom. If we treat the phantom itself as a second order system with stiffness, damping, and mass, the equation relating the applied force F(x) to the indentation depth x should be given by Eqn 7.5:

$$F = kx + b\dot{x} + m\ddot{x} \tag{7.5}$$

If the actuator moves at a constant velocity, the acceleration term disappears and the equation becomes

$$F = kx + b\dot{x} \tag{7.6}$$

Since we already know k_e = 3000N/m, we should be able to find b_e, given x

and F(x). However, using the pseudo-inverse we can actually find the least-squares approximation to both k_e and b_e given F(x) and x. We first rewrite Eqn 7.6 as

$$F_{Nx1} = X_{Nx2}B_{2x1} \tag{7.7}$$

Where N is the number of data points collected, F is the vector of recorded forces, X is a Nx2 matrix of the recorded positions and velocities, and B is a 2x1 vector $[k_e\ b_e]^T$, which we would like to determine. Since we have N equations and only two unknowns, we have an overconstrained problem. We find a least-squares approximation for B. Equation 7.8 gives the least-squares approximation [8] for B:

$$\hat{B} = [(X^TX)^{-1}X^T]F \tag{7.8}$$

With this method in mind we gathered position versus force data for several runs, an example of which is shown in Fig 7-12.

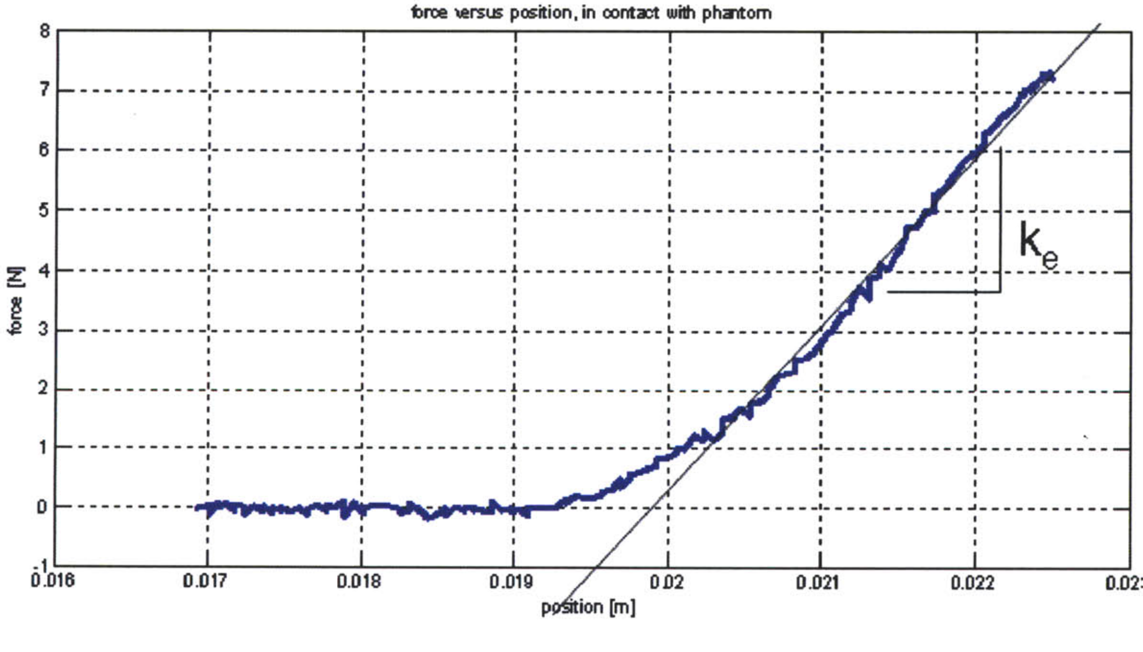

Figure 7-12: Contact force versus position when in contact with the phantom.

Using this method the value for k_e was found to be approximately 3000N/m. This represents the slope of the F(x) versus x plot. The modulus of elasticity E can be determined from the stiffness k_e via Eqn 7.9:

$$k = \frac{EA}{L} \tag{7.9}$$

Where A is the contact area of the ultrasound probe ($7*10^{-4}m^2$) and L is the effective thickness of the phantom under compression. Since the compression depth is less than 5mm, we assume L is roughly 1cm. This gives an elastic modulus of 43kPa for the phantom. By comparison, [17] gives an average elastic modulus of 28.7kPa for the breast.

Determining the damping coefficient was less straightforward. The challenge is that the position x from Equation 7.5 needs to be the indentation depth of the ultrasound probe. From the graph, it is subjective to determine where the ultrasound probe makes contact with the phantom. It looks to be in the vicinity of $x = 0.019$m, but the curvature of the trace suggests full contact might not be made until $x = 0.02$m. The ultrasound probe itself is curved and it was difficult to ensure that surface of the probe and phantom were parallel. This could explain the zone of intermediate contact.

We found that the value selected for the contact position x_0 has a large effect on the damping coefficient b_e. In this case, for $x_0 = 0.01991$m, the least-squares approximation gave $b_e = 2.0\frac{Nm}{rad/sec}$. For $x_0 = 0.01927$m, least-squares gave $b_e = 99\frac{Nm}{rad/sec}$.

Although this method gives a good approximation for k_e it is not reliable in determining b_e, the viscous damping coefficient of the phantom.

In order to obtain an approximation for b_e, the value of b_e in the model was varied by hand (along with the τ_{static} and b_0 parameters of the Coulombic Frition block) until the model seemed to match the data. The values that produced the closest approximation to the actual data were $b_e = 50\frac{N}{m/s}$, τ_{static}=0.008Nm, and $b_0 = 0.0001\frac{Nm}{rad/sec}$. The value for τ_{static} is close to the independently-determined value of 0.009Nm-0.015Nm from Section 7.1.1. A plot of the model and actual experimental data for the 2^{nd} order system is shown in Fig 7-13.

The general shapes of the two curves match, but as in the first-order system the

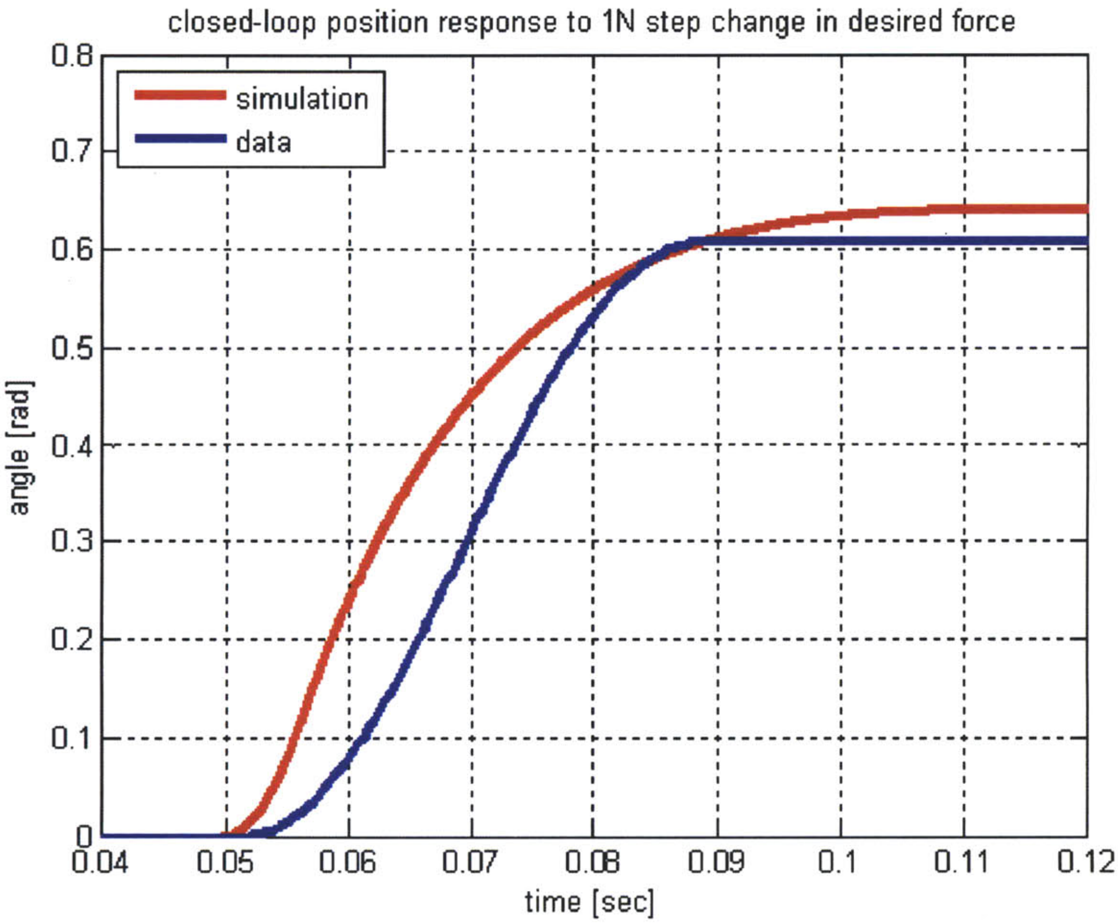

Figure 7-13: Comparison between simulation and actual data for 2^{nd} order system.

actual response for this second-order system is slower than the predicted response.

7.3 Disrepancies between actual and predicted responses

Figures 7-6 and 7-13 show that in both the first- and second-order systems the model predicts a faster response that is actually observed. This could be explained by "S-Curve Smoothing" that occurs by default on the National Instruments PXI-7358 motion controller card. This feature allows the user to specify the maximum acceleration/deceleration and maximum velocity that the motor is allowed to move at. Another feature also allows the user to indirectly control the maximum 'jerk' (time rate of change of acceleration) that the motor is allowed to experience.

The exact behavior of this this S-Curve Smoothing was unknown at the time of this thesis and little documentation is available from National Instruments. Potentially the Smoothing could be implementing a controller that enables once the motor approaches one of the jerk, acceleration, or velocity limits. The controller would try to keep these three parameters below the maximum programmed values, and the controller would be disabled once the the jerk, acceleration, and velocity fall back within acceptable levels. Alternatively there might be a higher-level logic system that simply reduces the command voltage when any of the limits are reached. In either case, such a controller would tend to make the trajectory of the motor smoother and the total response slower than predicted. Modeling the S-Curve Smoothing has so far proved unsuccessful.

In gathering the step response plots, we took care to ensure that none of the acceleration, velocity, or voltage limits were reached. Occasionally we found that for large steps the command voltage met the +10V upper limit, and the output was capped by the amplifier. To eliminate these dynamics we reduced the size of the step command from $\frac{1}{8}^{th}$ of a rotation to $\frac{1}{16}^{th}$ of a rotation, and reduced the gain on the PID controller. Future step commands did not reach the +10V saturation limit. We also set the maximum acceleration and velocity limits very high and observed that the system only reached about 10% of these limits.

Future work is needed to understand the dynamics of the S-Curve Smoothing in order to improve the accuracy of the models.

7.4 Actual-Use Model

The next step is to model the behavior of the device when it is held in the hand of the ultrasound technician and placed in contact with the patient. A higher-order model is necessary to describe this interaction. An example of a 6^{th}-order model is shown in Fig 7-14.

The entire system is held in the hand of the ultrasound technician. The technician

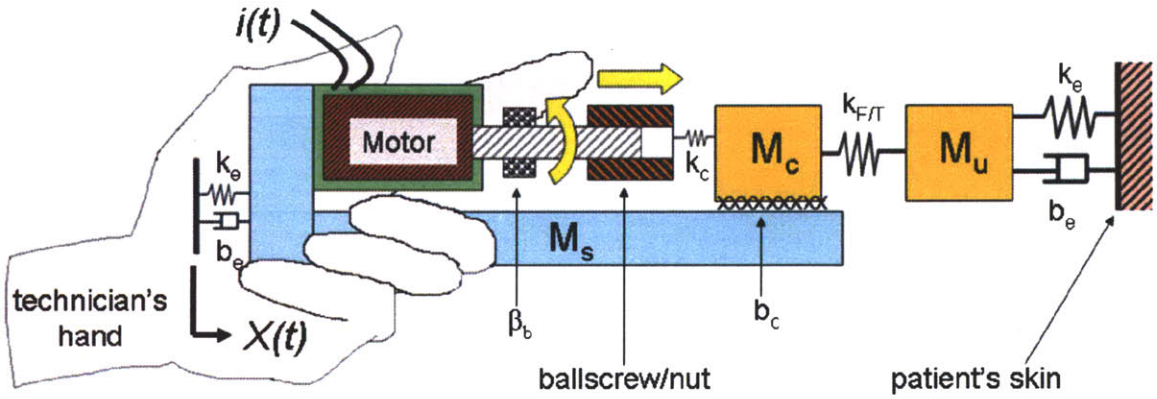

Figure 7-14: 6^{th}-order model for the device held in the hand of the technician while in contact with the patient

places the device in contact with the patient's skin. On one side the device experiences the forces exerted by the technician's hand, while the other side experiences the forces exerted by the patient's body. The inputs to the system are the current i(t) supplied to the motor and the velocity V(t) of the technician's hand. We are interested in the contact force exerted on the patient's body, $F_c(t)$.

Both the contact with the technician's hand and the contact with the patient's body are modeled as visco-elastic interactions [11]. The contact thus consists of a viscous damping term and a stiffness term. The values of the stiffness k_e and damping b_e parameters of the probe-patient interface depend strongly on the type of tissue being examined. At the technician-device interface the stiffness k_t and damping b_t are those of the technician's entire limb, from the hand to the shoulder.

The device consists of three main translating masses: the mass of the stage + motor M_s, the carriage + force sensor mass M_c, and the ultrasound probe mass M_u, along with one rotating mass: the motor rotor + ball screw with rotational inertia J_{tot}. The ultrasound probe is mounted to the force/torque sensor, which has a stiffness $k_{F/T}$. The force/torque sensor is mounted to the carriage M_c which experiences viscous damping b_c when moving with respect to the stage M_s. Between the carriage's ball nut and the ballscrew there exists stiffness k_c. The ballscrew is driven by the servo motor, with total rotational inertia J_{tot}. Viscous damping β_b resists rotation of the shaft. The motor is modeled as a gyrator, thus the current supplied to the motor i(t) is converted to torque by the motor torque constant K_T. The motor is mounted to the stage M_s, which is held in the hand of the ultrasound technician.

In order to evaluate the accuracy of this model we need to move the device at a velocity V(t) with respect to the patient's body while measuring the contact force. Future work includes attaching the device to another linear actuator that can act as the technician's hand to move the device through specific trajectories. In this thesis we do not evaluate the accuracy of this 6^{th}-order model.

7.5 Summary

This chapter modeled three use scenarios for the system. We first modeled the system when it was affixed to the table and not in contact with the environment. We next modeled the system when it was in contact with the environment, but affixed rigidly to a frame. The third, and most complex, model described the interaction of the device and the environment when it was held in the hand of an ultrasound technician. The first two models fit the experimental data relatively well, but the actual responses were slower than expected. The discrepancies could be explained by the built-in S-Curve Smoothing which seeks to keep the jerk, acceleration, and velocity below preprogrammed maximum levels, and which so far we have been unable to model accurately.

Chapter 8

Results

This chapter describes the results of several experiments to evaluate the performance of the device. We first investigated the step response of the system, and then used the system to determine the mechanical properties of the tissue phantom we used. We also compared the ability of the device to maintain a constant contact force to that of human operators. The results have been presented by at the Design of Medical Devices Conference, April 2010 [16].

8.1 Step Response

We first investigated the ability of the system to achieve a desired contact force. The actuator was affixed rigidly to a frame as shown in Fig 7-7 and a tissue phantom was placed beneath it. The phantom had similar mechanical properties to that of skin (described in more detail in Section 7.2.1) and is home-made from 50 parts water / 1 part agar powder.

The endpoint was placed in light contact with the phantom by commanding a 1.0N force in the LabVIEW program. Step changes were commanded in the desired force and the time response of force was recorded. This procedure was repeated for forces between 1N and 10N, forces that would be encountered in a typical carotid artery ultrasound examination [28]. The results are shown in Fig 8-1.

Each of these trials achieved zero steady state error and zero overshoot. In a real

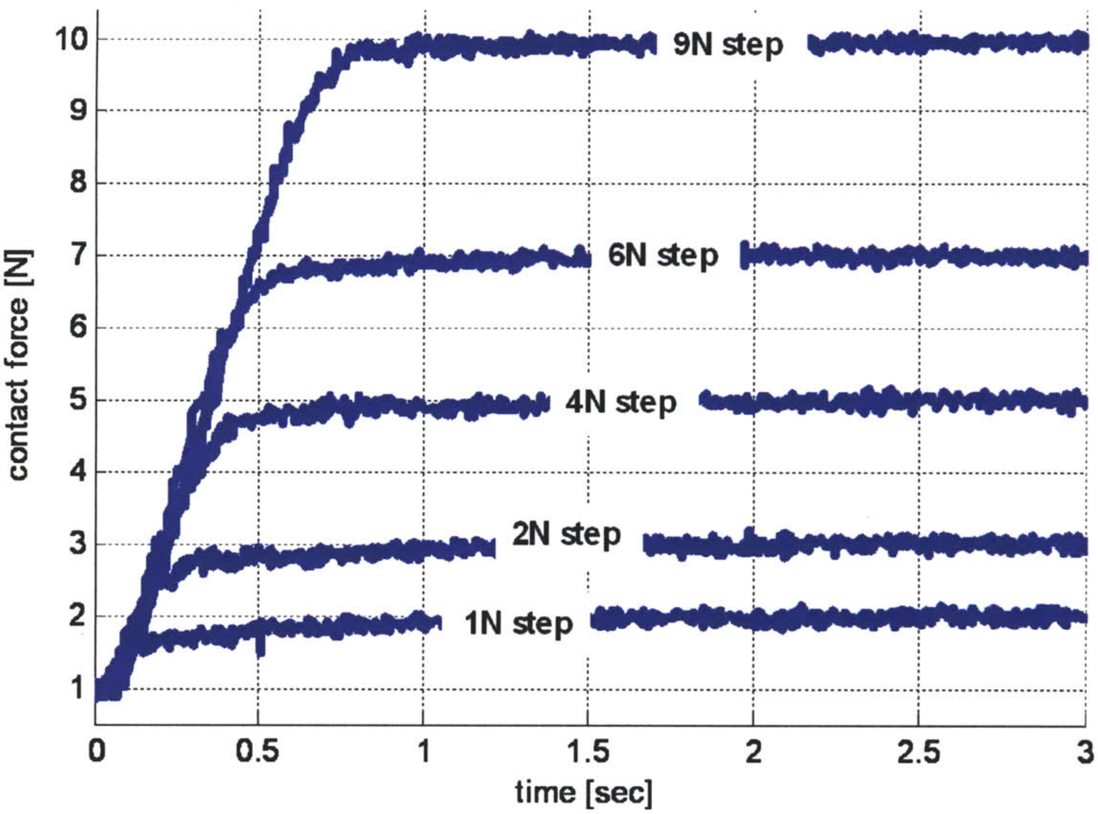

Figure 8-1: Contact force versus time for five step changes in desired force while probe is in contact with the phantom

ultrasound examination it would be critical to avoid high force overshoot because this could potentially injure the patient. The 10% settling times were all less than 0.8 seconds.

8.2 Skin stiffness and Damping calculation

The device was also used to measure the stiffness of a more realistic commercially available breast tissue phantom from Computerized Imaging Reference Systems, Inc (CIRS) of Norfolk, VA. The particular phantom is often used in the field of elastography to validate methods *in vitro.* The device was held on a rigid frame and brought in contact with the phantom at a contact force of 3N. Unit step changes in desired force were commanded from 3N to 13N and the positions recorded at each force.

Using the same method as in Section 7.2.1 the stiffness was calculated to be

827N/m, giving an elastic modulus of E = 29.5kPa., which is close to the literature value of 28.7kPa for the breast [17]. As before, the damping coefficient was much more difficult to calculate, and no method gave reliable estimates for this parameter. This means that the tissue phantom from CIRS has similar mechanical properties as that of the real human breast.

This procedure was also used to characterize the approximate stiffness at the technican's hand-device interface. The author held his hand palm-up against the table and grasped the actuator firmly. The actuator endpoint was placed in contact with a rigid object, and the actuator was commanded to move 2mm at a constant velocity. From five trials the average effective stiffness of the hand-device interface was found to be 1000N/m. This stiffness value could be used as k_t in the future for the 2^{nd} order model.

8.3 Comparison of device performance with and without control

We investigated the ability of this system to maintain a constant probe contact force as compared to that of an untrained and unassisted human operator. Rather than using an actuator and control system to maintain constant force, one alternative would be to simply instrument a conventional passive ultrasound probe with a force sensor (such as [12]) and provide the technician with visual force feedback. We call such a strategy "manual gauge control."

We conducted experiments with twelve untrained operators to characterize the force-control capability of our system and of unassisted operators. Each untrained operator held the system in his/her hand (as in Fig 3-2) and placed the probe in contact with the tissue phantom. To mimic the motions of an actual ultrasound exam, the subjects first held the probe stationary for ten seconds, then conducted a slow, linear sweeping motion across the phantom for twenty seconds, for a total of thirty seconds. The phantom was lubricated with ultrasound gel. The goal was to maintain a constant vertical contact force of 5N while not looking at the probe. The device itself weighed 7.9N so in order to apply 5N the subjects needed to pull upward with 2.9N of force. Each subject performed this procedure in each of the following three scenarios (performed in the order listed):

1. "Manual Gauge Control": The controller was turned off and the actuator locked in position. The subject held the system in his/her hand and attempted to maintain 5N of contact force by focusing on a force gauge displayed on the computer screen.

2. "Automatic Control": The controller was turned on and the subject held the system in his/her hand. The subject looked at the computer screen while the actuator translated to maintain 5N contact force.

3. "Blind": With the actuator off and with no visual force feedback, the subject tried to maintain 5N from his/her memory of 5N from Scenarios 1 and 2. To start the subject was able to look at a force gauge. As soon as the subject reached 5N the force gauge was covered up and we started recording data. Again, the subject was instructed to focus on the computer screen and not the device.

The time history of force was recorded over the entire thirty seconds for each of the twelve subjects in each of the three scenarios. An example of one of these plots is shown for Subject 7 in Fig 8-2.

The "Blind" trace in Fig 8-2 shows that without force feedback the subject's contact force drifted over time. The change in perceived contact force could be a result of muscle fatigue. When the subject switched from holding the device stationary to conducting a sweeping motion at the ten-second mark, the subject's ability to maintain constant force in the blind case diminished.

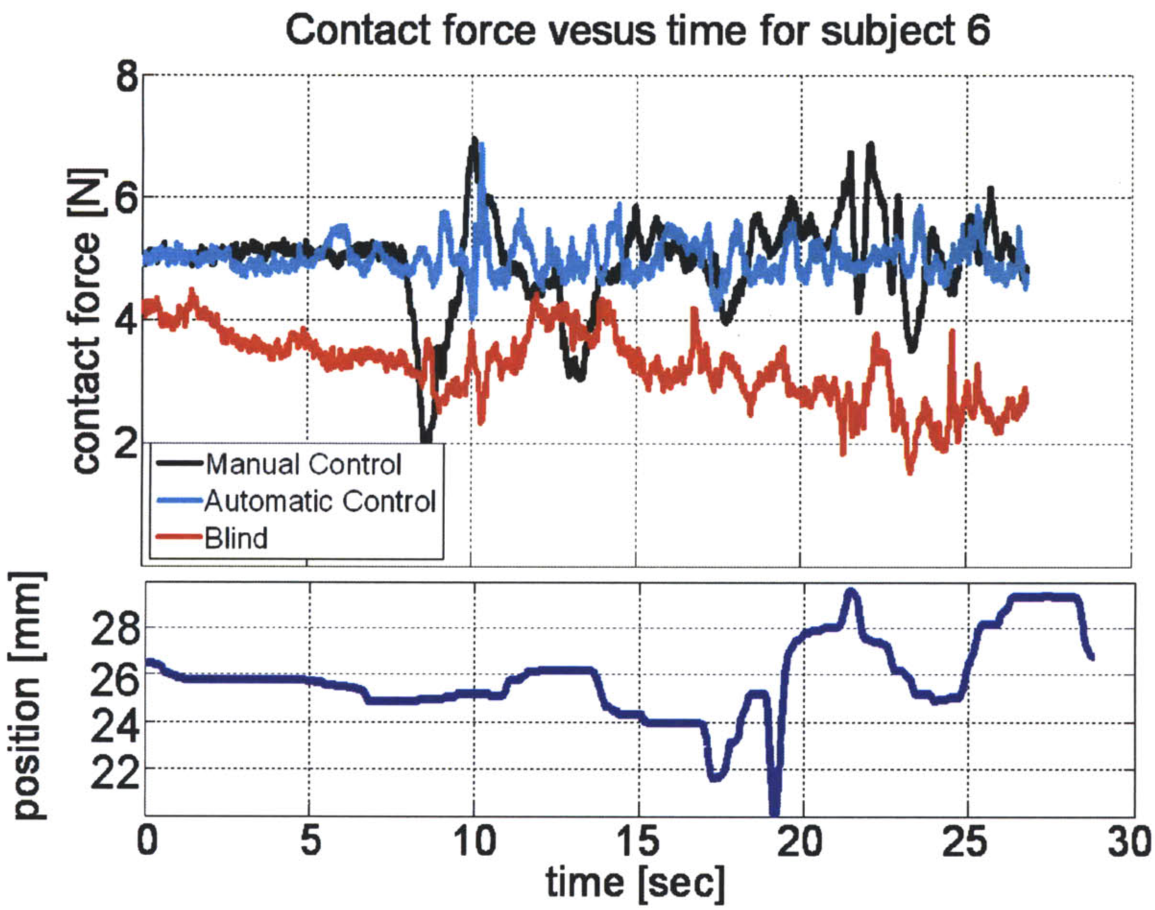

Figure 8-2: (Top): Contact force versus time for Subject 7 in each of the three scenarios. (Bottom): Actuator position versus time in automatic control scenario. The subject held the probe stationary in the first ten seconds and conducted a sweeping motion for the remaining twenty seconds.

8.4 Position Drift

Fig 8-2 also shows the actuator position versus time during Subject 7's Automatic Control scenario (at the bottom). Since the control system is driving the actuator to maintain a constant force, not a constant position, the actuator position fluctuates to compensate for the unsteadiness in the operator's hand. If the operator's hand moves too far however, the actuator will approach one of the limits of travel and must be turned off to prevent damage. In order to keep the actuator within its safe range of motion we provided each subject with a visual indication of actuator position on the computer screen. This consisted of two small lights, one of which would illuminate if the actuator was getting too close to one of the limits.

This feedback was provided to each of the twelve subjects in the "Automatic Control" scenarios presented above. By monitoring the lights, ten out of the twelve subjects kept the actuator within its 7 cm range of motion during the 30 second trial. The other two subjects kept the actuator within range on the subsequent trial.

During a real ultrasound exam the technician will ideally be able to focus on the ultrasound image without needing to concentrate on his/her own hand position. Thus it is important that the position indicators be relatively inconspicuous and do not significantly divert the technician's attention away from the actual ultrasound image.

8.5 Analysis of user studies

Fig 8-3 shows the mean and standard deviation in contact force for each of the twelve subjects in the three scenarios while holding the probe stationary.

The standard deviations in the Manual Gauge Case (average 0.108N) are in general tighter than in the Automatic Case (average 0.160N) which means that the human operator looking at a force gauge is slightly more able to maintain a constant force than the actuated device when the operator is holding the probe stationary. The mean contact forces for the Manual Gauge and Automatic Cases are all within 0.1N of the desired 5N, while the mean contact forces in the Blind Case are as much as 2.1N below the desired 5N.

The performance of the actuated device improves relative to that of the human operator when the operator conducts a sweeping motion instead of holding the device stationary. A plot of the mean contact forces and standard deviations in the case of the moving probe is shown in Fig 8-4.

The averages of the standard deviations for the twelve subjects in each scenario are shown in Table 8.1.

For the case of Manual Gauge control, the standard deviations quadruple when the user moves the probe instead of holding it stationary, while the standard deviations of

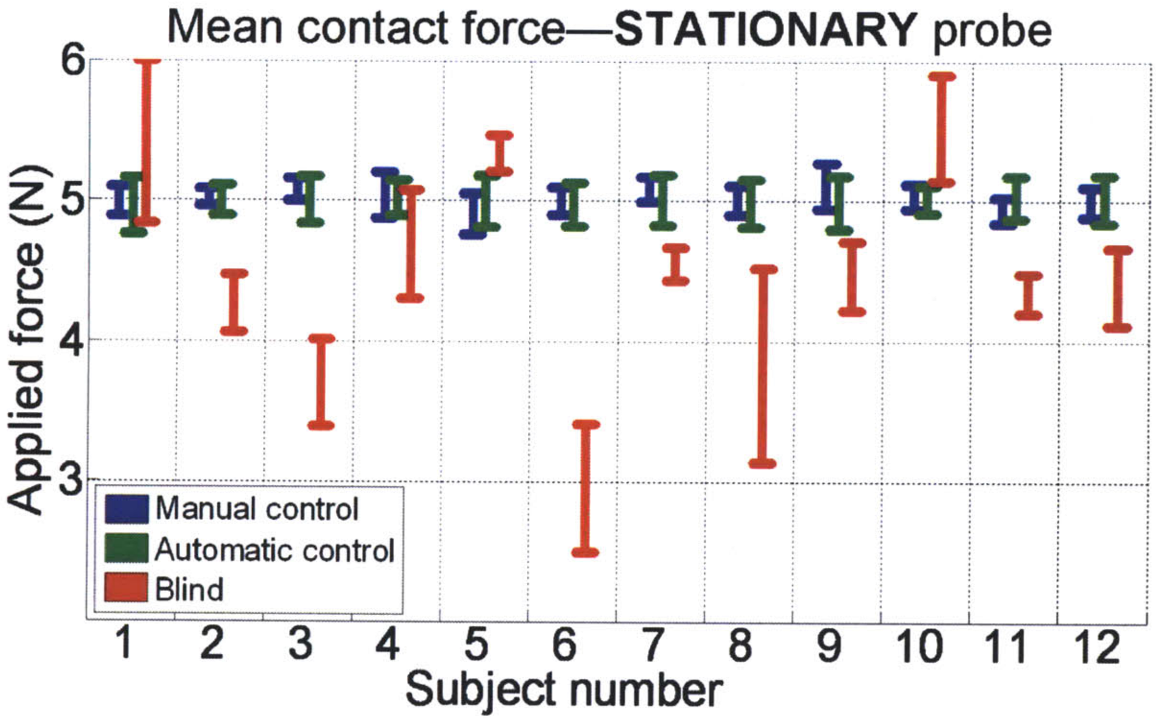

Figure 8-3: Stationary probe: mean contact force for twelve subjects in each of the three scenarios while holding the probe stationary. Error bars indicate standard deviation and the icons represent the mean.

the automatic control increase by 45%. This means that when conducting a sweeping motion with the probe the controller is able to more consistently maintain a constant force than a human operator.

In the actual clinical setting it would be critical that the technician focus on the ultrasound image itself instead of needing to split his/her concentration between the ultrasound image and the force reading (as was done in the Manual Gauge Control case). We believe that the key to achieving this lies in actuating the probe so that the technician does not need to worry about the applied force. One subject commented "it's nice with the control on because then I can relax and not have to focus on the force gauge." Considering the need to focus on the ultrasound image, the force-maintaining capabilities of the Manual Gauge Control case presented here are thus optimistic at best for a realistic ultrasound exam.

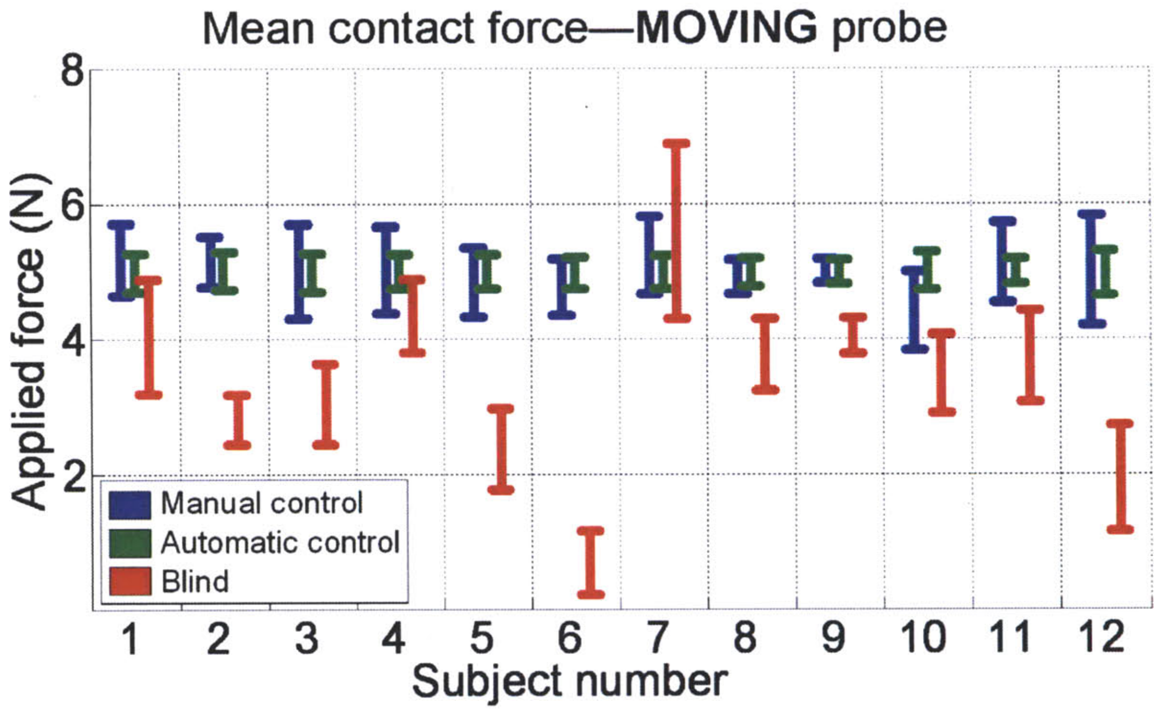

Figure 8-4: Moving probe: mean contact force for twelve subjects in each of the three scenarios while translating the probe. Error bars indicate standard deviation.

8.6 Improving image repeatability

In order to obtain image consistency from one month to the other, the technician needs to position the ultrasound transducer in exactly the same location at exactly the same force. The goal of this device is to fulfill the latter of those two requirements.

We performed an experiment to compare the force repeatability of a person to that of the device. A non-expert human operator held the device in his hand with the controller turned off. He placed the probe in contact with a breast phantom and positioned the device so that an inclusion was within the field of view. He pressed down the probe until the force read 5.0N on the computer screen and captured the ultrasound image (Image 1 in Fig 8-5). Next the controller was turned on and the device gathered the image at 5.0N (Fig 8-5, Image 2). One hour later the subject was asked to acquire the same image at the same force. For this, the subject could see the current image and the previous image on the computer screen but did not know the applied force. The subject positioned the probe and adjusted his contact force

Scenario		Average standard deviations (N) for 12 subjects
Stationary Probe	Automatic	0.160
Stationary Probe	Manual Gauge	0.108
Stationary Probe	Blind	0.329
Moving Probe	Automatic	0.233
Moving Probe	Manual Gauge	0.471
Moving Probe	Blind	0.849

Table 8.1: Average standard deviations for each use scenario

until he perceived that the two images were the same, then an image was captured (Fig 8-5, Image 3). The contact force was also recorded. Next, the subject turned the controller on and captured the same image with the device applying 5.0N (Fig 8-5, Image 4). The four images are shown in Fig 8-5.

Although these four images look similar, the subject was actually applying 3.9N when Image 3 was acquired, even though he thought he was applying 5N. This same experiment was performed with two additional untrained subjects. Although the images were once again similar, the contact forces for the two subjects in the second "blind" scenario were 4.1N and 4.0N.

Fig 8-6 shows the result when the images are subtracted for the first subject.

Image A shows the difference between the two images gathered with the controller off (one image at 5.0N, the other at 3.9N), while Image B shows the difference between the 5.0N images with the controller on. The images were aligned manually prior to the subtraction. Image B is darker in more areas than Image A, suggesting that by applying the same contact force more consistent images can be acquired.

Thus, even though a subject might think that he/she is applying the same contact force to gather two images, the actual contact force could be more than 20% off. With the device, the applied force will be the same within ± 0.1N.

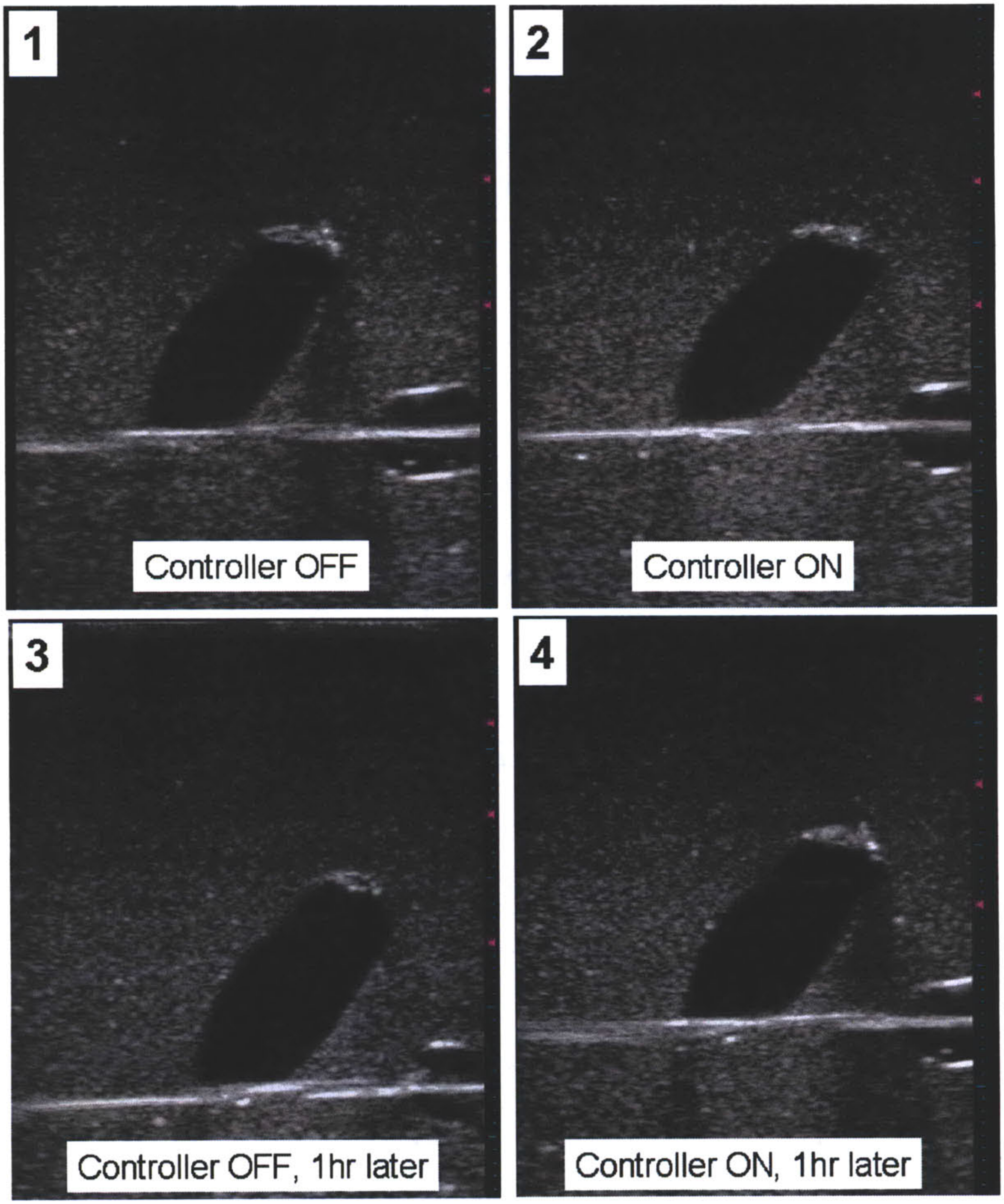

Figure 8-5: Image 1: controller off, applying 5.0N time zero. Image 2: controller on, applying 5.0N, time zero. Image 3: controller ON, one hour later, actual force = 3.9N. Image 4: Controller ON, one hour later, applying 5.0N.

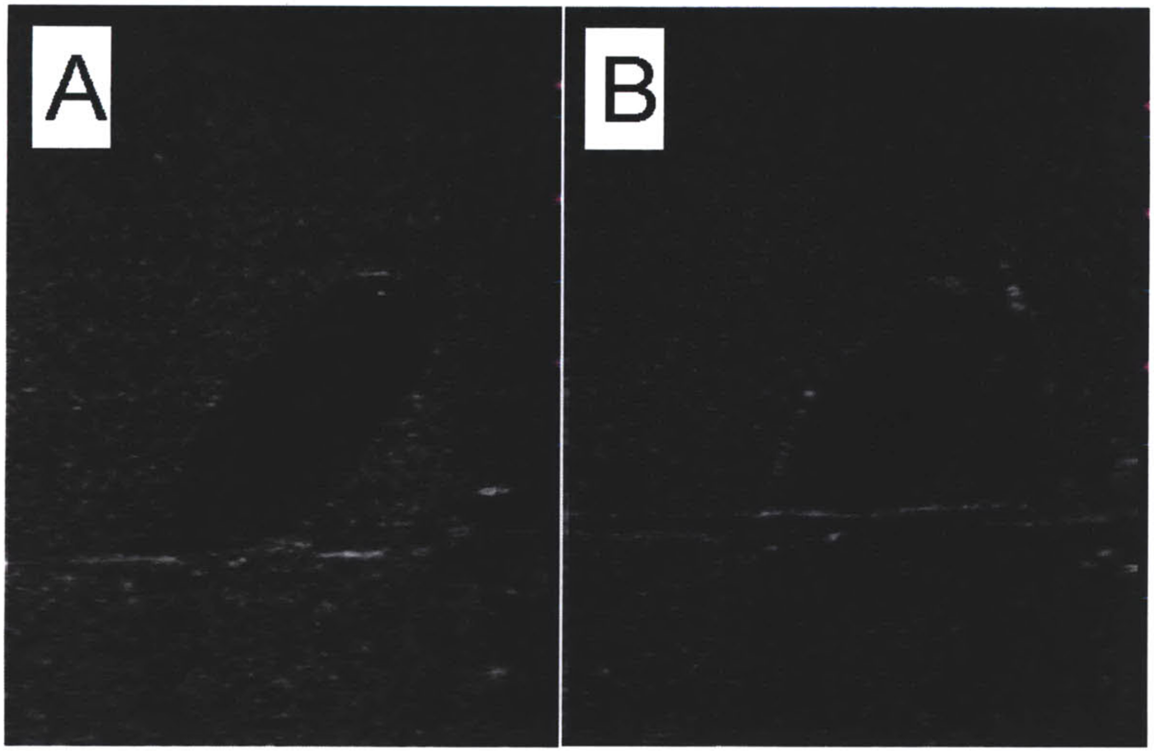

Figure 8-6: Image A: Difference between Images 1 and 2 (force controller OFF). Image B: Difference between Images 3 and 4 (force controller ON)

8.7 Tissue distortion without constant force

To acquire two consistent images of the same tissue from one ultrasound exam another the technician must apply the same force at the same location. From Table 8.1, we observed that in the "Blind" case, the average accuracy of the mean force applied by the unassisted users was ±1.6N from the target force of 5N. In order to quantify the level of tissue distortion that would result from this level of force inaccuracy we gathered nine images from 3N to 7N of contact force at 0.5N increments, shown in Fig 8-7. The total compression depth was 15mm.

From these images we measured the length of the most prominent inclusion and compared it with the nominal inclusion length measured at 5N. Fig 8-8 shows the difference in inclusion length from the nominal 5N image, plotted versus force.

Fig 8-8 indicates that at a 3N contact force the inclusion is about 0.8mm longer than at 5N. The inclusion contracts by 0.3mm at 6N. Thus, with the typical variations in contact force encountered during an ultrasound exam tissue features can change

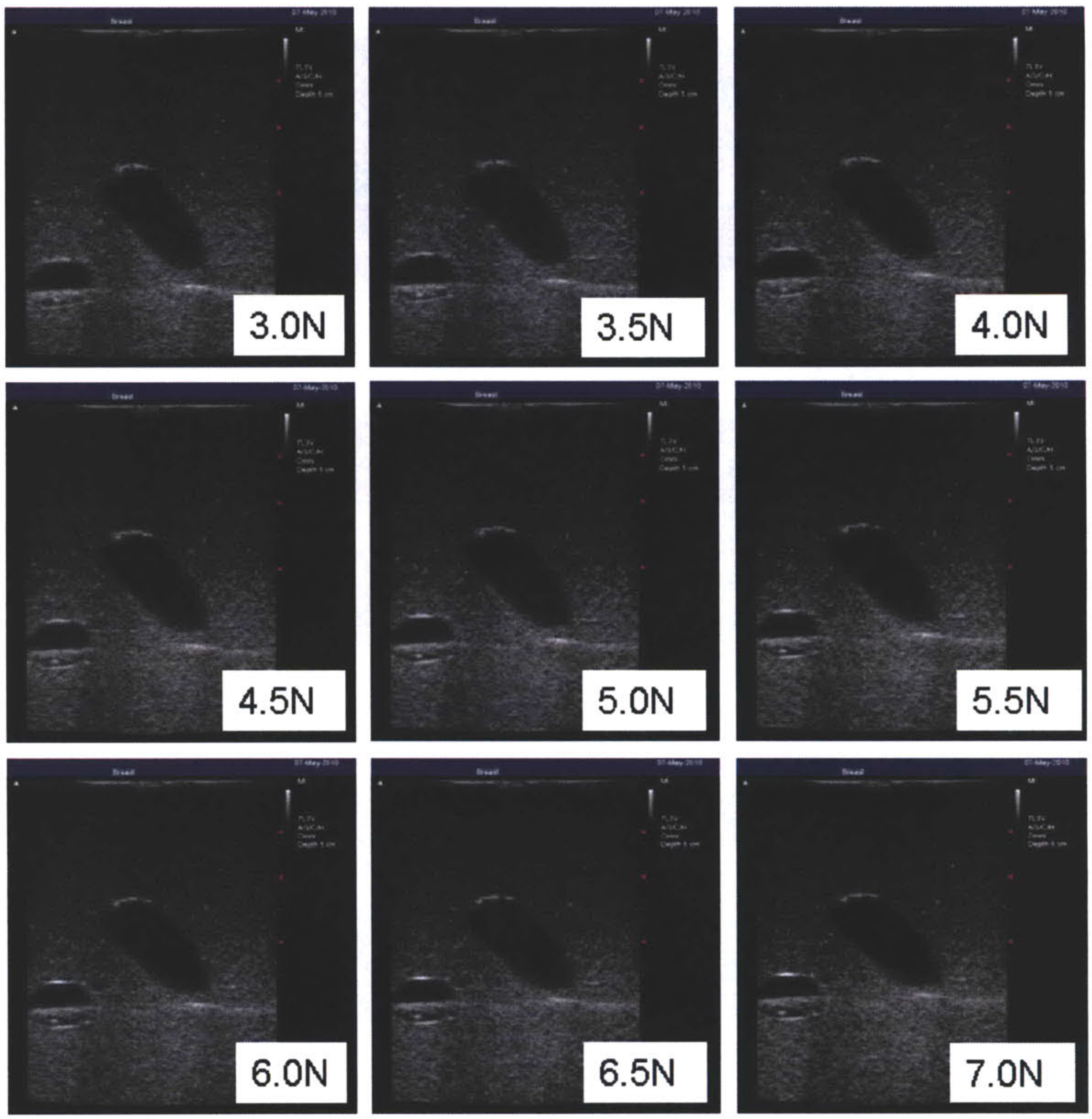

Figure 8-7: Nine images gathered of the breast phantom for contact forces between 3N to 7N

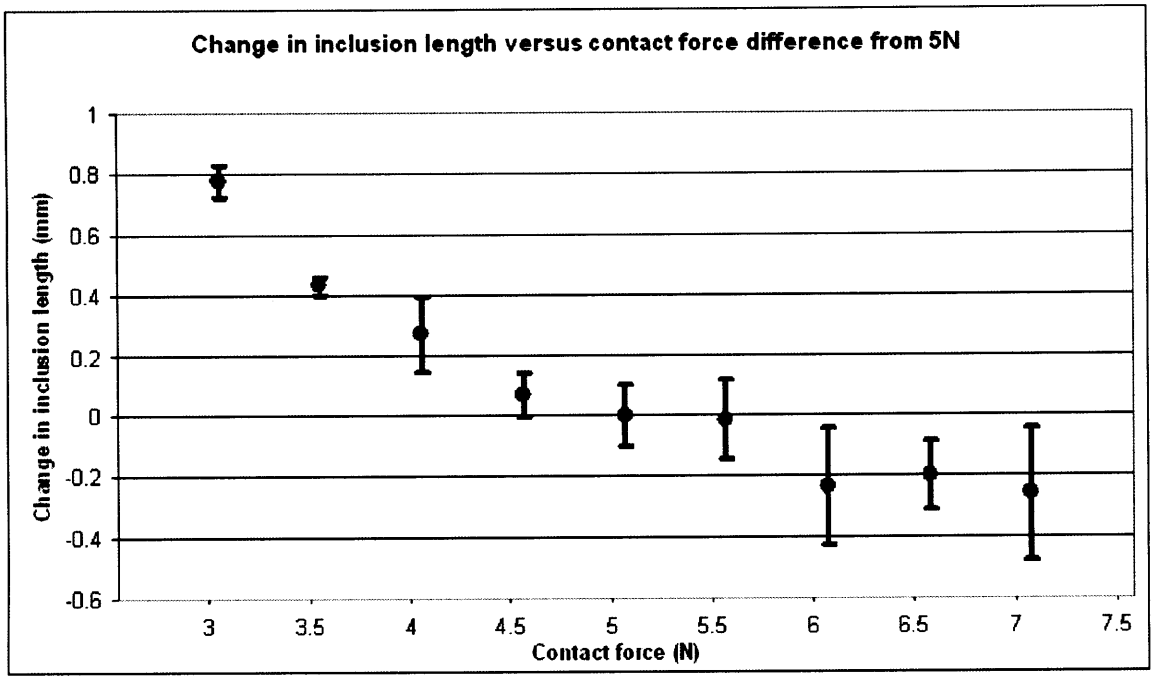

Figure 8-8: Variation in measured inclusion length from 5N image versus contact force

in length by up to 1.1mm, which is about 5% of the total length of 15mm. By maintaining constant contact force the device presented in this thesis could eliminate these contact force-dependent image variations and produce more consistent images.

8.8 Summary

This chapter described the results of several experiements that evaluated the performance of the device. We first investigated the transient time-domain response of the system to a step input. Next we used the system to determine the stiffness of a tissue phantom. We found that the device was better able to maintain a constant force than an unassisted human operator. We also found that an inclusion will change in length by up to 1.1mm (5% of total length) during a conventional (without this device) ultrasound exam due to variations in the force applied by the user. The results are discussed in more detail in Chapter 9.

Chapter 9

Conclusions

We have developed a handheld force-controlled ultrasound probe that can be used to apply a programmable contact force when gathering ultrasound images. The device has one linear degree of freedom that actuates in order to compensate for tremors or other movement in the ultrasound technician's hand. The device can be used to either apply a constant force or gather images at a range of different forces.

9.1 Summary

Initially the goal was to create a multi-DOF automated ultrasound scanning robot. A two-DOF remote center of rotation prototype was built to provide for scanning of spherically-shaped biologic objects. Next a two-DOF linear+rotational prototype was built for potential integration into the first prototype. The focus then shifted to developing a compact, single-DOF device that could fit comfortably in a person's hand and control contact force. A system was built to maintain a constant contact force and is actuated by a ballscrew.

The force-controlled probe was able to achieve the desired contact force better than an unaided human during a mock ultrasound exam. Across twelve human subjects the automated controller maintained an average 1.7 times tighter standard deviation in contact force when compared to a human maintaining a constant force by looking at a force gauge. With only muscle memory serving as force feedback, the contact force exerted by the human subjects drifted over time.

When holding the probe stationary however, the human subjects outperformed the controller. We believe that this is due to a combination of high-amplitude noise in the force sensor reading along with non-optimized controller gains.

In response to step changes in the desired contact force, the control system achieved near-zero steady-state error and zero overshoot. The system was also used to characterize the visco-elastic properties of a tissue phantom and soft tissue.

The device enables the user to apply a consistent force between images. In one experiment, a user gathered two images, one hour apart. The user applied a 20% smaller contact force in gathering the second image while the device applied the same contact force to within <2%. The same results held in two subsequent experiements with different users.

We also used the device to measure the average level of tissue distortion that would be encountered during a conventional ultrasound exam conducted without using this device. We found that an inclusion changed in length by ± 0.5mm with a force difference of ± 2N about a nominal force of 5N.

9.2 Future work

One of the important next steps is to gather feedback from real ultrasound technicians. We would like to observe how the technicians use the device and listen to their comments.

Numerous improvements to the device could enhance its speed and usability. The next step will be to look for ways to speed up the control algorithm. It is believed that if the control loop speed is improved to 1000Hz instead of the current 250Hz the force error will be even lower. One way to speed up the control loop would be to use a single-axis force sensor, which outputs an analog voltage proportional to the contact force. This would eliminate the need for the slow LabVIEW computation that currently deals with six force voltages.

By making the device smaller and lighter it would be easier for technicians to hold and manipulate. Building custom housings for the ultrasound probe electronics and more tightly integrating the force sensor could make the device smaller. A compact cable-driven system could potentially allow the motor to be mounted in a different orientation and would also make the device smaller.

Even with 10cm of travel the human subjects often unconsciously allowed the actuator to drift to one of the limits, forcing it to stop. However, the cumbersomeness of the current prototype means that the length must be reduced in order to increase its usability. The next challenge is to determine how much the length of the device can be reduced without increasing the likelihood that the user will run the device into a limit. One potential way to do this would be to provide a discreet form of feedback for the user next to the ultrasound image itself, so that the user can focus on the ultrasound image while being aware if the device is reaching a limit of travel.

Improvements in the system model will enable more optimized control which would enhance the performance of the device. In particular, future work is needed to understand the behavior of the National Instruments motion controller.

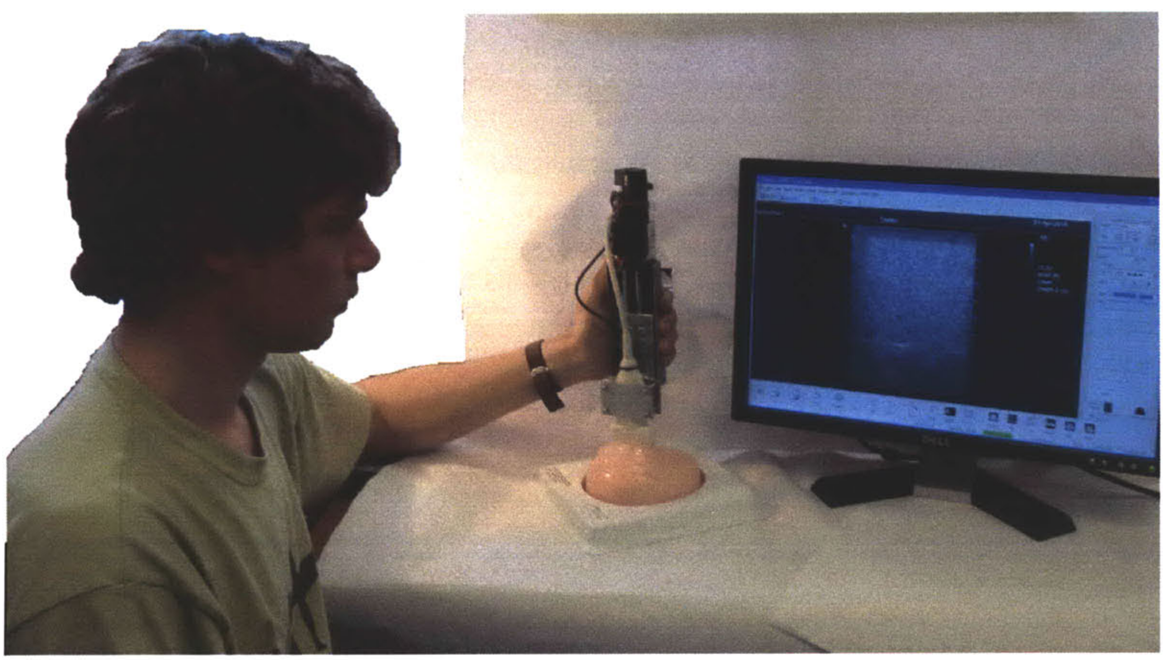

Figure 9-1: The author using the device

Bibliography

[1] http://www.pwr-con.com/pics/, April 2010.

[2] http://www.fi.edu/, April 2010.

[3] http://school.mech.uwa.edu.au, April 2010.

[4] http://www.motionnode.com/, April 2010.

[5] BEI Kimco VCA spec sheet. http://www.beikimco.com/pdf/LA19-40-000A.pdf, April 2010.

[6] NSK Monocarrier website. http://www.nskamericas.com/, April 2010.

[7] Rotolok rotary stage spec sheet. http://www.sagebrushtech.com/, April 2010.

[8] Wikipedia Least Squares article. http://en.wikipedia.org, April 2010.

[9] B.D. Adelstein. *Three degree of freedom parallel mechanical linkage*. In *US Patent Number 5816105*, Oct 1998.

[10] J. Bevirt. *Hemispherical, high bandwidth mechanical interface for computer systems*. In *US Patent Number 6024576*, Feb 2000.

[11] G. Boyer, H. Zahouani, A. Le Bot, and L. Laquieze. In vivo characterization of viscoelastic properties of human skin using dynamic micro-indentation. *Proceedings of the Annual International Conference of the IEEE Engineering in Medicine and Biology*, pages 4584 – 4587, 2007.

[12] Michael R. Burcher, J. Alison Noble, Lianghao Han, and Mark Gooding. A system for simultaneously measuring contact force, ultrasound, and position information for use in force-based correction of freehand scanning. *IEEE Transactions on Ultrasonics, Ferroelectrics, and Frequency Control*, 52(8):1330 – 1342, 2005.

[13] F. Courreges, P. Vieyres, and R.S.H. Istepanian. Advances in robotic tele-echography services - the otelo system. *Annual International Conference of the IEEE Engineering in Medicine and Biology - Proceedings*, 26:5371 – 5374, 2004.

[14] E. Degoulange, L. Urbain, P. Caron, S. Boudet, J. Gariepy, J.-L. Megnien, F. Pierrot, and E. Dombre. Hippocrate: an intrinsically safe robot for medical applications. *Proceedings. 1998 IEEE/RSJ International Conference on Intelligent Robots and Systems. Innovations in Theory, Practice and Applications (Cat. No.98CH36190)*, 2:959 - 64, 1998//.

[15] R. Gupta et al. *Guidance and Insertion System.* In *US Patent Application 2006/0229641*, Jan 2006.

[16] M.W. Gilbertson, B.A. Anthony, and S.Y. Sun. Handheld Force-Controller Ultrasound Probe. (To be published). In *Design of Medical Devices Conference, Minneapolis, MN, USA*, April 2010.

[17] L. Han, J.A. Noble, and M. Burcher. A novel ultrasound indentation system for measuring biomechanical properties in vivo soft tissue. *Ultrasound in Medicine and Biology*, 29(6):813 - 23, 2003/06/.

[18] N. Hogan. Impedance control: an approach to manipulation. parts i-iii. *Transactions of the ASME. Journal of Dynamic Systems, Measurement and Control*, 107(1):1 - 24, 1985/03/.

[19] I.W. Hunter, T.D. Doukoglou, S.R. Lafontaine, P.G. Charette, M.A. Sagar, G.D. Mallinson, and P.J. Hunter. A teleoperated microsurgical robot and associated virtual environment for eye surgery. *Presence*, 2(4):265–280, 1994.

[20] B.E. Ilon. *Wheels for a course stable selfpropelling vehicle movable in any desired direction on the ground or some other base.* In *US Patent Number 3876255*, Apr 1975.

[21] B. Landa. *Photocopier scanning apparatus.* In *US Patent Number 4355883*, Oct 1982.

[22] Akhil Madhani. *Design of Teleoperated Surgical Instruments for Minimally Invasive Surgery.* PhD thesis, Massachusetts Institute of Technology, 1998.

[23] M. Marchal and J. Troccaz. A one-DOF freehand haptic device for robotic tele-echography. *Studies in Health Technology and Informatics*, 98:231–233, 2004.

[24] K.M. Martin. *Force feedback transmission mechanisms.* In *US Patent Number 6104382*, Aug 2000.

[25] F. Najafi. *Hand controller and wrist device.* In *US Patent Number 7204168*, Apr 2007.

[26] Farshid Najafi and Nariman Sepehri. A novel hand-controller for remote ultrasound imaging. *Mechatronics*, 18(10):578 - 590, 2008.

[27] L.B. Rosenberg. *Method and apparatus for providing damping force feedback.* In *US Patent Number 5721566*, Feb 1998.

[28] S.E. Salcudean, G. Bell, S. Bachmann, W.H. Zhu, P. Abolmaesumi, and P.D. Lawrence. Robot-assisted diagnostic ultrasound - design and feasibility experiments. *Medical Image Computing and Computer-Assisted Intervention - MICCAI'99. Second International Conference. Proceedings (Lecture Notes in Computer Science Vol.1679)*, pages 1062 – 71, 1999.

[29] A. Samani and D. Plewes. A method to measure the hyperelastic parameters of ex vivo breast tissue samples. *Physics in Medicine and Biology*, 49(18):4395 – 405, 21 Sept. 2004.

[30] D. Stewart. *A Platform with Six Degrees of Freedom.* In *UK Institution of Mechanical Engineers Proceedings 1965-66*, volume 180.

[31] S.Y. Sun, B.A. Anthony, and M.W. Gilbertson. Trajectory-based deformation correction in ultrasound images. In *SPIE Conference on Medical Imaging 2010: Ultrasonic Imaging, Tomography, and Therapy, San Diego, CA, USA*, volume 7629, March 2010.

[32] A. Vilchis, J. Troccaz, P. Cinquin, K. Masuda, and F. Pellissier. A new robot architecture for tele-echography. *IEEE Transactions on Robotics and Automation*, 19(5):922 – 6, 2003/10/.

[33] A. Vilchis-Gonzalez, J.C. Avila-Vilchis, and A. Garcia-Torres. Termi robot. *Electronics, Robotics and Automotive Mechanics Conference, CERMA 2007 - Proceedings*, pages 464 – 469, 2007.

[34] P.C. Watson. *Remote center compliance system.* In *US Patent Number 4098001*, Jul 1978.